

# **DEVELOPMENT OF POLY(VINYLDENE FLUORIDE) BASED NANOTEXTILES FOR PIEZOELECTRIC AND TRIBOELECTRIC ENERGY HARVESTING**

Thesis

Submitted in partial fulfillment of the requirements for the degree of  
DOCTOR OF PHILOSOPHY

By

**GOVIND SHREENIVAS EKBOTE**



DEPARTMENT OF METALLURGICAL AND MATERIALS  
ENGINEERING  
NATIONAL INSTITUTE OF TECHNOLOGY KARNATAKA  
SURATHKAL, MANGALURU -575025  
NOVEMBER, 2023

## DECLARATION

*By the Ph.D. Research Scholar*

I hereby *declare* that the Research Thesis titled " **Development of Poly(vinylidene fluoride) based Nanotextiles for Piezoelectric and Triboelectric Energy Harvesting,**" which is being submitted to the **National Institute of Technology Karnataka, Surathkal** in partial fulfillment of the requirements for the award of the Degree of **Doctor of Philosophy in Metallurgical and Materials Engineering** is a *bonafide report of the research work carried out by me*. The material contained in this Research Thesis has not been submitted to any University or Institution for the award of any degree.



**GOVIND SHREENIVAS EKBOTE**

Register Number: 177138MT004

Department of Metallurgical and Materials Engineering  
National Institute of Technology Karnataka, Surathkal

Place: NITK-Surathkal

Date: 20/11/2023

## CERTIFICATE

This is to *certify* that the Research Thesis titled "**Development of Poly(vinylidene fluoride) based Nanotextiles for Piezoelectric and Triboelectric Energy Harvesting,**" submitted by **Govind Shreenivas Ekbote** (Register No: 177138MT004) as the record of the research work carried out by him, is *accepted as the Research Thesis submission* in partial fulfillment of the requirements for the award of degree of **Doctor of Philosophy**.

**Prof. S. Anandhan PhD FRSC**  
Department of Metallurgical & Materials Engineering  
National Institute of Technology Karnataka  
Surathkal, Srinivasnagar (P.O.)  
Mangaluru-575025, Karnataka, India.



**Prof. S. Anandhan**

Research guide

(Signature with date and seal)



**Chairman-DRPC**

(Signature with date and seal)

**Chairman - DRPC**  
Dept. of Metallurgical and Materials Engineering  
National Institute of Technology Karnataka, Surathkal  
Post Srinivasnagar, Mangaluru - 575 025  
Karnataka, India

*Dedicated to my loving parents (Aai ani Dada) and my beloved brother and sister.*



## ACKNOWLEDGMENT

---

I express my profound and most sincere gratitude to my guru, Prof. S. Anandhan, Department of Metallurgical and Materials Engineering, for his tireless guidance, invaluable mentorship, and immense support throughout my research journey. The gratitude I feel towards him is beyond words. I have been fortunate to have him as my mentor, teacher, and supervisor. The uplifting motivation and guidance he provided throughout the research process made this work possible. I have always been motivated by him to broaden my research interests. It is my pleasure to thank him for his kind words, and I will remain grateful to him forever. I would also like to extend my gratitude to his family members for their compassion and support.

I would like to convey my heartfelt gratitude to my research progress assessment committee members, Dr. Srikanth Bontha, Department of Mechanical Engineering, and Dr. Sumanth Govindarajan, Department of Metallurgical and Materials Engineering. Their constant encouragement, insightful comments, and suggestions have greatly improved my research quality and direction.

I express my heartfelt gratitude to Dr. Arunjunairaj Mahendran, Kompetenzzentrum Holz GmbH, Austria, Prof. B Venkatesa Perumal, Department of Electrical and Electronics Engineering, NITK, Prof. Udaya Bhat K., Dr. M. R. Rahman, Department of Metallurgical and Materials Engineering, NITK, who provided vital assistance and support with various characterization. I thank Dr. Ravishankar K.S., Head of the Department, Department of Metallurgical and Materials Engineering, NITK, for valuable help during my research. I am grateful to Dr. M. Selvakumar and Prof. K. N. Prabu for their valuable support throughout my research. I thank and acknowledge the Central Research Facility, NITK, for providing different characterization facilities. Also, I am deeply grateful for the direct and indirect support from the Department of Metallurgical and Materials Engineering faculty.

I am also thankful to Mrs. U. Rashmi, Mr. Sanat, Mr. Vinayraj, Mr. Bibekananda, Mr. Pradeep, Mrs. Pratheeksha, Mrs. Aniz, and Mr. Sharat for their helpful assistance with various characterization techniques. I am deeply grateful to Mrs. Sharmila Dinesh for her invaluable assistance and constant encouragement during my

research journey. I would like to thank the technicians and non-teaching staff Mrs. Vinaya D. Shettigar, Mr. Sundara Shettigar, Mr. Yashvanth K. S, Mr. Satish P., Mr. Lokesh, Mr. Sachin, and Mr. Dinesha S., of the Department of Metallurgical and Materials Engineering, NITK Surathkal, for their assistance throughout my experiments.

It is a privilege and a great pleasure to thank Dr. Mohammed Khalifa for his constant support and encouragement during the research. I would like to extend my heartfelt gratitude to Dr. Sachin Kumar B., Dr. Shamitha C., Dr. Sawan Shetty, Dr. Sathies T., Mr. Harsha G. Patil, Mr. Abhipreet Mohapatra for their technical support, cooperation, and motivation during my research work.

It gives me great pleasure to express my gratitude to my friends for their love and support, Mr. Anvit Khare, Mr. Basavaraj Padasale, Mr. Agustin Samuele, Mr. Kamalanathan D, Dr. Pavan Sondar, Dr. Robbi Vivek Vardhan, Mr. Pravin Lakkimsetti, Dr. Komalakrishna Hadagalli, Mr. Bikesh Kumar, Dr. Prabhu C., Dr. Sunil Meti, Mr. Rajesh Samleti, Mr. Nagesh Gorre, are only a few among them.

I sincerely express my gratitude towards all my teachers who taught and helped me become who I am today. I am grateful for their guidance and support.

I wholeheartedly express my deepest gratitude to my family with profound appreciation. No words can adequately convey my immense gratitude to my father, Shreenivas, and mother, Shantabai, for their prayers and the countless sacrifices they selflessly made for me. I express my deepest gratitude to my brother, Chandrakant, and sister, Babita, for their constant encouragement and support during hard times. Also, I would like to thank my brother-in-law, Balaji, and nieces (Mansi, Prasanna, and Harshali) for their wholehearted support. Lastly, I extend my gratitude to all my friends and colleagues for their valuable assistance, feedback, and indirect support throughout the completion of my research work.

**GOVIND SHREENIVAS EKBOTE**

## ABSTRACT

---

Piezoelectric and triboelectric nanogenerators have experienced a steep increment in popularity over the last few years as an alternative power source for miniature devices and the internet of things (IoT). Herein, piezoelectric nanogenerators (PENG) and triboelectric nanogenerators (TENG) based on electrospun poly(vinylidene fluoride) (PVDF) composites and cationic surfactant doped nanofabric were developed. Two nanoscale fillers, namely reverse microemulsion synthesized barium tungstate nanorods (BWN) and mica nanosheets (MNS), and cationic surfactant (tetra-n-butyl ammonium chloride) (TBAC) were employed to enhance the electroactive phase content of PVDF. The nanofabrics were probed for their morphology, crystallinity, polymorphism, dielectric properties, piezo capacitance, and piezoelectric and triboelectric performances. Incorporation of either the nanoscale filler or the cationic surfactant enhanced the electroactive phase content of PVDF, which was supported by the FTIR spectral and XRD results. The maximum  $\beta$ -phase content of 89% was obtained at a TBAC loading of 3 wt%. The dielectric constant of TBAC doped nanofabrics was enhanced and a maximum of 22.5 was observed for the nanofabric containing 3 wt% of TBAC. The PENG based on the same nanofabric generated a  $V_{OC}$  of 17.2 V (under 5 N force) and an instantaneous power density of  $\sim 1.4 \mu\text{W}/\text{cm}^2$  (under 3 N force). The addition of BWN into the PVDF matrix enhanced its electroactive phase content (in the form of  $\beta$  and  $\gamma$ -phases), reaching a maximum of 86.5% at 3 wt% loading. Addition of BWN into PVDF led to a significant enhancement in the dielectric constant of composite nanofabrics. The highest dielectric constant of 17.68 was recorded for PVDF nanofabric containing 5 wt% of BWN. The enhanced piezo capacitive sensing ability was observed in the aforementioned composite nanofabric with a sensitivity value of 0.66/N. A piezoelectric  $V_{OC}$  of 8 V and an instantaneous power density of  $4.3 \mu\text{W}\cdot\text{cm}^{-2}$ , while the triboelectric  $V_{OC}$  of 200 V and an instantaneous power density of  $646 \mu\text{W}\cdot\text{cm}^{-2}$  were generated by nanogenerators based on PVDF nanofabric containing 3 wt% of BWN. The fluttering-driven triboelectric nanogenerator based on the same composite nanofabric generated 84 V when exposed

to a wind speed of 7 m/s. The MNS-infused electrospun PVDF composite nanofabrics demonstrated enhancement in electroactive and dielectric properties. The optimal loading of MNS was determined to be 0.75 wt%, resulting in the highest  $\beta$ -phase content of 84.3%. The PVDF nanofabric containing 0.75 wt% exhibited the highest dielectric constant of 14.7, which was  $\sim 1.64$  than that of PVDF nanofabric. The previously mentioned composite nanofabric showed the enhanced piezo capacitive response with a sensitivity value of 0.6/N. The piezoelectric nanogenerator consisting of PVDF composite nanofabric containing 0.75 wt% generated a  $V_{OC}$  of 8.4 V and an instantaneous power density of  $3 \mu\text{W}\cdot\text{cm}^{-2}$ . Additionally, The TENG fabricated the aforementioned composite nanofabric generated  $V_{OC}$  of 163 V and instantaneous power density of  $585 \mu\text{W}\cdot\text{cm}^{-2}$  under single finger tapping. A fluttering-based device consisting of PVDF composite nanofabric containing 0.75 wt% of MNS generated an output of 70 V at a wind speed of 7 m/s. The improved dielectric properties, as well as the enhanced piezoelectric and triboelectric performance of the electrospun PVDF composites and doped nanofabrics developed in this study, can provide an edge to researchers working on energy harvesters. A TENG based on a PVDF nanofabric containing 0.75 wt% of MNS successfully lit 35 LEDs. Furthermore, another TENG consists of PVDF nanofabric containing 3 wt% of BWN illuminated 40 LEDs connected to it in series.

**Keywords:** Electrospinning; poly(vinylidene fluoride); nanocomposite; piezoelectric; triboelectric; energy harvesting.

## CONTENTS

---

|   |            |
|---|------------|
| <b>CONTENTS</b>   |            |
| <b>LIST OF FIGURES</b>  | <b>i</b>   |
| <b>LIST OF TABLES</b>   | <b>vii</b> |
| <b>NOMENCLATURE</b>   | <b>ix</b>  |
| <b>CHAPTER 1: INTRODUCTION AND LITERATURE REVIEW</b>                                  | <b>1</b>   |
| 1.1 INTRODUCTION  | 1          |
| 1.1.1 Piezoelectricity  | 2          |
| 1.1.2 Triboelectricity  | 5          |
| 1.1.2.1 Mechanisms of triboelectrification  | 7          |
| 1.1.2.2 Operational modes of TENG   | 10         |
| 1.1.2.3 Mathematical expression of contact-separation mode based TENG                 | 12         |
| 1.1.3 Capacitive Sensing  | 13         |
| 1.1.4 PVDF  | 14         |
| 1.1.5 Electrospinning Process   | 17         |
| 1.2 LITERATURE REVIEW   | 20         |
| 1.2.1 Electrospun PVDF doped/composite nanofabrics based piezoelectric nanogenerators | 20         |
| 1.2.2 Triboelectric Nanogenerators  | 24         |
| 1.2.2.1 Material composition modification   | 24         |
| 1.2.2.2 Chemical modification of contact surface                                      | 26         |
| 1.2.2.3 Physical modification of surface  | 26         |
| 1.2.2.4 Triboelectric nanogenerators based on composites of PVDF                      | 28         |
| 1.2.3 Capacitive Sensors  | 30         |
| 1.3 PROBLEM IDENTIFICATION  | 36         |

|   |           |
|---|-----------|
| 1.4 SCOPE AND OBJECTIVES OF THE PRESENT WORK  | 36        |
| 1.4.1 Scope   | 36        |
| 1.4.2 Objectives  | 37        |
| <b>CHAPTER 2: MATERIALS AND METHODS</b>   | <b>41</b> |
| 2.1 MATERIALS   | 41        |
| 2.2 METHODS   | 41        |
| 2.2.1 Electrospinning of TBAC-doped PVDF nanofabrics  | 41        |
| 2.2.2 Synthesis of barium tungstate nanorods (BWN)  | 42        |
| 2.2.3 Electrospinning of PVDF/BWN Composite Nanofabrics   | 42        |
| 2.2.4 Electrospinning of PVDF/mica nanosheets (MNS) Composite Nanofabrics   | 43        |
| 2.3 MEASUREMENT AND CHARACTERIZATION  | 45        |
| 2.4 SETUPS AND METHODOLOGY EMPLOYED FOR THE PIEZOELECTRIC, PIEZO CAPACITANCE AND TRIBOELECTRIC PERFORMANCE EVALUATION OF ELECTROSPUN PVDF COMPOSITE/DOPED NANOFABRICS | 48        |
| 2.4.1 Piezoelectric and piezo capacitance setup   | 48        |
| 2.4.2 Triboelectric setup   | 49        |
| <b>CHAPTER 3: CATIONIC SURFACTANT ASSISTED ENHANCEMENT OF DIELECTRIC AND PIEZOELECTRIC PROPERTIES OF PVDF NANOFIBERS FOR ENERGY HARVESTING APPLICATION</b>            | <b>53</b> |
| 3.1 RESULTS AND DISCUSSION  | 53        |
| 3.1.1 Morphology  | 53        |
| 3.1.2 FTIR spectral analysis  | 54        |
| 3.1.3 Phase and crystallinity analysis using WAXD and DSC results   | 56        |
| 3.1.4 Piezoelectric Performance   | 58        |
| 3.1.5 Dielectric studies  | 61        |

**CHAPTER 4: DEVELOPMENT OF A FLEXIBLE PIEZOELECTRIC AND TRIBOELECTRIC ENERGY HARVESTER WITH PIEZO CAPACITIVE SENSING ABILITY FROM BARIUM TUNGSTATE NANOROD-DISPERSED PVDF NANOFABRICS 65**

|  |    |
|--|----|
| 4.1 RESULTS AND DISCUSSION                               | 65 |
| 4.1.1 Characterization of BWN                            | 65 |
| 4.1.2 Characterization of PVDF/BWN composite nanofabrics | 66 |
| 4.1.2.1 Morphology                                       | 66 |
| 4.1.2.2 FTIR spectral analysis                           | 68 |
| 4.1.2.3 WAXD analysis                                    | 71 |
| 4.1.2.4 Dielectric studies                               | 72 |
| 4.1.2.5 Piezo capacitance evaluation                     | 74 |
| 4.1.2.6 Piezoelectric properties                         | 76 |
| 4.1.2.7 Triboelectric properties                         | 77 |

**CHAPTER 5: A NEW MULTIFUNCTIONAL ENERGY HARVESTER BASED ON MICA NANOSHEETS-DISPERSED PVDF NANOFABRICS FEATURING PIEZO-CAPACITIVE, PIEZOELECTRIC AND TRIBOELECTRIC EFFECTS 85**

|   |    |
|---|----|
| 5.1 RESULTS AND DISCUSSION                    | 85 |
| 5.1.1 SEM and TEM analysis of the nanofabrics | 85 |
| 5.1.2 FTIR spectral analysis                  | 87 |
| 5.1.3 WAXD analysis                           | 89 |
| 5.1.4 Dielectric studies                      | 91 |
| 5.1.5 Piezo capacitance evaluation            | 92 |
| 5.1.6 Piezoelectric performance               | 94 |
| 5.1.7 Triboelectric performance               | 96 |

**CHAPTER 6: SUMMARY AND CONCLUSIONS 103**

|                               |            |
|-------------------------------|------------|
| <b>SCOPE FOR FURTHER WORK</b> | <b>107</b> |
| <b>APPENDIX -I</b>            | <b>109</b> |
| <b>REFERENCES</b>             | <b>115</b> |
| <b>BIO-DATA</b>               | <b>139</b> |
| <b>LIST OF PUBLICATIONS</b>   | <b>141</b> |

## LIST OF FIGURES

---

| Figure No. | Caption   | Page No. |
|------------|---|----------|
| 1.1        | Schematic of the direct piezoelectric and converse piezoelectric effects, (a) Poled piezoelectric material, (b) Upon the application of tensile stress, a voltage is produced, and (c) Upon the application of compressive stress, a voltage is produced with reversed polarity, (d) Upon the application of DC voltage, a tensile strain is induced, (e) Upon the application of DC voltage with reversed polarity, a compressive strain is induced.   | 2        |
| 1.2        | Arrangement of dipoles (a) Prior to polarization, (b) at the time of polarization, (c) after polarization.  | 4        |
| 1.3        | Schematic of piezoelectric $d_{31}$ and $d_{33}$ configurations of piezoelectric materials.   | 5        |
| 1.4        | The charge transfer between metal-dielectric (semiconductor) is explained using a modified solid-state model, (a) prior to contact, there is no exchange of charges, (b) during contact, electrons present at a high energy level in metal transferred to the dielectrics/insulators, (c) after contact, some electrons return to the metal, and few remains on the surface of dielectric/insulators due to energy barrier, (d) Some charges are released due to thermionic effect. $\Phi$ - metal work function; $E_F$ -Fermi level; $E_{VAC}$ -vacuum level; $E_C$ -conduction band; $E_V$ -valence band; $E_n$ -neutral level of surface states. | 7        |
| 1.5        | Schematic of the electron cloud and potential well describing the charge transfer between two materials, (a) prior to contact, (b) at the time of contact, (c) after contact, (d) few charges are released due to thermionic effect.  | 8        |

## LIST OF FIGURES

|      |   |    |
|------|---|----|
| 1.6  | Schematic (a) water bridge model describing ion transfer in the ionic polymer, (b) water bridge model describing asymmetrically redistributed OH <sup>-</sup> and H <sup>+</sup> causing ion transfer in non-ionic polymers.                                    | 9  |
| 1.7  | Schematic of the theoretical mass transfer model involving charge transfer between two materials.   | 10 |
| 1.8  | Schematic of the different modes of triboelectric nanogenerators: (a) Vertical contact-separation mode, (b) in-plane contact-sliding mode, (c) single electrode mode, (d) freestanding triboelectric-layer mode.  | 12 |
| 1.9  | Schematic of three major phases of PVDF.  | 15 |
| 1.10 | Schematic of electrospinning setup and its components.  | 18 |
| 1.11 | Applications of electrospun nanofibers in various fields.   | 20 |
| 1.12 | The state of the art of textile-based TENGs based literature retrieved in the year 2012 to 2020; The articles on textile-based TENG were obtained according to (a) different years, (b) various nations, and (c) independent research institutes, respectively. | 28 |
| 2.1  | Setup used for the evaluation of (a) Piezo-capacitance based pressure sensor, (b) PENG.   | 49 |
| 2.2  | Schematic illustration of the PENG and the piezoelectric and piezo capacitive response measurement setup.   | 49 |
| 2.3  | (a) Schematic illustration, and (b) digital photograph of TENG.   | 50 |
| 2.4  | Schematic illustration of the FDTENG.   | 50 |
| 3.1  | SEM images of (a) EPVDF; and PVDF/TBAC doped nanofibers: (b) PVDF/TBAC-1.0, (c) PVDF/TBAC-2.0, (d) PVDF/TBAC-3.0, (e) PVDF/TBAC-5.0.  | 54 |
| 3.2  | FTIR spectra (a) EPVDF and PVDF/TBAC doped nanofabrics, (b) Shift in the C-F band of PVDF upon the addition of TBAC.  | 55 |
| 3.3  | Plausible mechanism of interaction between PVDF, DMF and TBAC.  | 56 |
| 3.4  | WAXD patterns of EPVDF and PVDF/TBAC doped nanofabrics.   | 57 |
| 3.5  | DSC curves (second heating cycle) of EPVDF and PVDF/TBAC doped nanofabrics.   | 58 |

## LIST OF FIGURES

|     |  |    |
|-----|--|----|
| 3.6 | (a) Piezoelectric response of EPVDF and PVDF/TBAC doped nanofabrics at different loading of TBAC (under a constant applied force of 2.5 N), (b) Piezoelectric response of PVDF/TBAC-3.0 under different values of applied force. | 60 |
| 3.7 | (a) The output voltage and current across different load resistances, (b) calculated power density of PVDF/TBAC-3.0 based PENG under 3 N load at different load resistance values.   | 61 |
| 3.8 | Frequency-dependent; (a) dielectric constant, (b) dielectric loss of EPVDF and PVDF/TBAC doped nanofabrics.  | 62 |
| 4.1 | (a) WAXD, (b) FTIR spectrum, (c) $\zeta$ -potential curve, and (d) FESEM image of BWN.   | 66 |
| 4.2 | FESEM images of (a) EPVDF, (b) PVDF/BWN-0.5, (c) PVDF/BWN-1, (d) PVDF/BWN-1.5, (e) PVDF/BWN-2, (f) PVDF/BWN-3, (g) PVDF/BWN-5 (the AFD and SD values are indicated as inset within each image).                                  | 67 |
| 4.3 | TEM images of a single nanofiber of PVDF/BWN-3 imaged at two locations.  | 67 |
| 4.4 | FTIR spectra of EPVDF and PVDF/BWN composite nanofabrics in the wavenumber ranges of (a) 1800-650 $\text{cm}^{-1}$ , (b) 1350-1200 $\text{cm}^{-1}$ , (c) 3100-2880 $\text{cm}^{-1}$ .   | 69 |
| 4.5 | Schematic representation of plausible mechanism of interaction between the surface of BWN and PVDF chains.   | 70 |
| 4.6 | WAXD patterns of EPVDF and PVDF/BWN composite nanofabrics.   | 71 |
| 4.7 | Deconvoluted WAXD patterns of (a) EPVDF and (b) PVDF/BWN-3.  | 72 |
| 4.8 | Frequency-dependent (a) dielectric constant and (b) dielectric loss of EPVDF and PVDF/BWN composite nanofabrics, (c) dielectric constant and dielectric loss values at 1000 Hz as a function of the loading of BWN.              | 74 |

## LIST OF FIGURES

- 4.9 (a) Ratio of relative change in capacitance to the initial capacitance ( $\Delta C/C_0$ ) of the sensor fabricated from PVDF/BWN-5 and (b) ratio of relative change in capacitance to the initial capacitance ( $\Delta C/C_0$ ) of EPVDF at 8 N load, and (c) ratio of relative change in the capacitance to the initial capacitance ( $\Delta C/C_0$ ) of the sensor based on PVDF/BWN-5 with respect to the applied force. 75
- 4.10 (a) Piezoelectric response of (i) EPVDF, (ii) PVDF/BWN-0.5, (iii) PVDF/BWN-1, (iv) PVDF/BWN-1.5, (v) PVDF/BWN-2, (vi) PVDF/BWN-3, (vii) PVDF/BWN-5, (b) instantaneous power density and  $V_{OC}$  of PVDF/BWN-3 across different load resistances at 10 N applied force. 77
- 4.11 (a) Variation of the triboelectric  $V_{OC}$  of (i) EPVDF, (ii) PVDF/BWN-0.5, (iii) PVDF/BWN-1, (iv) PVDF/BWN-1.5, (v) PVDF/BWN-2, (vi) PVDF/BWN-3, (vii) PVDF/BWN-5, TENG, (b) instantaneous power density and  $V_{OC}$  of PVDF/BWN-3 based TENG across the different values of resistances, (c) schematic illustration of the working mechanism of TENG, (d)  $V_{OC}$  of TENG over  $\sim 600$  cycles, (e) photograph shows forty LEDs directly connected in series to TENG based on PVDF/BWN-3 nanofabric, which were illuminated by finger tapping force (inset shows schematic of TENG device directly connected to LED). 80
- 4.12 (a) Variation of the triboelectric  $V_{OC}$  of the FDTENG at different wind speeds, and (b) working principle of FDTENG. 82
- 5.1 SEM images of (a) EPVDF, (b) PVDF/MNS-0.25, (c) PVDF/MNS-0.5, (d) PVDF/MNS-0.75, (e) PVDF/MNS-1 nanofibers, (f) MNS. 85
- 5.2. TEM images of PVDF/MNS-0.75 nanofiber at two different locations. 86
- 5.3 FTIR spectra of EPVDF and PVDF/MNS composite nanofabrics (a) 2000-650  $\text{cm}^{-1}$ , (b) 900-860  $\text{cm}^{-1}$ , (c) 1230-1140  $\text{cm}^{-1}$ . 87
- 5.4 Visual depiction illustrating the potential mechanism of interaction between MNS and PVDF chains. 89

## LIST OF FIGURES

- 5.5 X-ray diffractograms of EPVDF and PVDF/MNS composite nanofabrics. 90
- 5.6 Deconvoluted X-ray diffractograms of (a) EPVDF and (b) PVDF/MNS-0.75. 90
- 5.7 (a) Dielectric constant and (b) dielectric loss of EPVDF and PVDF/MNS composite nanofabrics as a function of frequency, (c) variation of dielectric constant and dielectric loss with respect to MNS loading (at 1000 Hz) of the nanofabrics. 91
- 5.8 (a) The response ( $\Delta C/C_0$ ) of PVDF/MNS-0.75 based capacitive sensor (under 9 N load), (b) the response ( $\Delta C/C_0$ ) of EPVDF based capacitive sensor (under 9 N load), and (c) ratio of relative change in capacitance to the initial capacitance of the sensor as a function of the applied load. 94
- 5.9 (a) Piezoelectric response of EPVDF and PVDF/MNS composite nanofabrics based PENG with varying loading of MNS, (b) piezoelectric voltage generated, and instantaneous power density of PVDF/MNS-0.75 based PENG across the different resistances (applied force of 8 N). 95
- 5.10 (a) Triboelectric response of the TENG based on nanofabrics with different loading of MNS, (b) voltage response and instantaneous power density at different load resistances, (c) triboelectric response of PVDF/MNS-0.75 based TENG for  $\sim 1000$  cycles, (d) the photograph of thirty-five LEDs connected to TENG based on PVDF/MNS-0.75 in series, lit under one finger tapping (inset: schematic of LEDs connected to TENG in series). 96
- 5.11 (a) Triboelectric performance of PVDF/MNS-0.75 based FDTENG when exposed to varying wind speeds, (b) schematic of the working mechanism of FDTENG. 99



## LIST OF TABLES

---

| <b>Table No.</b> | <b>Caption</b>  | <b>Page No.</b> |
|------------------|---|-----------------|
| 1.1              | Triboelectric series.   | 6               |
| 1.2              | Piezoelectric performance of PVDF-based doped/composite nanofabrics.  | 32              |
| 1.3              | Triboelectric performance of PVDF-based composites.   | 35              |
| 2.1              | Notations used for the PVDF based nanofabrics.  | 44              |
| 3.1              | Melting temperature ( $T_m$ ), enthalpy of melting ( $\Delta H_s$ ), crystallinity $\chi_{c(DSC)}(\%)$ and $F(\beta)(\%)$ of EPVDF and PVDF/TBAC doped nanofabrics. | 58              |
| 4.1              | $F(EA)(\%)$ , $F(\beta)(\%)$ , $F(\gamma)(\%)$ , and total crystallinity of PVDF/BWN composite nanofabrics.   | 70              |
| 5.1.             | $F(\beta)(\%)$ and $\chi(WAXD)(\%)$ of PVDF/MNS composite nanofabrics.  | 88              |



## NOMENCLATURE

---

|                                  |                                 |
|----------------------------------|---------------------------------|
| $\overline{M}_w$                 | Weight average molecular weight |
| %                                | Percentage                      |
| °                                | Degree                          |
| °C                               | Degree Celsius                  |
| ζ                                | Zeta                            |
| θ                                | Theta                           |
| 0-D                              | Zero dimensional                |
| 1-D                              | One dimensional                 |
| 2-D                              | Two dimensional                 |
| 3-D                              | Three dimensional               |
| μW                               | Microwatt                       |
| μC                               | Microcoulomb                    |
| μA                               | Microampere                     |
| μm                               | Micrometer                      |
| AFD                              | Average fiber diameter          |
| Al                               | Aluminium                       |
| Au                               | Gold                            |
| BTO                              | Barium titanate                 |
| BiFeO <sub>3</sub>               | Bismuth ferrite                 |
| BiCl <sub>3</sub>                | Bismuth chloride                |
| C                                | Coulomb                         |
| Cu                               | Copper                          |
| cm                               | Centimeter                      |
| Cu Kα                            | Copper k-alpha                  |
| CoFe <sub>2</sub> O <sub>4</sub> | Cobalt ferrite                  |
| CNT                              | Carbon nanotube                 |
| DMF                              | N, N-dimethylformamide          |
| DMSO                             | Dimethyl sulfoxide              |
| DMAc                             | Dimethylacetamide               |

## NOMENCLATURE

|                                 |  |
|---------------------------------|--|
| DSC                             | Differential scanning calorimetry            |
| EPVDF                           | Electrospun poly(vinylidene fluoride)        |
| F                               | Farad  |
| F( $\beta$ )                    | Fraction of $\beta$ -phase                   |
| F( $\gamma$ )                   | Fraction of $\gamma$ -phase                  |
| F(EA)                           | Fraction of electroactive phases             |
| Fe <sub>3</sub> O <sub>4</sub>  | Iron oxide                                   |
| g                               | Gram   |
| G                               | Gauge  |
| Gd <sub>5</sub> Si <sub>4</sub> | Gadolinium silicide                          |
| h                               | Hour   |
| hBN                             | Hexagonal boron nitride                      |
| Hz                              | Hertz  |
| ICDD                            | International Centre for Diffraction Data    |
| IoT                             | Internet of things                           |
| I <sub>sc</sub>                 | Short circuit current                        |
| K                               | Kelvin                                       |
| kHz                             | Kilohertz                                    |
| kPa                             | Kilopascal                                   |
| kV                              | Kilovolt                                     |
| LiCl                            | Lithium chloride                             |
| LCR meter                       | Inductance, Capacitance and Resistance meter |
| LED                             | Light-emitting diode                         |
| m                               | Meter  |
| M                               | Molar  |
| mA                              | Milliampere                                  |
| min                             | Minute                                       |
| mL                              | Millilitre                                   |
| mW                              | Milliwatt                                    |
| mV                              | Millivolt                                    |
| MoS <sub>2</sub>                | Molybdenum disulfide                         |

## NOMENCLATURE

|                                      |   |
|--------------------------------------|---|
| MWCNT                                | Multi-walled carbon nanotubes           |
| MΩ                                   | Megaohm                                 |
| N                                    | Newton                                  |
| nA                                   | nanoampere                              |
| nm                                   | nanometer                               |
| NiCl <sub>2</sub> .6H <sub>2</sub> O | Nickel chloride hexahydrate             |
| Pa                                   | Pascal                                  |
| pC                                   | picocoulomb                             |
| PVDF                                 | Poly(vinylidene fluoride)               |
| rpm                                  | Revolutions per minute                  |
| s                                    | Second                                  |
| SiO <sub>2</sub>                     | Silicon dioxide                         |
| SnO <sub>2</sub>                     | Tin oxide                               |
| SWCNT                                | Single-walled carbon nanotubes          |
| tan δ                                | Dielectric loss                         |
| T <sub>m</sub>                       | Melting temperature                     |
| V                                    | Volt                                    |
| V <sub>oc</sub>                      | Open circuit voltage                    |
| W                                    | Watt                                    |
| w/v%                                 | Weight by volume percent                |
| wt%                                  | Weight percent                          |
| X <sub>c</sub>                       | Degree of crystallinity                 |
| Zn-Al-LDH                            | Zinc-Aluminium Layered Double Hydroxide |
| ZnSO <sub>3</sub>                    | Zinc sulfite                            |
| ZnO                                  | Zinc oxide                              |



# CHAPTER 1

---

The contents of this chapter will be published in *Journal of Micro and Nano Engineering* (In pipeline).



## CHAPTER 1

### INTRODUCTION AND LITERATURE REVIEW

---

*This chapter provides a brief overview of PVDF-based electrospun nanocomposites and their application potential in energy harvesting and capacitive sensing. A brief introduction to energy harvesting, piezoelectricity, triboelectricity, capacitive sensing, PVDF, and electrospinning has been presented. A summarized literature review of piezoelectric and triboelectric energy harvesters and capacitive sensing has been discussed with a focus on tailoring the electroactive phase and dielectric properties of composite nanofabrics.*

#### 1.1 INTRODUCTION

Renewable energy plays a significant role in sustainable development that benefits human health and environment. Several kinds of renewable energy sources are being used for some of the energy demands of humankind. These include solar energy, wind energy, ocean energy, geothermal energy, and hydropower energy (Lund 2007). In its broadest sense, energy could be described as being in the range of mega Watt or giga Watt, which could be used to power industries and residential localities. However, there are huge numbers of miniature devices that require low power in the range of mW to  $\mu$ W to run (Wang and Wu 2012). Recently, The number of these devices has grown exponentially due to advances in science and technology. The energy consumption of each device may be small, but collectively the power required to run these devices would be high. These devices can be powered by batteries. However, because of the large number of batteries and their potential placement in remote locations, replacing and recycling them is a challenge (Wang et al. 2016). Energy harvesting is a process that refers to converting waste ambient energy into electrical energy. The ambient energy in the form of waste mechanical vibrations, thermal, wind, motion, and light are converted into useful electrical energy by piezoelectric effect (Safaei et al. 2019), pyroelectric effect (Thakre et al. 2019), triboelectric effect (Wang et al. 2016), electromagnetic effect (Han et al. 2014; Hu et al. 2014) and photoelectric effect (Lin et al. 2016). Piezoelectric and triboelectric energy harvesters have attracted the attention

of researchers due to their simplicity and versatility, as well as their efficient conversion and easy integration (Fan et al. 2016; Kalimuldina et al. 2020; Luo and Wang 2020). Piezoelectric materials generate electricity through mechanical vibration due to electric polarization. In triboelectric nanogenerators, the contact between two dissimilar materials leads to the generation of electricity due to the triboelectric effect combined with electrostatic induction. A piezoelectric nanogenerator and a triboelectric nanogenerator can be used as potential power sources for low-power miniature devices.

### 1.1.1 Piezoelectricity

When a piezoelectric material is stressed mechanically, it produces electricity across its surface. When an electric field is applied to these materials, it induces mechanical strain in the material (Fig. 1.1). It was the Curie brothers who discovered the piezoelectric effect. In March 1880, the findings were published in the French scientific journal *Comptes Rendus*. The converse piezoelectric effect was predicted theoretically by Lippman and later confirmed by the Curie brothers (Mason 1981).

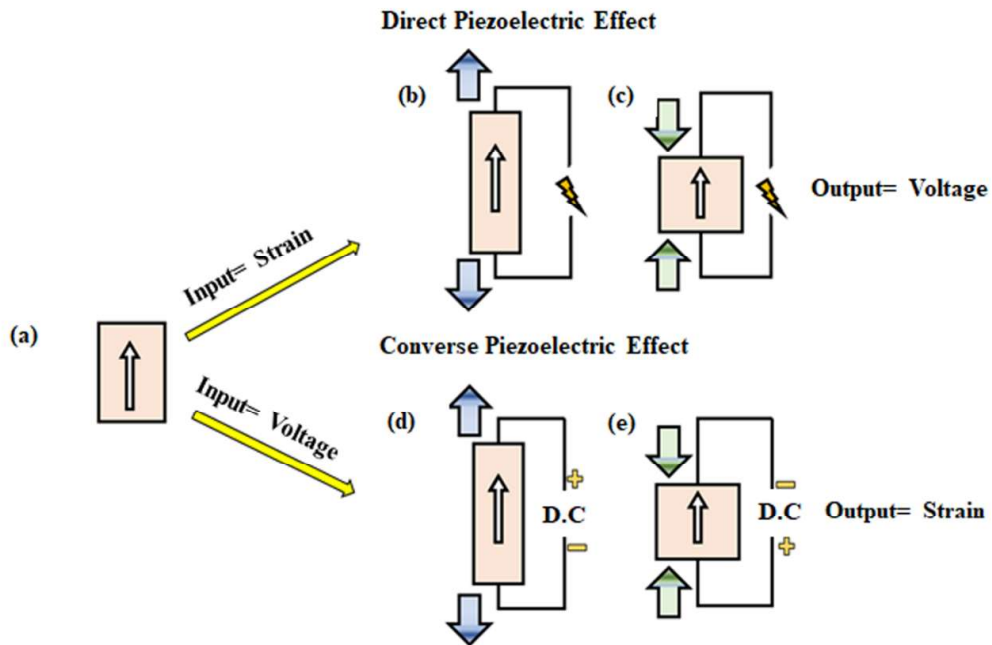


Fig. 1.1 Schematic of the direct piezoelectric and converse piezoelectric effects, (a) Poled piezoelectric material, (b) Upon the application of tensile stress, a voltage is

produced, and (c) Upon the application of compressive stress, a voltage is produced with reversed polarity, (d) Upon the application of DC voltage, a tensile strain is induced, (e) Upon the application of DC voltage with reversed polarity, a compressive strain is induced (Atif et al. 2020).

The piezoelectric effect is observed in certain crystals that lack inversion symmetry. Initially, the dipoles in the material are arranged randomly so that the resultant dipole moment becomes zero; upon application of a strong electric field just below the Curie temperature, the dipoles orient in the direction of an applied electrical field. After the complete removal of an electric field, the material possesses a net dipole moment (Fig. 1.2). The net-aligned dipoles are responsible for the piezoelectric effect in non-centrosymmetric crystals (Caliò et al. 2014; Li et al. 2014; Mishra et al. 2019). The following equations can describe the piezoelectric effect and its converse effect:

Direct piezoelectric effect

$$S_i = s_{ij}^E T_j + d_{ki} E_k \quad (1.1)$$

Converse piezoelectric effect

$$D_i = d_{ij} T_j + \varepsilon_{ik}^T E_k \quad (1.2)$$

where subscripts  $i$ ,  $j$ , and  $k$  represent the three spatial dimensions, and the strain and stress induced by the mechanical and electrical effects are described by  $S$  and  $T$ , respectively. The electrical displacement and electrical field are denoted by  $D$  and  $E$ , respectively.  $s^E$  and  $\varepsilon^T$  are elastic compliance matrices at constant electric field and permittivity value at constant stress. The piezoelectric coefficient is represented by  $d$  (electric charge(C)/applied load(N)) (Qi and Mcalpine 2010). The two primary configurations for piezoelectric materials are  $d_{31}$  and  $d_{33}$ , which are determined by the direction of polarization and applied stress. The  $d_{33}$  configuration depicts the electric polarization generated in the same direction as the applied stress, and  $d_{31}$  represents the electric polarization (3) induced in the direction normal to the applied stress direction (1) (Fig. 1.3).

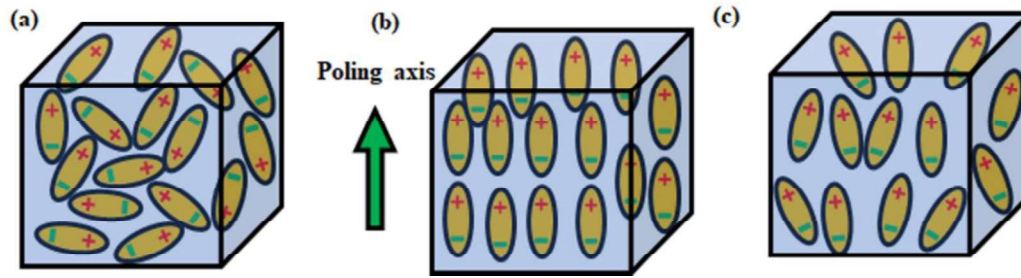


Fig. 1.2 Arrangement of dipoles (a) Prior to polarization, (b) at the time of polarization, (c) after polarization (Korkmaz and Kariper 2022).

During its early days, Rochelle salt was known for its ferroelectric nature and was used as a sensor. At present, approximately 200 materials are found to exhibit piezoelectric property. The materials such as barium titanate (BTO), lead zirconate titanate (PZT), and potassium niobate are known for their high piezoelectric coefficient values (Mishra et al. 2019). However, Jong et al.'s research group has presented a database of 941 potential inorganic piezoelectric materials, which were not known before. The intrinsic piezoelectric constant was calculated using the Density Function Perturbation Theory (DFPT). The piezoelectric coefficient was calculated for a defect-free and unstrained material at 0 K. By providing a database of unexplored compounds to be explored, Jong et al.'s group took research related to piezoelectric materials a step further (Jong et al. 2015). Piezoceramic materials have a high piezoelectric coefficient, but they are fragile and require high processing temperatures. On the other hand, piezoelectric polymers are easy to process, lightweight, cost-efficient to fabricate, provide significant flexibility in designing and manufacturing devices, and also provide flexibility and stretchability to a device. Piezoelectric polymers may be an excellent alternative to piezoceramics in areas where they lack. The piezoelectric behavior of polymers can be enhanced by combining them with reinforcements. Some well-known piezoelectric polymers include PVDF and copolymers of fluorinated materials, and polyamide (Mishra et al. 2019; Ramadan 2014).

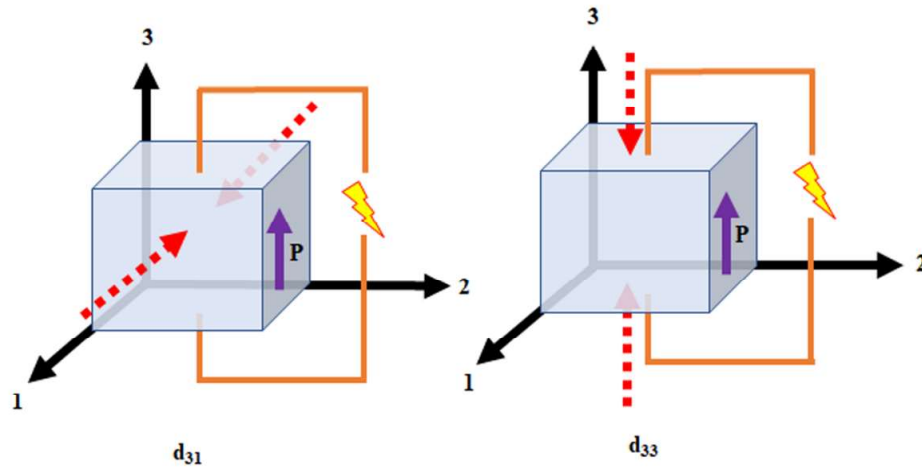


Fig. 1.3 Schematic of piezoelectric  $d_{31}$  and  $d_{33}$  configurations of piezoelectric materials (Chilabi et al. 2020).

### 1.1.2 Triboelectricity

The triboelectric effect is a phenomenon that occurs when two different materials come into contact with each other, resulting in the creation of electricity (Wang et al. 2016). Wang's research group first devised the triboelectric nanogenerator (TENG) in 2012 by integrating the triboelectric effect and electrostatic induction to scavenge ambient mechanical energy. TENG offers exceptional benefits, including a wide range of materials, lightweight, inexpensive, and excellent performance (Fan et al. 2012). Over the past decade, TENG has evolved into a concept that encompasses various working modes, enabling it to be applied to a variety of applications, including mechanical vibration (Chen and Wang 2017), biomechanical moments (Cho et al. 2020), wind (Chen et al. 2018), and blue energy (Khan and Kim 2016). In the age of the internet of things (IoT) and miniature devices, TENG may prove to be a cost-effective alternative energy source (Wang et al. 2016). In triboelectrification, charge transfer between two different materials occurs when they come in contact, where one material accepts the charges (tribo-negative) and the other loses the charges (tribo-positive). The electron affinity of the material dictates the nature of the material to accept/donate the charges. By their position in the triboelectric series (Table 1.1), it is possible to recognize the donor and acceptor. The greater the gap between two materials in the series, the higher

the charge transfer, which enhances the triboelectric performance. So, the selection of material for TENG is crucial for its performance (Wang et al. 2016).

Table 1.1 Triboelectric series (Kim et al. 2017; Wang et al. 2020).

|                                  |  |
|----------------------------------|--|
|                                  | Polyamide 11, Polyamide 6-6                |
|                                  | Wool, knitted                              |
|                                  | Silk, woven                                |
|                                  | Aluminium                                  |
|                                  | Paper                                      |
|                                  | Cotton, woven                              |
|                                  | Steel                                      |
|                                  | Wood                                       |
|                                  | Nickel, copper                             |
|                                  | Brass, silver                              |
|                                  | Acetate, rayon                             |
|                                  | Poly(methyl methacrylate) (Lucite)         |
|                                  | Poly(vinyl alcohol)                        |
|                                  | Poly(vinylidene chloride-co-acrylonitrile) |
|                                  | Poly(Bisphenol A carbonate)                |
|                                  | Poly(vinylidene chloride) (Saran)          |
|                                  | Polystyrene                                |
|                                  | Polyethylene                               |
|                                  | Polypropylene                              |
|                                  | Polyimide (Kapton)                         |
| Poly(vinyl chloride) (PVC)       |  |
| Polydimethylsiloxane (PDMS)      |  |
| Poly(vinylidene fluoride)        |  |
| Polytetrafluoroethylene (Teflon) |  |

### 1.1.2.1 Mechanisms of triboelectrification

The degree of triboelectrification determines the performance of the TENG. Thus, understanding the fundamental physics is vital to ensure optimal triboelectrification. In TENG, there is true uncertainty as to which type of charge transfer occurs, i.e., electron, ion, or material, during triboelectrification (Baytekin et al. 2011; McCarty and Whitesides 2008; Taylor and Lowell 1980). In triboelectrification, there is no universal charge transfer model that can perfectly represent triboelectrification. Identification of specific species transferred is challenging as they exist at the atomic scale, and the current technological limitations inhibit the accurate characterization of these species (Kim et al. 2021).

#### 1.1.2.1.1 Electron transfer model

The solid-state and electron cloud/potential well-based models (Xu et al. 2018a; b) were proposed to depict the electron transfer process in triboelectrification between the metal and dielectric/insulator. In the solid-state model (Fig. 1.4), the semiconductor band structure was used to depict electron transfer between the metal and the dielectric. Electrons at a higher energy level in metal hop onto a dielectric material's surface upon contact between them when  $E_F$  is higher than  $E_n$ . When the metal and dielectric material are separated, a small population of electrons at a higher surface state energy state return to metal. Some electrons remain on the dielectric material due to the potential barrier, which results in triboelectrification.

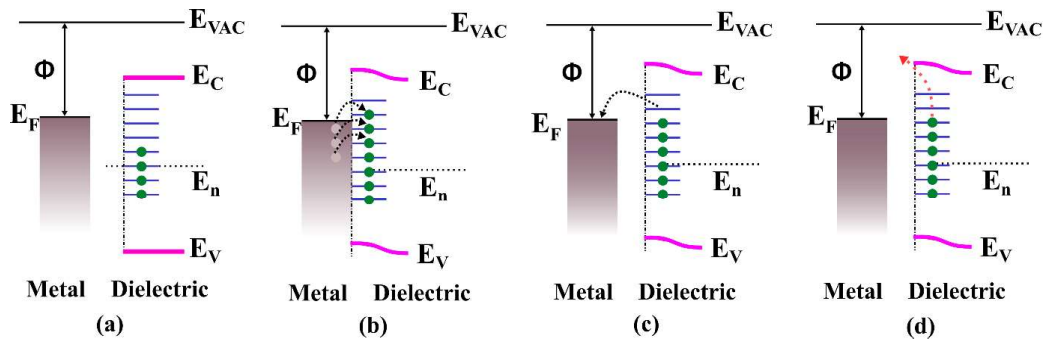


Fig. 1.4 The charge transfer between metal-dielectric (semiconductor) is explained using a modified solid-state model, (a) prior to contact, there is no exchange of charges,

(b) during contact, electrons present at a high energy level in metal transferred to the dielectrics/insulators, (c) after contact, some electrons return to the metal, and few remain on the surface of dielectric/insulators due to energy barrier, (d) Some charges are released due to thermionic effect.  $\Phi$ - metal work function;  $E_F$ -Fermi level;  $E_{VAC}$ -vacuum level;  $E_C$ -conduction band;  $E_V$ -valence band;  $E_n$ -neutral level of surface states (Xu et al. 2018b).

The electron cloud/potential well model is suggested to describe the triboelectrification process in general materials such as polymers and non-crystalline structures (Fig. 1.5). In this instance, a potential well could be used to illustrate the atom, where outer shell electrons are loosely coupled to form an electron cloud. The electron clouds of the two materials are distinct before atomic contact. The potential wells of two different materials overlap when they come in contact with each other and become asymmetric double-well potentials, resulting in electron transfer from one material to another (Fig. 1.5b). After separation, the electrons are retained on the other material due to the energy barrier. Thus, triboelectrification occurs between two materials.

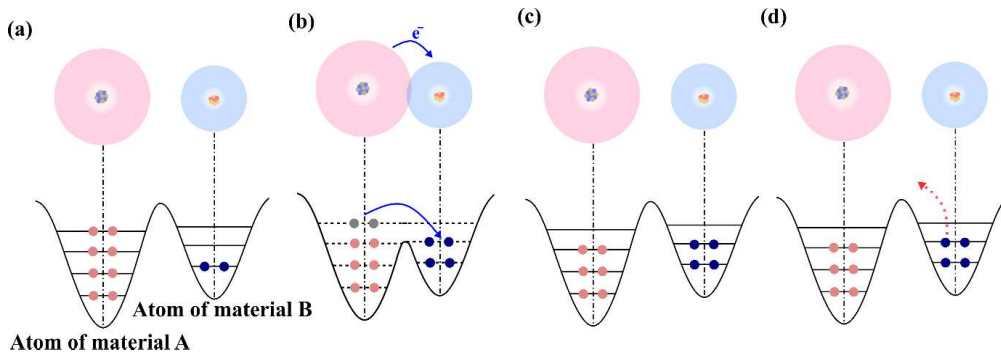


Fig. 1.5 Schematic of the electron cloud and potential well describing the charge transfer between two materials, (a) prior to contact, (b) at the time of contact, (c) after contact, (d) few charges are released due to thermionic effect (Xu et al. 2018b).

#### 1.1.2.1.2 Ion transfer model

Some studies suggest that instead of electrons, the mobile ions could be the charges which are transferred between two different materials (McCarty and Whitesides 2008;

Taylor and Lowell 1980). When two different materials come into contact with each other, ions may transfer from one material to another. When the materials separate, ions present on the surface are asymmetrically pulled apart, which gives rise to triboelectric charges. In ionic polymers, one ion is attached to the matrix, and a second ion with a different polarity acts as a moving charge, which facilitates triboelectrification (Kim et al. 2021). In non-ionic polymers, water ions play a crucial role in triboelectrification. All polymers adsorb water from the environment, and the ions of these water molecules ( $\text{OH}^-$  and  $\text{H}^+$ ) are asymmetrically separated during contact, which results in triboelectrification (Fig. 1.6) (Knorr 2011; McCarty and Whitesides 2008).

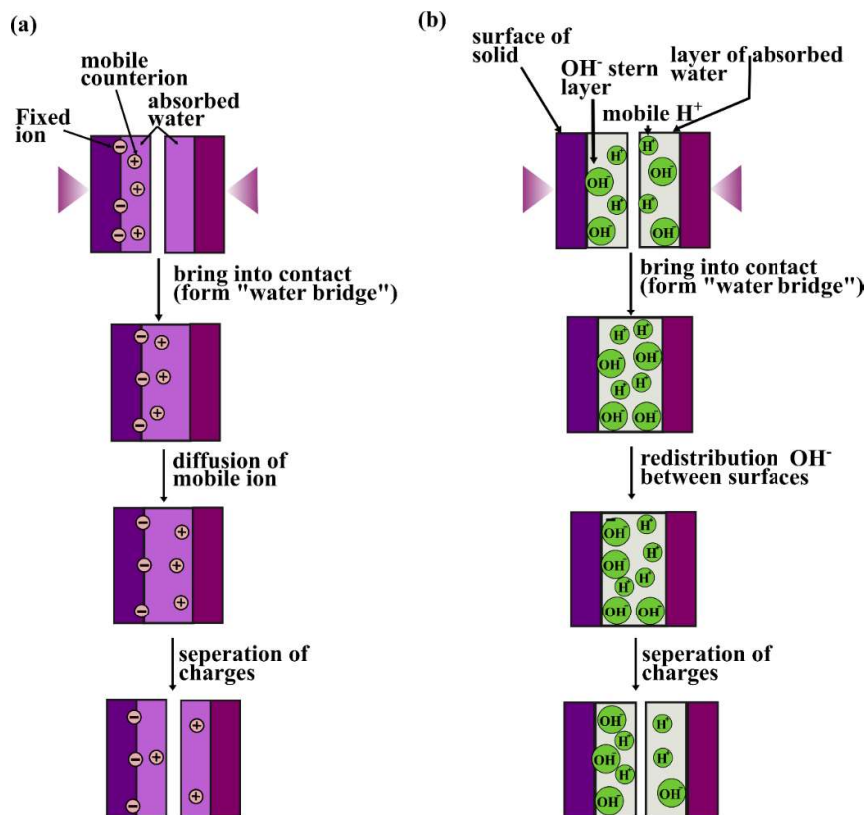


Fig. 1.6 Schematic (a) water bridge model describing ion transfer in the ionic polymer (Kim et al. 2021) (b) water bridge model describing asymmetrically redistributed  $\text{OH}^-$  and  $\text{H}^+$  causing ion transfer in non-ionic polymers (McCarty and Whitesides 2008).

### 1.1.2.1.3 Material transfer model

The transfer of material between two layers at a nanoscopic level can result in triboelectrification (Fig. 1.7). In polymeric materials, triboelectrification and material transfer often occur with bond cleavage. Triboelectrification results in the formation of mechanoions and mechanoradicals by breaking polymer chains (Baytekin et al. 2012; Sakaguchi et al. 2014; Sohma 1989). The heterolytic cleavage and homolytic cleavage mechanisms are responsible for the formation of mechanoions and mechanoradicals, respectively. In the heterolytic cleavage mechanism, positive and negative charges are formed at both ends of the polymer chain, whereas in the homolytic cleavage mechanism, there is no charge separation. The mechanoions and mechanoradicals are responsible for the triboelectrification in the material transfer model, and the formation process of both species is given below (Sohma 1989).

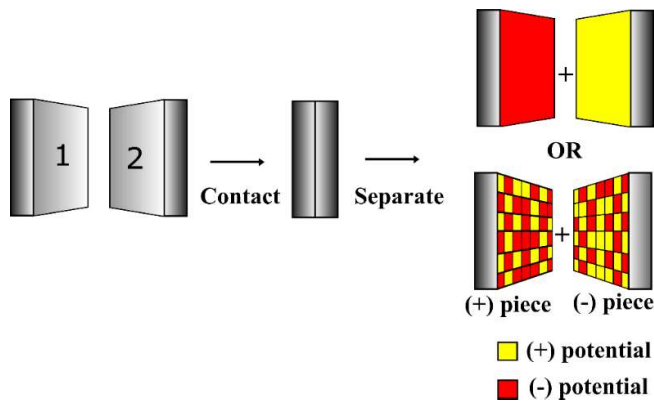
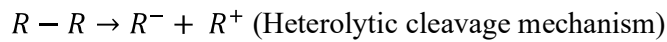
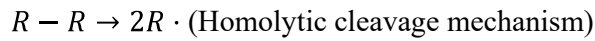


Fig. 1.7 Schematic of the theoretical mass transfer model involving charge transfer between two materials (Xu et al. 2018a).

### 1.1.2.2 Operational modes of TENG

The four modes of triboelectric nanogenerator are demonstrated based on the electrode, dielectric layer, and the relative motion (Fig. 1.8) (Wang et al. 2016).

### **1.1.2.2.1 Vertical contact-separation mode**

In vertical contact-separation mode, the relative motion between dissimilar materials is perpendicular to the interface. The two dissimilar materials are placed such that they face each other, and the other side of the materials is attached to the electrodes. When the materials come in contact with each other upon application of external force, the charge transfer occurs due to the triboelectric effect. Upon the separation, the remaining charges present on the surface induce opposite charges on the electrode due to electrostatic induction, which creates electrical potential. The developed electrical potential causes electrons to flow through the external circuit.

### **1.1.2.2.2 Lateral sliding mode**

The design of the TENG is similar to the vertical contact-separation mode; however, the relative motion between the two interfaces is parallel sliding to each other. Along the sliding direction, lateral polarization occurs, which drives the electron through the external circuit to balance the electrical potential created by the triboelectric effect and electrostatic induction.

### **1.1.2.2.3 Single electrode mode**

The previous modes discussed in 1 and 2 are two electrodes connected by the load. In some situations, if the moving object is used as the second material, it is difficult to connect the electrode to it. The single electrode mode has been introduced to harvest energy in such a situation. The bottom electrode is connected to the ground to withdraw charges generated during contact or sliding. To maintain the potential, electron exchange occurs across the bottom electrode and ground.

### **1.1.2.2.4 Freestanding triboelectric layer mode**

When a moving object, such as clothes, gloves, or shoes, contact makes contact with the ground or air, it becomes charged. The charges generated will accumulate and last for an extended period. When two symmetric electrodes are placed beneath a dielectric layer and have a similar size and gap between them as the size of the passing object,

they will produce an uneven charge distribution as the object passes by or moves away from these electrodes, which in turn causes electrons to transfer between the electrodes to compensate for the change in local potential. There is no physical contact between the moving part and the surface of the dielectric material.

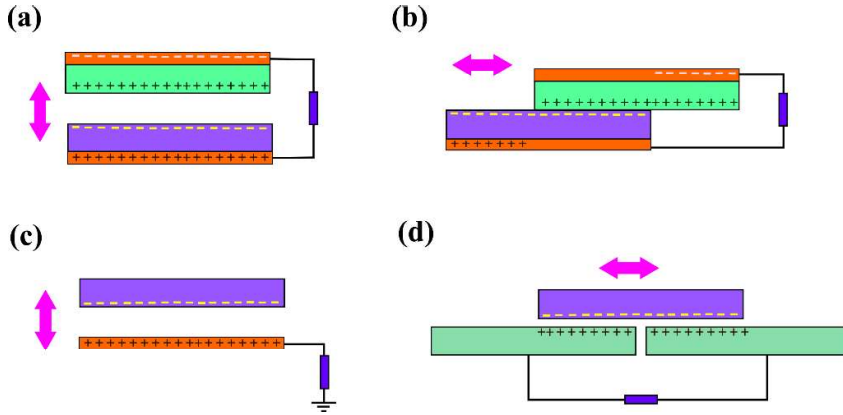


Fig. 1.8 Schematic of the different modes of triboelectric nanogenerators: (a) Vertical contact-separation mode, (b) in-plane contact-sliding mode, (c) single electrode mode, (d) freestanding triboelectric-layer mode.

### 1.1.2.3 Mathematical expression of contact-separation mode based TENG

#### 1.1.2.3.1 Displacement current of TENG by using the first-principle method

Displacement current is a fundamental parameter that directly impacts TENG output. The displacement current ( $J_D$ ) was postulated by Maxwell in 1861 (Wang 2020; Wang et al. 2017). The contribution of polarization due to the piezoelectric effect and or triboelectric effect to the displacement current can be taken into consideration and applied to the contact-separation mode of TENG. So, the modified displacement current equation can be written as (Wang et al. 2017);

$$I \approx A\sigma_C \frac{dx}{dt} \frac{\frac{d_1 \epsilon_0}{\epsilon_1} + \frac{d_2 \epsilon_0}{\epsilon_2}}{\left[ \frac{d_1 \epsilon_0}{\epsilon_1} + \frac{d_2 \epsilon_0}{\epsilon_2} + x \right]^2} \quad (1.3)$$

where  $d_1$  and  $d_2$  are thickness.  $\varepsilon_1$  and  $\varepsilon_2$  are the dielectric constants of the two different materials.  $\sigma_c$  is surface charge density,  $x$  is the distance of separation between two triboelectric materials, and  $I$  is output current.

### 1.1.2.3.2 V-Q-x equation for contact-separation mode TENG

The basic principle of TENGs is the combination of electrostatic induction and the triboelectric effect. TENG has inherent capacitive property since it is based on electrostatics. Any TENG's inherent capacitive behavior can be explained by V-Q-x, which serves as the governing equation for the determination of TENG electrical performance. The equation can be expressed as (Niu and Wang 2014):

$$V = -\frac{1}{C(x)}Q + V_{OC}(x) \quad (1.4)$$

where  $V$  is the voltage between two electrodes,  $V_{OC}$  is open circuit voltage,  $Q$  is the total charge transfer between the two electrodes, and  $x$  is the distance between two triboelectric materials.

The  $V_{OC}$  can be given as:

$$V_{OC} = \frac{\sigma_c x(t)}{\varepsilon_0} \quad (1.5)$$

### 1.1.3 Capacitive Sensing

A sensor is a device that produces signals by responding to physical or chemical responses. Due to technological advancements, sensors have become an integral part of human life. The flexible pressure/touch/tactile sensor got huge attention due to its flexibility, lightweight, better sensitivity, and quick response (Chen and Yan 2020; Xu et al. 2018c). Flexible pressure/touch/tactile sensors can be categorized into piezoresistive (Stassi et al. 2014), capacitive (Chen and Yan 2020), and piezoelectric (Emamian et al. 2015) based on their underlying operating principles. The capacitance-based flexible sensor performs better than the piezoelectric and piezoresistive sensors

in terms of simple design, stability, and energy efficiency (Emamian et al. 2015). During the application of external force, a capacitive sensor detects the change in capacitance value. The change in the capacitance value of the sensor upon the application of external force could be due to the change in the area or distance of the electrodes. Also, the dielectric constant of the material is a crucial factor in determining the sensitivity of the device (Chen and Yan 2020). The capacitance of the device can be measured using the following equation,

$$C = \frac{\epsilon_r \epsilon_0 A}{d} \quad (1.6)$$

where  $C$  is capacitance,  $\epsilon_r$  is dielectric constant,  $\epsilon_0$  is the permittivity of the vacuum,  $A$  is the area of overlapped electrodes, and  $d$  is the distance between two electrodes.

Equation 1.6 suggests that capacitance is influenced by the dielectric constant and the distance between electrodes. The sensitivity of a sensor is one of the most significant parameter that defines the sensor's performance. Sensitivity is expressed as the ratio of the change in capacitance to the external load, which represents precision and efficacy in real-life applications. The sensitivity of a sensor was calculated by taking the slope of the change in capacitance with respect to a load curve. The sensitivity of a flexible capacitive sensor can be enhanced in three ways. First, improving the dielectric constant of the polymer film. Second, increasing the contact surface area by micropatterning the polymer film/electrodes, and third, reducing the distance by incorporating porosity into the film (Li et al. 2021).

#### 1.1.4 PVDF

Kawai was the first to observe the piezoelectric effect in a stretched and polarized film PVDF. The importance of PVDF has grown with the discovery of its piezoelectric nature. PVDF is a semicrystalline polymer with a simple recurring part of  $-\text{CH}_2\text{-CF}_2-$ , with hydrogen and fluorine attached to its carbon backbone. PVDF displays five different phases depending on chain conformation, namely  $\alpha$ ,  $\beta$ ,  $\gamma$ ,  $\delta$ , and  $\epsilon$  (Fig. 1.9). In PVDF, the  $\alpha$ -phase is predominant and thermodynamically stable with chain conformation trans-gauche-trans-gauche' (TG TG'). The  $\beta$ -phase consists of all-trans

(TTTT) conformation, contributing to the highest dipole moment of  $8 \times 10^{-30}$  Cm compared to other phases and making it the most electroactive phase. The  $\gamma$ -phase is constructed with chain conformation of  $T_3GT_3G'$  and has a net dipole moment, making it an electroactive phase.  $\delta$  and  $\varepsilon$ -phase have conformation similar to  $\alpha$  (TGTG') and  $\gamma$  ( $T_3GT_3G'$ ) phase. The  $\alpha$  and  $\varepsilon$ -phases are nonpolar due to zero net dipole moment, attributed to their dipole's antiparallel packing (Martins et al. 2014). The  $\beta$ -phase exhibits excellent electrical characteristics and piezoelectric, pyroelectric, and ferroelectric properties. The  $\beta$  and  $\gamma$ -phases are also known as electroactive phases due to their electroactive nature.

Various techniques such as electrical poling (Dani et al. 2022), drawing or stretching (Sencadas et al. 2009; Wang et al. 2018), annealing (Sathiyaraju and Ramesh 2019a), solution casting (Salimi and Yousefi 2004), and spin coating (Yin et al. 2019), melt crystallization at high pressure (Jin et al. 2018), electrospinning, and addition of reinforcements have been used to transform the stable  $\alpha$ -phase into the electroactive phases.

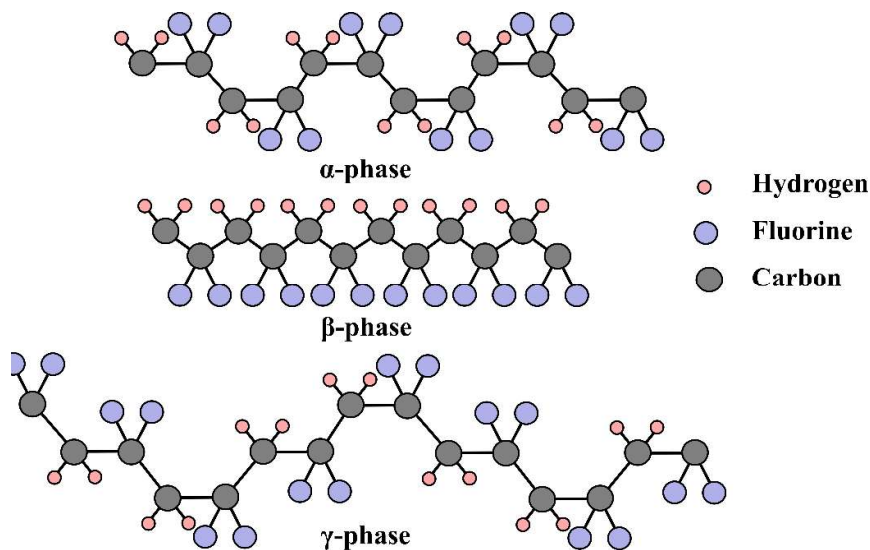


Fig. 1.9 Schematic of three major phases of PVDF.

Electrical poling is a well-established method to transform the  $\alpha$ -phase into the  $\beta$ -phase of the PVDF. Different poling methods, such as direct current poling (DCP), corona discharge poling (CDP), and alternating current poling (ACP), have been used

for the electrical poling of PVDF. The electrical poling strength, temperature, and time are governing parameters in electrical poling techniques which determine the formation of electroactive phase content (Dani et al. 2022). In the melt crystallization process, the formation of phases in PVDF is governed by melt temperature and pressure. The melt crystallization of PVDF results in a mixture of the  $\alpha$  and  $\gamma$ -phases. At lower melt temperatures (<153 °C- 155 °C), the PVDF consists of a predominant  $\alpha$ -phase, and at higher melt temperatures (>153 °C- 155 °C), it consists of a higher content of the  $\gamma$ -phase (Gregorio JR. and Capitão 2000; Lovinger et al. 1980). The stretching of PVDF film induces the electroactive phase at lower temperatures (Sajkiewicz et al. 1999). The effect of temperature during the stretching process on the electroactive phase of PVDF in the temperature range of 50 to 145 °C was investigated. The highest electroactive phase was obtained during drawing at 87 °C. A similar trend was observed by Liu et al., where the increase in  $\beta$ -phase content was observed with a drawing ratio up to 4 and 80 °C, beyond which it decreased (Liu and Jiayan 1998). The thermal treatment also influences the electroactive phase content and electrical properties of PVDF (Satthiyaraju and Ramesh 2019a; Ting et al. 2020). It has been reported that the  $\beta$ -phase dominates in solution-casted PVDF film at temperatures below 70°C (Gregorio and Cestari 1994; Salimi and Yousefi 2004). In the spin coating method, the electroactive phase can be controlled by controlling the spin-coating parameter and post-treatment conditions (Cardoso et al. 2011).

Electrospinning is a simple and cost-efficient method of preparing nanofibers. A key characteristic of electrospinning is that it is a one-step process that involves simultaneous electrical poling and stretching to induce an electroactive phase in PVDF (Kalimuldina et al. 2020; Martins et al. 2014). Moreover, it produces nanofabric of sufficient roughness to improve the TENG's contact surface area. Various reports have been published exploring the use of PVDF nanofabrics in real-life applications such as tactile/touch sensors (on robotic hands, on artificial skin) (Xin et al. 2016b), wearable sensors for physiological signal monitoring (pulse monitoring, respiration, and heartbeat monitoring, eating habit monitoring) (Xin et al. 2016a), energy harvesters (piezoelectric, triboelectric, pyroelectric, etc.) (Zi et al. 2015).

### 1.1.5 Electrospinning Process

Electrospinning is an easy and scalable technique to produce nanofibers. Cooley and Morton first documented the electrospinning process in 1902 (Andrady 2009). The essential requirements for the electrospinning process are a high voltage DC supply, viscous polymer solution/melt, ground electrode/collector, and spinneret (Fig. 1.10). The electrostatic force applied by the high voltage DC supply is used to prepare thin fibrils. Initially, the polymer solution is pumped into the spinneret. The droplet will form at the end of the spinneret and fall to the ground without an electric supply. The same trend will be observed until a high enough voltage is supplied. As enough high voltage is supplied and increased progressively, the droplets will deform and explode into several smaller droplets due to coulombic repulsion of charges in the absence of polymer chain entanglements. However, in the presence of sufficient polymer chain entanglement, the droplet deforms under the applied electric field and forms an elongated droplet, which assumes a cone-like shape, and the polymer jet is ejected. This cone is popularly known as the "Taylor cone." The narrow fibril ejected from the cone produces extra surface area to accommodate charges built on the surface of the jet and travels toward the ground. Above the critical applied voltage, the coulombic repulsion forces overcome the surface tension of the polymer solution, which deforms the droplet and increases surface charge so much that the polymer solution will be stretched to form fiber and increase surface area to accommodate the surface charges. The jet starts as soon as the applied voltage reaches beyond the critical voltage. The axial component of the coulombic repulsion in a jet is responsible for a straight elongated jet that passes toward the ground, which is known as a straight elongated segment. A straight elongated jet segment becomes unstable and exhibits a bending, waving moment as it travels towards the ground collector. This segment is known as the whipping instability region. In this regime, the evaporation rate of a solvent and the rate at which the surface area of fiber increases are high. As the solvent is evaporated during whipping instability, the solid nanofibers are collected over the collector (Andrady 2009).

Various parameters such as solution parameters (viscosity, molecular weight, solution conductivity, surface tension, and dielectric constant of solution), processing parameters (voltage, feed rate, tip-to-collector distance (TCD)), and ambient

parameters (temperature, humidity, type of atmosphere) administer the electrospinning process.

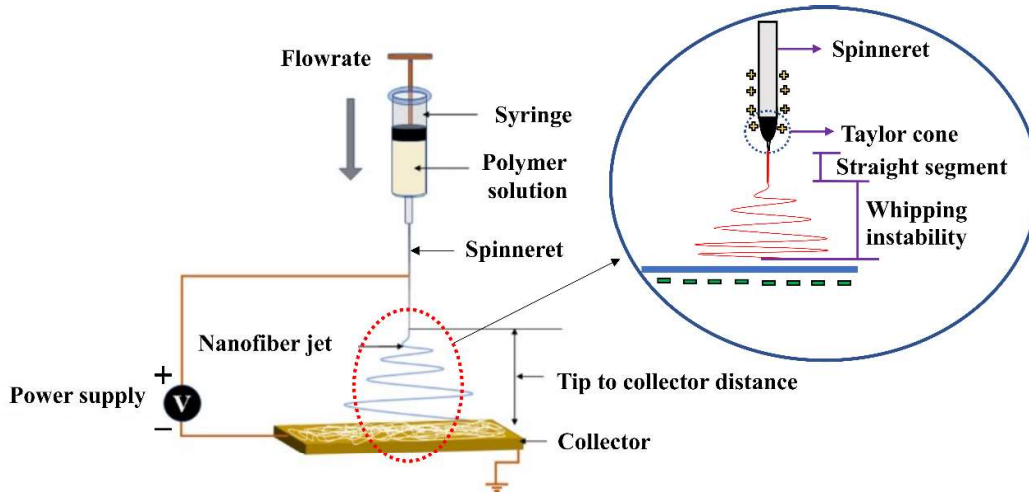


Fig. 1.10 Schematic of electrospinning setup and its components.

The concentration of polymer in the solution and the molecular weight of the polymer determines the viscosity of the precursor polymer solution. The viscosity of the polymer solution influences fiber diameter and morphology. It also helps to maintain polymer chain entanglement to avoid the breakup of droplets and form a continuous fiber (Beachley and Wen 2009; Fong et al. 1999; Zhu et al. 2017). The electrical conductivity of the polymer solution determines the charge mobility across the polymer solution, which assists in the stretching of the electrospinning jet under an applied electrical field. The electric charge should be high enough to create enough coulombic repulsive force to subdue the surface tension of the solution. In addition, enhancement in conductivity may result in an improved stretching effect to produce thinner fibers (Angamma and Jayaram 2011). Applied electrical voltage is also an influential factor that governs the electrospinning process. The high voltage induces the essential charges to initiate the electrospinning jet once the coulombic repulsive force subdues the surface tension of the solution. The feed rate, conductivity, viscosity of the solution, and tip-to-collector distance also need to be considered while deciding the applied voltage (Ramakrishna et al. 2005; Zhang et al. 2005; Zong et al. 2002). In the electrospinning process, the quantity of polymer solution available for electrospinning will be decided by the feed rate, and the feed rate can dictate the diameter and

morphology of fibers. The optimum feed rate is preferred by considering applied voltage, the evaporation rate of solvent, and tip-to-collector distance (Ramakrishna et al. 2005). The flight time available for the polymer solution and the electrical field strength is determined by the TCD. The change in TCD will influence flight time and electrical field strength, affecting the fiber diameter and morphology of the electrospun fiber. The optimal distance is preferable for desirable morphology and fiber diameter (Ramakrishna et al. 2005).

Humidity and temperature also have an impact on the diameter and morphology of electrospun fibers. An increase in temperature will reduce the viscosity of the polymer solution and increase the evaporation rate of the solvent, thus affecting the diameter and morphology of electrospun fibers. At relatively high humidity, moisture may condense on the fiber's surface, influencing the fiber's morphology. Also, higher humidity causes difficulty in drying of the fiber, resulting in wet fibers (Ramakrishna et al. 2005).

Electrospun nanofibers are intensely researched for applications like catalysis, energy harvesting, energy storage, photonics, and electronics. The electrospun nanofibers are also used as a membrane or electrode in solar cells, Li-ion batteries, supercapacitors, and fuel cell fabrication. The high porosity, large surface area, and high aspect ratio of nanofibers have made their way into the field of membrane technology, such as filtration, water treatment, selective absorption, air purification, and degradation of pollutants. In the biomedical field, they have been adapted by tailoring fiber diameter, porosity, biodegradability, surface modification, mechanical strength, and biocompatibility. The 2-D and 3-D scaffolds are fabricated and used in tissue engineering, bone tissue regeneration, and wound healing (Fig. 1.11) (Xue et al. 2019).

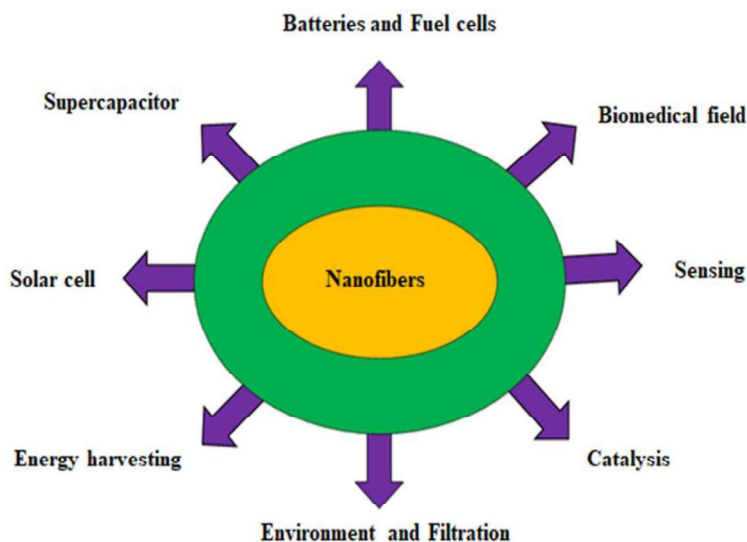


Fig. 1.11 Applications of electrospun nanofibers in various fields.

## 1.2 LITERATURE REVIEW

### 1.2.1 Electrospun PVDF doped/composite nanofabrics based piezoelectric nanogenerators

PVDF has several advantages over ceramic piezoelectric materials; however, the piezoelectric coefficient ( $d_{33}$ ) of PVDF is comparatively low. Electrospinning could enhance the piezoelectric output  $d_{33}$  value of PVDF by inducing the  $\beta$ -phase to some extent. Despite this, electrospinning alone may not be sufficient for real-life applications. Many researchers have attempted to improve piezoelectric performance by incorporating additives/fillers into PVDF. There is evidence that additives/fillers have significantly enhanced the piezoelectric performance of PVDF most of the time.

Salt/ionic liquid/surfactant (SIS) are used to enhance the piezoelectric performance of PVDF by increasing its electroactive phase content. SIS are mostly soluble in solvents, which leads to fine dispersion in the PVDF matrix, improving electroactive phase content and piezoelectric property. Dhakras et al. (2012) investigated the influence of hydrated salt ( $\text{NiCl}_2 \cdot 6\text{H}_2\text{O}$ ) on the  $\beta$ -phase and piezoelectric performance of electrospun PVDF nanofibers. A more significant effect

of adding salt is the enhanced  $\beta$ -phase content and piezoelectric performance due to ionic interactions between the polymer and the hydrated salt, as well as the polar solvent. The addition of room temperature ionic liquid (RTIL), i.e., 1-butyl-3-methylimidazolium hexafluorophosphate [BMIM][PF<sub>6</sub>], has resulted in the enhancement of the  $\beta$ -phase content in PVDF nanofiber mats. The remarkable improvement in the  $\beta$ -phase content was due to the interaction between the imidazolium ions of RTIL and CF<sub>2</sub> of the polymer chain (Xing et al. 2014). Yu et al. (2017) categorized the salt into three categories; the first category (I) is the salt that does not ionize in precursor solution and can be assumed in its molecular form. These molecules have zero or negligible dipole moments. Such salts will not affect electrospinning or the formation of the  $\beta$ -phase, so there will be no improvement in piezoelectric output compared to electrospun pristine PVDF. The second category (II) is of salts which can be separated into positive and negative charges and form electric dipoles upon addition to the solvent. Also, the addition of these salts causes an increment in the conductivity of the solution. The interaction between positive charge ion with fluorine atoms and negative charge ion with hydrogen atoms gives rise to the enhancement  $\beta$ -phase. The third category of salts can readily ionize in a precursor electrospinning solution, which is indicated by a substantial increase in the conductivity of a solution. The high conductivity of the precursor solution hampered the electrospinning process, resulting in being less effective compared to II categories of salts. A further detailed investigation was conducted on the influence of SnCl<sub>4</sub>.5H<sub>2</sub>O, Co(Ac)<sub>2</sub>.4H<sub>2</sub>O(I-category), CoCl<sub>2</sub>.6H<sub>2</sub>O, FeCl<sub>2</sub>.4H<sub>2</sub>O(II-category), MgCl<sub>2</sub>.6H<sub>2</sub>O, Co(NO<sub>3</sub>)<sub>2</sub>.6H<sub>2</sub>O (III-category) on the piezoelectric performance of PVDF.

0-D nanoparticles are particles that have all of their dimensions less than 100 nm. 0-D nanoparticles have attracted research attention because of their extremely small size and high specific surface area. Goncalves et al. (2015) investigated the impact of the addition of magnetic nanoparticles on the  $\beta$ -phase and the  $d_{33}$  value of PVDF under the influence of a magnetic field. The addition of CoFe<sub>2</sub>O<sub>4</sub> improved the  $\beta$ -phase content, which may be due to the interaction between the negatively charged particles ( $\zeta$ -potential of nanoparticle was -22 mV) and the positively charged CH<sub>2</sub> group of the polymer chain. The  $d_{33}$  value of nanocomposites was increased with an applied

magnetic field. BTO is an extensively explored and fascinating filler material. It improved the charge density of the electrospinning solution, thereby improving the stretching effect, which leads to an enhanced electroactive phase. Also, the electrostatic interaction between the BTO and polymer chain might have facilitated the promotion of the electroactive phase content. Additionally, the inherent piezoelectric nature also contributes to the enhanced piezoelectric performance of PENG (Chanmal and Jog 2011; Hussein et al. 2019; Jiang et al. 2020; Sharafkhani and Kokabi 2018). Moghadam et al. (2020) fabricated a self-powered wearable piezoelectric sensor using an electrospun PVDF/Metal-Organic Framework (MOF) nanofabric. The addition of MOF has enhanced the  $\beta$ -phase content, and the highest  $\beta$ -phase content of 75% was formed at 5 wt% loading of MOF. The enhanced  $\beta$ -phase could be due to the interaction between the carboxyl group (COOH) of MOF and the CF of PVDF. The highest piezoelectric constant was measured and found to be 212 mV/mm for 5% MOF loading.

1-D nanoparticles have an elongated structure with a diameter of less than 100 nm. 1-D nanoparticles such as nanotubes, nanowires, and nanorods have gained attention due to their unique and interesting properties by virtue of their size and high aspect ratio. A PVDF/CNT composite nanofiber mat was prepared to investigate the effect of CNT on the electroactive phase content. The incorporation of CNT resulted in the enhancement of the  $\beta$ -phase content. The enhanced  $\beta$ -phase content was due to the synergistic effect of the interfacial interaction and the stretching effect. The interfacial interaction could be due to strong donor-acceptor type interaction between CNT and fluorine at the interface (Huang et al. 2008). Khalifa et al. (2016) probed the synergistic effect of the addition of halloysite nanotubes (HNT) and the electrospinning process on the promotion of the  $\beta$ -phase content and piezoelectric response of PVDF. Incorporating HNT improved the  $\beta$ -phase content due to the combined effect of the intermolecular hydrogen bonding between the OH of HNT and the  $\text{CF}_2$  of PVDF and the interaction between the  $\text{CH}_2$  group of PVDF and the negatively charged surface of HNT. The maximum  $\beta$ -phase content of 81 % was observed at 10 wt% loading. Above 10 wt% loading of HNT, the  $\beta$ -phase was decreased, which may be due to excess HNT loading that reduced the polymer filler interaction. The highest piezoelectric response of 955 mV was observed under an applied load of 100 g. Li et al. (2019) studied the

role of particle morphology on the polymorphism and piezoelectric response of PVDF/ZnO composite-derived piezoelectric nanogenerators. The composites were prepared using ZnO nanoparticles (NPs) and ZnO nanorods (NRs) as fillers via the electrospinning process. The  $\beta$ -phase content of the PVDF-based composites was improved, which may be due to the nucleating effect caused by the interaction between negatively charged NPs/NRs and the positively charged  $\text{CH}_2$  of PVDF. PVDF/ZnO NRs-derived nanofibers showed higher  $\beta$ -phase content (90.7%) than PVDF/ZnO NPs nanofibers (87.5%), which may be attributed to the high aspect ratio of filler and better interaction caused by the proper orientation of NRs along the fiber axis. The NRs-based composite showed superior piezoelectric performance could be due to the higher  $\beta$ -phase content and the ability of piezoelectric NRs to deform under externally applied load. The piezoelectric  $V_{OC}$  and  $I_{SC}$  of NRs-based nanofiber were found to be 85 V and 2.2  $\mu\text{A}$ , respectively.

2-D nanoparticles are ultrathin sheet-like structures with a thickness of less than 100 nm and lateral dimensions larger than 100 nm. They have high specific surface area, which could provide strong interfacial interaction with polymer chains. The graphene-based composite nanofiber showed a reduction in the  $\beta$ -phase content upon the addition of graphene when compared to pure PVDF. The presence of graphene could have inhibited the crystallization of PVDF during solidification, which might be the reason for lower  $\beta$ -phase content. However, the  $d_{33}$  value of the PVDF/graphene composite was higher (19.2 pC/N) than electrospun pure PVDF nanofibers (15.2 pC/N). The interfacial polarization between reinforced graphene and PVDF might be the reason for the enhanced  $d_{33}$  value (Wu and Chou 2016). Electrospun PVDF/graphene oxide (GO)-based composite nanofibers were developed to study the impact of graphene oxide on piezoelectric and physical properties. The van der Waals interactions between the free electron pair that exists on the oxygen atom of GO and the negatively charged  $\text{CF}_2$  group of the PVDF chains resulted in the enhancement of the  $\beta$ -phase content (Issa et al. 2016). Khalifa et al. (2019) prepared a flexible piezoelectric nanogenerator based on graphitic-carbon nitride (g- $\text{C}_3\text{N}_4$ ) reinforced electrospun PVDF. The enhanced  $\beta$ -phase content was due to the hydrogen bonding between the hydroxyl groups of g- $\text{C}_3\text{N}_4$  and the PVDF chains. Also, the dipole-dipole interaction

between the oxygen atom of g-C<sub>3</sub>N<sub>4</sub> and CH<sub>2</sub> of the PVDF chain could have played a role. The highest  $\beta$ -phase content of  $\sim 80\%$ , and piezoelectric response of 7.5 V was generated from 0.75 wt% g-C<sub>3</sub>N<sub>4</sub>-based composite nanofiber. Shetty et al. (2019) studied the influence of organo-modified Ni-Co layered double hydroxide (OLDH) on polymorphism and piezoelectric behavior of electrospun PVDF. The functional interaction between OH of OLDH and CF group of PVDF chains and also possible interaction between sodium dodecylbenzene sulfonate (SDBS) ions and CH<sub>2</sub> group of PVDF chains has enhanced the  $\beta$ -phase content in resultant composite nanofibers. The highest  $\beta$ -phase content of 87.8% was observed at 3 wt% OLDH-based composites. The piezoelectric  $V_{OC}$ ,  $I_{SC}$ , and power density were found to be 6.9 V, 11.78 nA, and 0.92  $\mu\text{W}\cdot\text{cm}^{-2}$ , respectively, for the same the composite under human finger-tapping mode. In Table 1.2, an electrospun PVDF nanofabrics-based piezoelectric energy harvester with respective filler has been summarized.

### 1.2.2 Triboelectric Nanogenerators

Several materials have been explored as tribo-positive/tribo-negative materials for TENG. Mostly, poly(tetrafluoroethylene) (PTFE), polydimethylsiloxane (PDMS), fluorinated ethylene propylene (FEP), polyimide (PI), and PVDF are used as tribo-negative materials. Metal films such as copper and aluminium have been used as tribo-positive materials that can also act as an electrode. Apart from the metal films, polymeric materials such as nylon, poly(ethylene terephthalate) (PET), and polyurethane (PU) have been employed as tribo-positive materials (Zhang and Olin 2020). A great deal of research has been done on the improvement of the performance of TENG. These efforts have been categorized into different sections, such as meticulous selection of material, modification of material composition, and modification of surface and interface.

#### 1.2.2.1 Material composition modification

In material composition modification, the bulk material is incorporated with reinforcement to improve the dielectric property, thereby improving the surface charge density and the resultant triboelectric performance. The fillers with high dielectric

constant and different sizes, such as micro or nano, are added to improve the dielectric properties of polymer composites owing to interfacial polarization and the filler's superior dielectric properties. Ferroelectric materials have been used as reinforcement to enhance the triboelectric performance by improving dielectric properties. The fillers' inherent ferroelectric nature could also contribute to the improved triboelectric performance. Tao et al. (2019) also used BTO as reinforcement to prepare PVDF-based composite film. The triboelectric performance of the composite was enhanced upon the addition of BTO nanoparticles, and the highest  $V_{OC}$  of 900 V and a charge density of  $34.4 \mu\text{C}/\text{m}^2$  was generated in a composite film containing 10 wt% BTO nanoparticles. The superior triboelectric performance of composite film may be due to enhanced piezoelectric performance and dielectric constant. Soin et al. (2016) developed TENG using lead-free perovskite  $\text{ZnSnO}_3$ -based PVDF composite film using the phase inversion method. The composite containing 5 wt%  $\text{ZnSnO}_3$  was able to generate a  $V_{OC}$  of 520 V and a current density of  $2.7 \text{ mA}/\text{m}^2$ . The improvement in  $\beta$ -phase content and stress-induced polarization of  $\text{ZnSnO}_3$  contributes to better performance of composite film-based TENG. Liu et al. (2021a) utilize  $\text{BiFeO}_3$  lead-free perovskite to fabricate wearable TENG. The TENG consists of glass fiber fabric/ $\text{BiFeO}_3$ -PDMS composite film and silk nanofibers. The enhanced TENG performance was a combination of the piezoelectric response from  $\text{BiFeO}_3$  and the triboelectric effect. The 2-D material has garnered attention due to its distinctive properties, such as electrical, dielectric, and unique geometry. The 2-D reinforcements have been proven to enhance the triboelectric performance of the composite film. Parandeh et al. (2019) developed high-performance TENG based on poly(caprolactone)(PCL)/GO composite film and cellulose paper. A detailed investigation has been made on the effect of varying loading of GO on the triboelectric performance of TENG. The TENG containing 4 wt% of GO generated the highest  $V_{OC}$  of 120 V,  $I_{sc}$  of  $2.5 \text{ mA}/\text{m}^2$ . The improved triboelectric performance of TENG may be attributed to nanopores and enhanced negative charges due to the fibrous structure of PCL and the addition of GO. Chen et al. (2022) fabricated TENG based on silk embedded with nanoflake MOF. The SF containing 0.2 wt % of nanoflake MOF-based film generated a power density of  $\sim 263 \mu\text{W}/\text{cm}^2$ . The improved dielectric constant could be the reason for the enhancement of triboelectric performance.

### 1.2.2.2 Chemical modification of contact surface

The difference in electron affinity between two materials can be altered by chemical modification of the contact surface. Chemical modification can be done to make contact surfaces either more tribo-positive or tribo-negative. Thus, the surface charge density can be improved to maximize the difference in electron affinity between the two materials, which enhances the triboelectric performance of the TENG (Wang et al. 2016). Wang et al. (2016a) studied the effect of a self-assembled monolayer (SAM) on the triboelectric performance of TENG. The thiols and silanes with the different head groups were used to chemically alter the surface of Au and SiO<sub>2</sub>, respectively. The triboelectric performance of Au-based and SiO<sub>2</sub>-based TENG consisting of amine (-NH<sub>2</sub>) head group was significantly improved. Shen et al. (2017) used surface functionalization to manipulate the electron affinity of the substrate. PET was utilized as a substrate, on which its surface was functionalized with a series of halogens and amines functional groups to make the surface either tribo-positive or tribo-negative. The substrate functionalized with halogen groups acted as the tribo-negative layer, and the one functionalized with -NH<sub>2</sub> acted as the tribo-positive layer. The TENG with a tribo-negative layer containing -Cl group and tribo-positive poly(ether imide) showed a triboelectric output of 55 W/m<sup>2</sup>. Feng et al. (2016) fabricated TENG using gum wrapper-coated aluminium foil and electrospun PVDF nanofiber mat. The gum wrapper was chemically modified with polydopamine to enhance the surface polarity. The chemically modified TENG showed triboelectric performance 3.5 times compared to unmodified TENG. The maximum I<sub>SC</sub> and V<sub>OC</sub> of 30 μA and 1000 V were measured, respectively.

### 1.2.2.3 Physical modification of surface

The triboelectric performance of TENG is directly related to surface charge density of the material. So, numerous efforts have been made to improve the surface charge density of the triboelectric material to enhance triboelectric performance. The surface charge density is defined as the amount of charge per unit footprint area (C/m<sup>2</sup>). The effective surface contact area is different from the footprint area, as effective surface contact area could increase by physical modifications such as nano or micropatterning

and electrospinning. Thus, surface charge density can be increased by physical modification of the contact surface. Fan et al. (2012a) fabricated TENG comprised of the substrate with a regular and uniform array of micropatterns such as lines, pyramids, and cubes. The triboelectric performance of the patterned TENG was improved compared to flat film, and the highest  $V_{OC}$  was observed in pyramid patterned-based TENG. Lin et al. (2013) fabricated a pressure sensor with high sensitivity and quick response on the basis of the triboelectric effect. The substrate was micropatterned with a pyramid structure to enhance the contact surface area, thereby improving the pressure response of the device. In an effort to create microstructures on the surface of PDMS, argon plasma was employed. The enhanced surface contact area due to the microstructures has resulted in significantly improved triboelectric performance. The optimized micro-structured sample showed 2.6 times higher performance compared to smooth film (Cheng et al. 2017). Dong et al. (2021) investigated the state-of-the-art and worldwide influence of textile-based TENGs on the basis of publications and their regional distribution between the period of 2012 to 2020. Since the successful integration of TENGs with textiles in 2014, the number of articles retrieved on the subject of textile TENGs has steadily increased each year. The major countries in the world are involved in the research of textile-based TENGs, and the significant contributors include the Republic of China, the United States, and the Republic of Korea. In terms of institutions, the Chinese Academy of Sciences, Georgia Institute of Technology, University of Chinese Academy of Sciences, and Donghua University are leading institutions to be paramount in the field of textile-based TENGs. Based on the data analysis, it was predicted that textile TENGs are going through a rapid growth phase and will demonstrate even more advancement in the upcoming years (Fig. 1.12). Electrospinning could be a superior approach among the various methods available for synthesizing textile-based TENGs due to its simplicity, cost-effectiveness, and scalability. It also facilitates the physical modification of the substrate's contact surface, which significantly improves the triboelectric performance of TENG. Kim et al. (2020) demonstrated that electrospun PI had modified surface that exhibited better triboelectric performance than commercially available and screen-printed PI film.

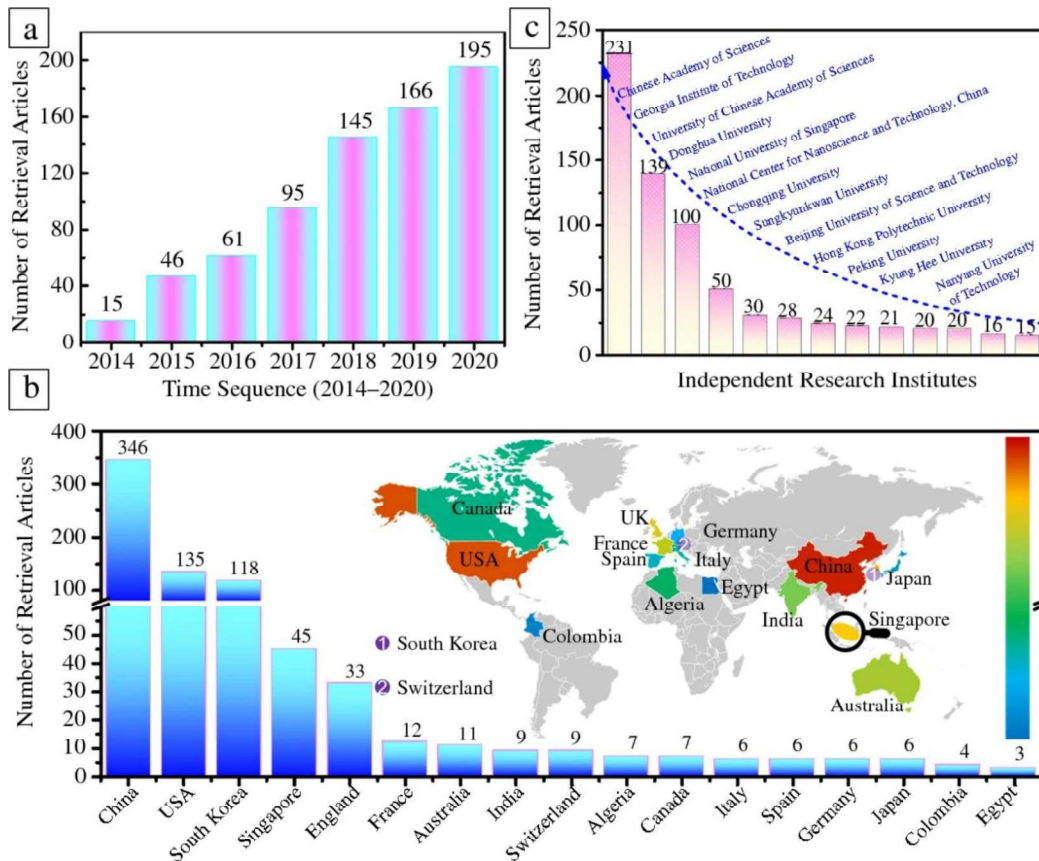


Fig. 1.12 The state of the art of textile-based TENGs based literature retrieved in the year 2012 to 2020; The articles on textile-based TENG were obtained according to (a) different years, (b) various nations, and (c) independent research institutes, respectively (Dong et al. 2021).

#### 1.2.2.4 Triboelectric nanogenerators based on composites of PVDF

The addition of reinforcements, chemical, and physical modification are proven techniques to enhance the triboelectric performance of TENG. The inherent piezoelectric nature of the filler or the substrate material could also add to the improvement of triboelectric performance. PVDF is well-known for its piezoelectric and dielectric properties and is also a suitable tribo-negative candidate for TENG. The electroactive phase content, nature of the filler, and processing technique are important factors that determine the dielectric properties and piezoelectric behavior of the PVDF. So, efforts have been made to improve the electroactive phase content and dielectric constant of PVDF by different methods. PVDF and its composites prepared using

different processes have been explored as tribo-negative materials with enhanced triboelectric performance.

Kim et al. (2017a) fabricated TENG based on PVDF composite film embedded with surface-functionalized MWCNT. The addition surface functionalized MWCNT improved the  $\beta$ -phase content. The triboelectric performance of TENG was enhanced upon the incorporation of functionalized MWCNT, and the highest  $V_{OC}$  of 16 V was recorded for PVDF composite film containing 1 wt% functionalized MWCNT. Cheon et al. (2018) fabricated TENG using electrospun PVDF nanofiber embedded with silver nanowire (AgNW) as tribo-negative material. The electroactive phase content and dielectric property were significantly improved with the addition of AgNW, which led to improvement in the triboelectric performance. The PVDF composite nanofiber containing 3 wt% of AgNW showed the highest triboelectric  $V_{OC}$  of 240 V at 5 N applied force. Choi et al. (2019) embedded graphene quantum dots (GQD) to prepare the PVDF composite nanofiber mat. The TENG fabricated using a nanofiber mat containing GQD showed superior performance compared to pristine PVDF nanofibers. The TENG based on a nanofiber mat containing 5 wt% GQD was able to produce the highest triboelectric  $V_{OC}$  of  $\sim 75$  V. The TENG was fabricated using an electrospun PVDF nanofiber mat impregnated with MXene nanosheets ( $Ti_3C_2T_x$ ). The addition of  $Ti_3C_2T_x$  nanosheets significantly enhanced the dielectric constant and surface charge density. The maximum power density of  $11.21 \text{ W/m}^2$  was observed in MXene-based TENG, which was 1.58 times more than that of pure PVDF nanofiber mat-based TENG (Bhatta et al. 2021). Shi et al. (2021) developed the triboelectric layer by the combination of electrospinning and incorporation of graphene. The addition of graphene significantly improved the dielectric constant and surface charge density. The electrospinning process introduced surface structures that improved the contact surface area. The enhanced  $\beta$ -phase content also contributed to improved triboelectric performance. Hence a superior performance of TENG with  $V_{OC}$  and  $I_{SC}$ ,  $\sim 1511$  V and  $\sim 189 \text{ mA/m}^2$ , respectively was recorded. Headu et al. (2022) fabricated self-poled  $MoS_2$  PVDF composite film as a triboelectric layer using a bar-printing method followed by postannealing. The enhanced triboelectric performance could be due to an improved electroactive phase and increased triboelectric trap states. The film

containing the optimized filler loading followed by postannealing generated a triboelectric  $V_{OC}$  and  $I_{SC}$  of  $\sim 200$  V and  $\sim 11.8$   $\mu A$ , respectively. Sim et al. (2022) developed PVDF composite nanofiber embedded with fullerene. The addition of the fullerene improved the electroactive phase content of PVDF. Also, the charge entrapment ability and electronegativity were boosted upon the incorporation of fullerene, which improved the triboelectric performance of the TENG. In Table 1.3, the performance of TENGs based on PVDF composites and corresponding tribo-positive materials is described.

### 1.2.3 Capacitive Sensors

The flexible capacitive sensor is used as a pressure sensor, tactile sensor, touch sensor, and force sensor in various applications such as eskin, wearable health monitoring systems, and robotic arms (Li et al. 2021). Different methods have been reported to enhance the performance of flexible capacitive sensors, such as altering the surface structure, distance, and dielectric properties of polymer film. Bao and coworkers first devised the capacitive sensor with a micropattern on dielectric material to enhance the performance of the sensor. The pyramid-type microstructure pattern was prepared on the PDMS dielectric film using a silicon mold. The pyramid-type micro-structured sensor showed better sensitivity when compared to line-type micro-structured and unstructured film. The sensor was able to achieve a sensitivity of  $0.55$   $kPa^{-1}$  (Mannsfeld et al. 2010; Wan et al. 2018). Lou et al. (2019) developed a capacitive sensor with a tilted micropillar structure by photolithography. The tilted pillar structure was more deformable, i.e., the change in distance between electrodes is much more effortless as the tilted pillar responds to bending deformation instead of compression. The sensor with a sensitivity of  $0.42$   $kPa^{-1}$  and a lower detection limit of  $1$  Pa was developed with a tilted pillar. A bionic micropatterned PDMS tactile sensor with high sensitivity was developed using the lotus leaf as a template. The PDMS film was coated with ultrathin AgNWs film to employ the same as an electrode. The sensor was able to sense as low as  $0.8$  Pa pressure and was able to achieve a sensitivity of  $1.2$   $kPa^{-1}$  (Wan et al. 2018). The addition of reinforcement into dielectric material could increase the film's dielectric constant, thereby enhancing the sensor's performance. The spin-coated AgNW doped

PU film was prepared with different concentrations of AgNW. The sensitivity of the composite film sensor was  $5.5 \text{ kPa}^{-1}$  ( $<30 \text{ Pa}$ ) and  $0.88 \text{ kPa}^{-1}$  ( $>30 \text{ Pa}$ ), whereas, for pure PU film, the sensitivity was  $0.5 \text{ kPa}^{-1}$  ( $<30 \text{ Pa}$ ) and  $0.23 \text{ kPa}^{-1}$  ( $>30 \text{ Pa}$ ). The composite-based dielectric sensor showed superior performance compared to pure PU (Wang et al. 2015). Rana et al. (2016) used ferroelectric materials to enhance the dielectric constant of the film. The addition of ferroelectric BTO improved the dielectric constant as well as the sensitivity of the capacitive sensor. Upon application of an external pressure, porous dielectric film can reduce the distance between the electrode and gradually reduce pores, increasing the effective dielectric constant of the film, which increases the capacitance as well as the overall dielectric constant of the film. Kwon et al. (2015) developed porous Ecoflex elastomer film for the capacitive sensors. Ecoflex was cured along with a sugar cube and then washed with water to prepare porous Ecoflex dielectric film. The sensitivity of the sensor was measured and found to be  $0.601 \text{ kPa}^{-1}$  upon the application of pressure less than  $5 \text{ kPa}$ , and it also was able to sense pulse in real-time. The foaming agent ammonium bicarbonate ( $\text{NH}_4\text{HCO}_3$ ) was added to the PDMS solution, and the resultant solution was then heated to form a porous structure. The sensitivity of porous dielectric film was significantly enhanced when compared to the non-porous film (Chen et al. 2016b). Yang et al. (2019) used electrospinning to fabricate the porous dielectric film. Further, to improve the dielectric constant of the nanofiber mat, carbon nanotubes were added to PVDF. The sensor showed a sensitivity of  $0.99 \text{ kPa}^{-1}$ , which was significantly higher than that of pure PVDF nanofiber mat ( $0.09 \text{ kPa}^{-1}$ ).

Table. 1.2 Piezoelectric performance of PVDF-based doped/composite nanofabrics.

| Fillers and size in nm                 | Solvent          | Diameter of nanofiber (nm) | Remark  | Reference              |
|--|------------------|----------------------------|---|------------------------|
| (NiCl <sub>2</sub> .6H <sub>2</sub> O) | DMF              | 60-220                     | The peak-to-peak output voltage of ~0.762 V and enhanced $\beta$ -phase content of 92 % were recorded.  | (Dhakras et al. 2012)  |
| LiCl                                   | DMF and acetone  | -                          | The highest $\beta$ -phase and piezoelectric $V_{oc}$ of 94% and 5 V were noted.  | (Mokhtari et al. 2020) |
| BiCl <sub>3</sub>                      | DMF and acetone  | -                          | PENG doped with BiCl <sub>3</sub> produced a $V_{oc}$ of 1.1 V when connected to a vibrating table, which is 4.76 times pure PVDF-based PENG. The $\beta$ -phase content of 80% was recorded for 2 wt% of BiCl <sub>3</sub> . | (Chen et al. 2020)     |
| AuNCs                                  | DMF and acetone  | ~434±72                    | Highest output voltage ~18.3 V, Display an enhanced $\beta$ -phase of 93.2%.  | (Li et al. 2018)       |
| BTO ( $\leq 100$ nm)                   | DMSO and acetone | 100-600                    | The highest piezoelectric $V_{oc}$ of 6-8 V was noted.  | (Hussein et al. 2019)  |
| ZnO (Avg. size ~15 nm)                 | DMF and acetone  | ~747                       | The maximum $\beta$ -phase content and piezoelectric response were reached at 87% and 1.1 V, respectively.  | (Bafqi et al. 2015)    |
| Ag nanoparticles (25-40 nm)            | DMF and acetone  | 400-650                    | The highest piezoelectric response (2 V for 30 Hz frequency) was recorded at a reasonably low loading of silver nanoparticles, i.e., 0.4%. The $\beta$ -phase content was enhanced to 81%.                                    | (Issa et al. 2017)     |

## CHAPTER 1

|                                      |                  |              |  |                                |
|--------------------------------------|------------------|--------------|--|--------------------------------|
| TiO <sub>2</sub>                     | DMF and acetone  | and 300-400  | The highest d <sub>33</sub> value of 30.7 pC/N was recorded for 2% TiO <sub>2</sub> loading.   | (Zhu et al. 2019)              |
| ZnO (50-80 nm)                       | DMAc and acetone | and ~225-250 | Upon the addition of relatively low loading, i.e., 0.1 wt%, the β-phase content was improved to 74.24% from 55.29%. The d <sub>33</sub> value was also improved from 8.29 to 13.42 pC/N.         | (Sathiyaraju and Ramesh 2019b) |
| Functionalized MWCNT                 | DMAc and acetone | and <1 μm    | The electrostatic interaction between PVDF and the surface functional group of MWCNT has promoted the β-phase content. The highest β-phase content of ~47% was observed for 1% loading of MWCNT. | (Ahn et al. 2013)              |
| Cellulose nanocrystal (CNC) (~15 nm) | DMF and acetone  | and -        | CNC-based PVDF composite showed improvement in β-phase content and the highest β-phase content of 86.96%, and the piezoelectric response of 40-60 V was observed.                                | (Fu et al. 2017)               |
| MWCNT (10-20 nm)                     | DMF              | 110-160      | The β-phase content of 89% and d <sub>33</sub> of 31.3 pC/N were achieved.   | (Wu et al. 2018)               |
| Carbon nanofibers (~100 nm)          | DMF              | 300-700      | Displayed piezoelectric V <sub>OC</sub> of 5.8 V and I <sub>SC</sub> of 1.2 μA   | (Kumar et al. 2019)            |
| Organically modified Nanoclay        | DMF and acetone  | and -        | Showed the highest electroactive phase content of 90% and piezoelectric response of 70 V/68 μW cm <sup>-2</sup> .  | (Tiwari et al. 2019)           |
| GO                                   | DMF and acetone  | and -        | The highest electroactive phase content of 96% and V <sub>OC</sub> of 7 V was recorded for 1 wt% of GO.  | (Roy et al. 2019)              |
| hBN nanoflakes                       | DMF and acetone  | and 100-500  | The maximum β-phase content of 86% was achieved for reinforcement of 0.4 wt% hBN loaded PVDF composite. The piezoelectric V <sub>OC</sub> /I <sub>SC</sub>                                       | (Yadav et al. 2020)            |

## CHAPTER 1

---

and power density were 68 V/0.1  $\mu$ A and 53.2  $\mu$ W/cm<sup>2</sup> for the same composite, respectively.

---

|                                |                 |         |  |                        |
|--------------------------------|-----------------|---------|--|------------------------|
| Ca-Al layered double hydroxide | DMF and acetone | 200-400 | The PVDF/Ca-Al LDH with 5 wt% loading exhibited the highest $\beta$ -phase content of 82.7%. The maximum piezoelectric $V_{OC}$ of 5.7 V was recorded for the same composite under mechanical vibration of 20 Hz.  | (Shamitha et al. 2020) |
| Talc nanosheet                 | DMF and acetone | 200-400 | The highest $\beta$ -phase content of 89.6 % was displayed for 0.5 wt% of the talc-based composite fabric. Also, the highest of 9.1 V, 16.5 nA, and 1.12 $\mu$ Wcm <sup>-2</sup> of piezoelectric $V_{OC}$ , $I_{SC}$ , and power density were recorded, respectively. | (Shetty et al. 2020)   |

---

Table 1.3 Triboelectric performance of PVDF-based composites.

| PVDF-based tribo-negative layer         | Counter tribomaterial | Method                  | Voltage (V) | Current                       | Power density                | Reference               |
|---|-----------------------|-------------------------|-------------|-------------------------------|------------------------------|-------------------------|
| PVDF/ AgNW                              | Nylon                 | Electrospinning         | 240         | 12 $\mu$ A                    |                              | (Cheon et al. 2018)     |
| PVDF/ Fe <sub>3</sub> O <sub>4</sub>    | Al                    | Electrospinning         | 138         | 5.68 $\mu$ A                  |                              | (Im and Park 2018)      |
| PVDF/Graphene                           | Polyamide-6 (PA6)     | Electrospinning         | 1511        | 189 mA/m <sup>2</sup>         | 130.2 W/m <sup>2</sup>       | (Shi et al. 2021)       |
| PVDF/printer ink                        | PET                   | Electrospinning         | 1600        | 130 $\mu$ A                   | 22 W/m <sup>2</sup>          | (Tayyab et al. 2020)    |
| PVDF                                    | Mustard Seed          | Electrospinning         | 84          | -                             | 334 mW/m <sup>2</sup>        | (Singh et al. 2019)     |
| PVDF/GQD                                | Al                    | Electrospinning         | ~75         | ~2 $\mu$ A                    | 2.7 $\mu$ W/cm <sup>2</sup>  | (Choi et al. 2019)      |
| PVDF/Fullerene                          | Al                    | Electrospinning         | ~80         | ~2 $\mu$ A/cm <sup>2</sup>    | 70.5 $\mu$ W/cm <sup>2</sup> | (Sim et al. 2022)       |
| PVDF/ZnO                                | PTFE                  | Solution cast           | 119         | 1.6 $\mu$ A                   | 10.6 $\mu$ W/cm <sup>2</sup> | (Singh and Khare 2019)  |
| PVDF/BTO                                | Nylon                 | Doctor-blade            | 131         | 1.025 $\mu$ A/cm <sup>2</sup> |                              | (Kang et al. 2020)      |
| PVDF/dopamine-treated SnO <sub>2</sub>  | Paper                 | Doctor-blade            | 60          | 0.380 $\mu$ A/cm <sup>2</sup> | 81 $\mu$ W/cm <sup>2</sup>   | (Paranjape et al. 2022) |
| PVDF/BTO                                | PA6                   | Spin coating            | 900         | 10 mA/m <sup>2</sup>          | -                            | (Tao et al. 2019)       |
| PVDF/ZnSO <sub>3</sub>                  | PA6                   | Spin coating            | 500         | 2.7 mA/m <sup>2</sup>         | 0.47 W/m <sup>2</sup>        | (Soin et al. 2016)      |
| PVDF/ Gd <sub>5</sub> Si <sub>4</sub>   | PA6                   | Phase-inversion process | ~425        | ~30 mA/m <sup>2</sup>         | -                            | (Harstad et al. 2019)   |
| PVDF/ Ti <sub>0.87</sub> O <sub>2</sub> | Cu                    | Solution cast           | 52.8        | 5.69 $\mu$ A/cm <sup>2</sup>  | -                            | (Wen et al. 2018)       |
| PVDF/Zn-Al-LDH                          | PET                   | Spin coating            | 230.6       | 5.6 $\mu$ A/cm <sup>2</sup>   | -                            | (Ippili et al. 2021)    |

### 1.3 PROBLEM IDENTIFICATION

In recent years, energy harvesting devices have attracted the attention of researchers as an alternative power source for miniature and wearable devices and internet of things. The piezoelectric and triboelectric effect-based nanogenerators have garnered substantial interest due to their ease of operation, adaptability, and high conversion effectiveness. Ceramic-based piezoelectric materials exhibit superior performance owing to their higher piezoelectric coefficients. However, their fragile nature and difficulty in intricate designs restrict their use in various applications, which opens the door for polymeric materials. In triboelectric energy harvesters, PTFE and PDMS have commonly utilized materials due to their ease of processibility and tribo-negative characteristics. However, the low dielectric constant and the absence of inherent piezoelectric nature limits their triboelectric performance. PVDF is a potential candidate with several advantages over ceramics, including its flexibility, ease of processing, and failure at high elongation, making it an appealing alternative in several applications. PVDF exhibits the highest piezoelectric coefficient and dielectric constant among polymeric materials, while its electronegativity is the highest after PTFE. However, PVDF's electrical response is limited by its low dielectric constant and relatively low electroactive phase content, which hinders its practical use in real-life applications. These challenges can be surpassed by using nanofillers and electrospinning together in a synergistic way which provides a coherent approach that improves the electroactive phase content and dielectric properties of PVDF. Therefore, the purpose of this study is to investigate the tuning of the piezoelectric and triboelectric properties of electrospun PVDF nanofabrics with carefully added nanofillers.

### 1.4 SCOPE AND OBJECTIVES OF THE PRESENT WORK

#### 1.4.1 Scope

PVDF could be a potential candidate to develop high-performance energy harvesting devices. PVDF has been intensively researched in the past decades for its use in piezoelectric and triboelectric energy harvesters and sensors. Several nanomaterials are responsible for increasing the electroactive phase content and dielectric property in

PVDF, including carbon nanotubes, graphene, nanoclay, silica, and titanium oxide. Electrospinning can induce electroactive phase formation in PVDF, which is a simplified and more readily scalable approach. Electrospinning and filler-polymer interaction significantly improve the electroactive phase content, contact surface area, and dielectric constant, which make PVDF suitable for energy harvesting and sensing application. The primary objective of this research is to synthesize the PVDF-based nanofabric incorporating either a cationic surfactant or a couple of carefully chosen nanofiller without surface modification. The focus is on enhancing the dielectric properties, piezo capacitive sensing, piezoelectricity, and triboelectric properties of PVDF.

### 1.4.2 Objectives

1. To synthesize PVDF/cationic surfactant doped nanofabrics.
2. To synthesize PVDF/mica nanosheet composite nanofabrics.
3. To synthesize PVDF/BaWO<sub>4</sub> composite nanofabrics.
4. To explore the structural and morphological aspects of these nanofabrics.
5. To study the piezo capacitive sensing, piezoelectric and triboelectric response of these nanofabrics.



# **CHAPTER 2**



## CHAPTER 2

### MATERIALS AND METHODS

---

*This chapter provides a primary focus on the materials employed in the production of PVDF based doped/composite nanofabrics. It delves into the preparation of the precursor solution and the synthesis of nanofabrics using the electrospinning process. The synthesis process of barium tungstate nanorods is also explained in detail. Brief descriptions of the characterization techniques used to examine the synthesized materials are included. Moreover, the chapter encompasses the evaluation of PVDF based doped/composite nanofabrics for various applications.*

#### 2.1 MATERIALS

PVDF (Solef 1015, Solvay, Italy) ( $\overline{M}_w = 575,000$ ) was obtained from Prakash Chemicals, India. Tetra-n-butyl ammonium chloride hydrate (TBAC) was procured from Alfa Aesar, India. N, N- dimethyl formamide (DMF), acetone, barium nitrate ( $\text{Ba}(\text{NO}_3)_2$ ), sodium tungstate dihydrate ( $\text{Na}_2\text{WO}_4 \cdot 2\text{H}_2\text{O}$ ), cyclohexane, Triton X-100 (non-ionic surfactant) were purchased from Molychem, India, and 1-hexanol was procured from TCI chemicals, India. The mica nanosheets (purity of >99%) (particle size < 80 nm) were procured from Nanoshell, UK.

#### 2.2 METHODS

##### 2.2.1 Electrospinning of TBAC-doped PVDF nanofabrics

Electrospinning solution had a concentration of 13.5% w/v of PVDF in DMF. 1, 2, 3, and 5 wt% of TBAC were added to the PVDF solution based on the weight of PVDF, and the mixture was stirred at 30 °C for 8 h. The resultant solution was loaded to a 10 mL syringe with a 22 G hypodermic needle with a beveled tip. The following optimized parameters were used for the synthesis of electrospun nanofibers: flow rate – 0.6 mL/h; drum collector speed – 1500 rpm; tip to collector distance – 17 cm; applied voltage – 18 kV; RH –  $55 \pm 2\%$ ; and temperature – 30 °C.

### 2.2.2 Synthesis of barium tungstate nanorods (BWN)

The BWN were synthesized using the reverse microemulsion method mentioned elsewhere (Zha et al. 2019).

#### **Part 1:** synthesis of $\text{Na}_2\text{WO}_4$ microemulsion

A beaker was filled with 25 ml of cyclohexane, 3.39 ml of Triton X-100 (surfactant), and 2 ml of 0.2 M aqueous  $\text{Na}_2\text{WO}_4$  solution in sequence under constant magnetic stirring (500 rpm). Then, 1.38 ml of 1-hexanol (co-surfactant) was added, and the resultant mixture was vigorously stirred at 1000 rpm for 15 min to create a transparent reverse microemulsion.

#### **Part 2:** synthesis of $\text{Ba}(\text{NO}_3)_2$ microemulsion

$\text{Ba}(\text{NO}_3)_2$  microemulsion was prepared using a similar method as mentioned in part 1, replacing  $\text{Na}_2\text{WO}_4$  solution with  $\text{Ba}(\text{NO}_3)_2$  solution.

The  $\text{Ba}(\text{NO}_3)_2$  microemulsion was gently added to the  $\text{Na}_2\text{WO}_4$  microemulsion under gentle stirring, and the mixture was allowed to turn into white and turbid. The resultant mixture was kept at 50 °C for 24 h and allowed to form a white precipitate. The precipitate was separated using a centrifuge, washed and cleaned using ethanol five times to remove the residual surfactant and organic solvent, and then dried at 60 °C in a hot air oven for 12 h to obtain the BWN.

### 2.2.3 Electrospinning of PVDF/BWN Composite Nanofabrics

About 13.5 w/v% solution of PVDF in a 9:1 mixture of DMF and acetone was prepared to synthesize EPVDF nanofabric. For synthesizing the composite nanofabrics, accurately weighed BWN (0.5, 1, 1.5, 2, 3, and 5 wt% based on the weight of PVDF) was added to 10 mL of the mixed solvents. The resultant dispersion was ultrasonicated for 90 min, then 1.35 g of PVDF was slowly added to it under constant magnetic stirring. The mixture was magnetically stirred for 10 h to ensure homogeneity. The aforementioned PVDF solution/homogenized mixture of PVDF and BWN was transferred to 10 mL syringes fitted with 22-gauge stainless steel needles and subjected to electrospinning at  $28 \pm 2$  °C under the optimized conditions as follows: applied

voltage 18 kV; flow rate 0.6 mL/h; spinneret TCD 17 cm; rotating drum collector speed 1500 rpm; relative humidity  $50 \pm 2\%$ .

#### **2.2.4 Electrospinning of PVDF/mica nanosheets (MNS) Composite Nanofabrics**

A precursor solution was prepared by dissolving PVDF powder (13.5 wt/v%) in a 9:1 mixture of DMF and acetone. The mixture was stirred for 10 h to ensure complete dissolution of PVDF and electrospun to prepare EPVDF nanofabric. The composite nanofabrics were synthesized by adding an accurately weighed amount of MNS (0.25, 0.5, 0.75, and 1 wt% based on the weight of PVDF) to PVDF solution. Initially, a dispersion of MNS was prepared in the mixed solvent. The mixture was probe-sonicated for 40 minutes, and then 1.35 g of PVDF was added under continuous magnetic stirring and kept for 10 h. Subsequently, the resultant solution was loaded into a syringe equipped with a 22-gauge beveled stainless steel needle and subjected to electrospinning using the following parameters: applied voltage of 18 kV, a flow rate of 0.6 mL/h, a TCD of 17 cm, a rotating drum collector speed of 1500 rpm, a relative humidity of  $50 \pm 2\%$ , and a temperature of  $28 \pm 3^\circ\text{C}$ . Table 2.1 provides the notation used for PVDF based nanofabrics.

Table 2.1 Notations used for the PVDF based nanofabrics.

| <b>Nanofabrics</b>                        | <b>Dopant/Filler</b> | <b>Dopant/Filler loading<br/>(wt%) based on the<br/>weight of PVDF</b> |
|---|----------------------|--|
| <b>PVDF/TBAC doped<br/>nanofabrics</b>    |                      |  |
| EPVDF                                     |                      | 0  |
| PVDF/TBAC-1                               | TBAC                 | 1  |
| PVDF/TBAC-2                               | TBAC                 | 2  |
| PVDF/TBAC-3                               | TBAC                 | 3  |
| PVDF/TBAC-5                               | TBAC                 | 5  |
| <b>PVDF/BWN composite<br/>nanofabrics</b> |                      |  |
| EPVDF                                     |                      | 0  |
| PVDF/BWN-0.5                              | BWN                  | 0.5  |
| PVDF/BWN-1                                | BWN                  | 1  |
| PVDF/BWN-1.5                              | BWN                  | 1.5  |
| PVDF/BWN-2                                | BWN                  | 2  |
| PVDF/BWN-3                                | BWN                  | 3  |
| PVDF/BWN-5                                | BWN                  | 5  |
| <b>PVDF/MNS composite<br/>nanofabrics</b> |                      |  |
| EPVDF                                     |                      | 0  |
| PVDF/MNS-0.25                             | MNS                  | 0.25   |
| PVDF/MNS-0.5                              | MNS                  | 0.5  |
| PVDF/MNS-0.75                             | MNS                  | 0.75   |
| PVDF/MNS-1                                | MNS                  | 1  |

### 2.3 MEASUREMENT AND CHARACTERIZATION

Scanning electron microscopy (SEM) (JSM-6380LA, JEOL, Japan) was used to study the morphology of the gold-sputtered TBAC-doped PVDF nanofibers. The morphologies of MNS, BWN, and composite nanofibers were investigated by field emission scanning electron microscopy (FESEM) (Zeiss GeminiSEM 300 FESEM, Germany). The nanofibers were gold-sputtered prior to FESEM imaging. Image-J software (Schneider et al. 2012) was used for the measurement of fiber diameter. The average fiber diameter (AFD) and standard deviation (SD) of the nanofibers were calculated by measuring the diameter of 50 fibers at three different locations. The average diameter and SD of BWN were also calculated using the image-J tool; 50 nanorods were chosen for the measurement. Also, a transmission electron microscope was employed to image the composite nanofibers. The nanofibers were directly spun on the carbon-coated copper grid (200 mesh) and then dried before imaging in TEM.

Fourier transform infrared (FTIR) spectroscopy (FTIR-4200, JASCO, Japan) was used to investigate the polymorphism of PVDF and the interaction between polymer and fillers. The measurement was carried out in the range of  $4000\text{ cm}^{-1} - 650\text{ cm}^{-1}$  at a resolution of  $4\text{ cm}^{-1}$  with 32 scans in the ATR mode. Using Eqn. 1, the %  $\beta$ -phase in PVDF and its TBAC doped nanofibers were determined with an assumption that the absorption follows Lambert-Beer law:

$$F(\beta) = \frac{A_{\beta}}{\left(\frac{K_{\beta}}{K_{\alpha}}\right)A_{\alpha} + A_{\beta}} \quad (2.1)$$

$A_{\alpha}$  is the absorbance at  $763\text{ cm}^{-1}$  ( $\alpha$ -phase), and  $A_{\beta}$  is the absorbance at  $839\text{ cm}^{-1}$  ( $\beta$ -phase). The absorption coefficients for each phase are  $K_{\alpha}$  ( $6.1 \times 10^4\text{ cm}^2/\text{mol}$ ) and  $K_{\beta}$  ( $7.7 \times 10^4\text{ cm}^2/\text{mol}$ ) at  $763\text{ cm}^{-1}$  and  $839\text{ cm}^{-1}$ , respectively.

The following equation was used for the calculation of the  $F(EA)$  in EPVDF and composite nanofabrics (Cai et al. 2017):

$$F(EA) = \frac{A_{840}}{\left(\frac{K_{840}}{K_{762}}\right)A_{762} + A_{840}} \times 100\% \quad (2.2)$$

where  $A_{840}$  and  $A_{762}$  are the absorbances at  $840\text{ cm}^{-1}$  and  $762\text{ cm}^{-1}$ , respectively. The  $K_{840}$  and  $K_{762}$  are the absorbance coefficients at  $840\text{ cm}^{-1}$  and  $762\text{ cm}^{-1}$ , respectively, with values of  $7.7 \times 10^4\text{ cm}^2\text{ mol}^{-1}$  and  $6.1 \times 10^4\text{ cm}^2\text{ mol}^{-1}$ .

The intensities at  $1275\text{ cm}^{-1}$  and  $1232\text{ cm}^{-1}$  were used for the quantitative measurement, as the absorbance intensities of these peaks are related to the amount of the  $\beta$  and  $\gamma$ -phases present, respectively (Cai et al. 2017):

$$F(\beta) = F(EA) \times \left( \frac{\Delta H_{\beta}}{\Delta H_{\beta} + \Delta H_{\gamma}} \right) \times 100\% \quad (2.3)$$

$$F(\gamma) = F(EA) \times \left( \frac{\Delta H_{\gamma}}{\Delta H_{\beta} + \Delta H_{\gamma}} \right) \times 100\% \quad (2.4)$$

where  $\Delta H_{\beta}$  is the height difference (absorbance intensity) between the peak at  $1275\text{ cm}^{-1}$  and its nearest valley at  $1260\text{ cm}^{-1}$ , and  $\Delta H_{\gamma}$  is the height difference between the peak at  $1232\text{ cm}^{-1}$  and the valley at  $1225\text{ cm}^{-1}$  (Cai et al. 2017).

Wide angle X-ray diffraction (WAXD) (Empyrean-Malvern PANalytical, UK) ( $\text{Cu K}\alpha=0.154\text{ nm}$ ,  $45\text{ kV}$ ,  $40\text{ mA}$ ) was employed to study the polymorphic phases. The samples were scanned in a  $2\theta$  range of  $10\text{-}45^\circ$  at a step size of  $0.013^\circ$ , and the time per step was  $24\text{ s}$ .

The total crystallinity using WAXD ( $\chi_{c(WAXD)}\%$ ) was calculated by the following equation:

$$\chi_{c(WAXD)}\% = \frac{A_c}{A_c + A_a} \times 100 \quad (2.5)$$

where  $A_c$  and  $A_a$  are the integrated areas of the XRD peaks corresponding to the crystalline and amorphous phases, respectively.

Differential scanning calorimetry (DSC) (Mettler Toledo, Model-833 E, Switzerland) was used to study the melting temperature and crystallinity of pristine PVDF and doped nanofabrics. The temperature ramp was done at a rate of  $10^\circ\text{C}/\text{min}$  in

dry nitrogen atmosphere purged at a rate of 50 mL/min. The degree of crystallinity using the DSC curve ( $\chi_{c(DSC)}\%$ ) was calculated by the following equation:

$$\chi_{c(DSC)}\% = \frac{\Delta H_S}{\Delta H_{100\%}} \times 100 \quad (2.6)$$

$\chi_{c(DSC)}\%$  is the percentage crystallinity using DSC;  $H_S$  is the enthalpy of fusion of pristine PVDF, and doped nanofabrics;  $\Delta H_{100\%}$  (104.7 J/g) is the enthalpy of pure PVDF of 100% crystallinity (Liu et al. 2013).

The dielectric properties of the nanofabrics were examined using a LCR meter (RS PRO: LCR-6300, UK). The samples were kept between copper electrodes for the measurement, and the test was carried out in the frequency range of 1 kHz-200 kHz at a bias voltage of 1 V. The following equation was used for calculating dielectric constant:

$$\varepsilon_r = \frac{Cd}{\varepsilon_0 A} \quad (2.7)$$

where  $\varepsilon_r$  and  $\varepsilon_0$  are the dielectric constant composite nanofabrics and dielectric permittivity of air ( $8.854 \times 10^{-12}$  F/m),  $C$  and  $d$  are the capacitance and thickness of nanofabrics, respectively, and  $A$  is the surface area of the electrode.

The piezo capacitive sensing of the composite nanofabrics was also examined under the application of an external load using a dielectric analyzer (Alpha A, Novocontrol Technologies, Germany). The sensitivity ( $S$ ) was obtained using the following equation:

$$S = \frac{\Delta C/C_0}{\Delta L} \quad (2.8)$$

where  $\Delta C$  is the relative change in capacitance under external load ( $C-C_0$ ),  $C_0$  is the initial capacitance, and  $\Delta L$  is the applied load. The slope of the response curve was used to determine the sensitivity of the device.

Particle size and Zeta potential analyzer (Litesizer™ 500, Anton-Paar, Austria) was used to measure the  $\zeta$ - potential of BWN and MNS. A particular amount of filler

was dispersed in water so that at least 70% transmittance was maintained to carry out the measurements.

The finger-tapping force was measured using a force sensor (Model-9712B5, Kistler, Austria).

### **2.4 SETUPS AND METHODOLOGY EMPLOYED FOR THE PIEZOELECTRIC, PIEZO CAPACITANCE AND TRIBOELECTRIC PERFORMANCE EVALUATION OF ELECTROSPUN PVDF COMPOSITE/DOPED NANOFABRICS**

#### **2.4.1 Piezoelectric and piezo capacitance setup**

The capacitive sensors were fabricated using copper tape adhered to the flexible insulating plastic sheet that served as the electrode and nanofabrics as a dielectric layer. The nanofabric was placed between the electrodes. An electrode edge has been cushioned with a thin layer of thermoplastic polyurethane (TPU). It does not contribute to the piezo capacitive performance of the device (Fig. 2.1 (a)).

The piezoelectric performances of the PVDF-based nanofabrics were evaluated using a digital oscilloscope (RS PRO-1052, UK) and a standard linear motor kit (Cyltronic AG, Switzerland). A copper electrode was attached to a non-conducting plastic film, and the nanofabric was sandwiched between these copper electrodes to fabricate the PENG device (Fig. 2.1(b)). The electrodes were connected to the oscilloscope to measure the voltage output. Then, the nanogenerator was tested under the application of an external load (Fig 2.2).

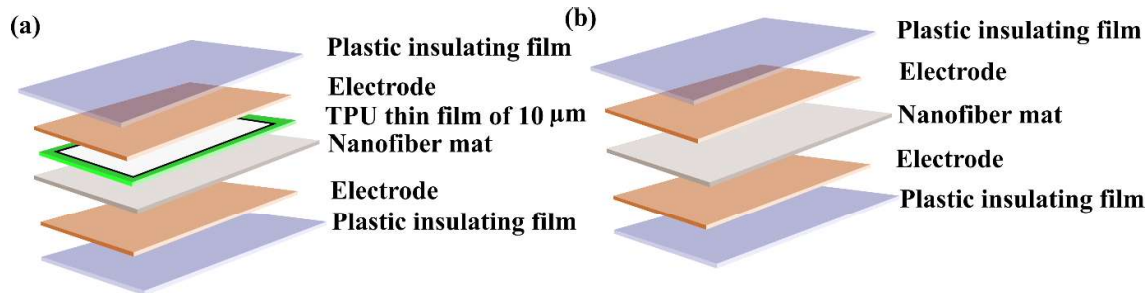


Fig. 2.1 Setup used for the evaluation of (a) Piezo-capacitance based pressure sensor, (b) PENG.

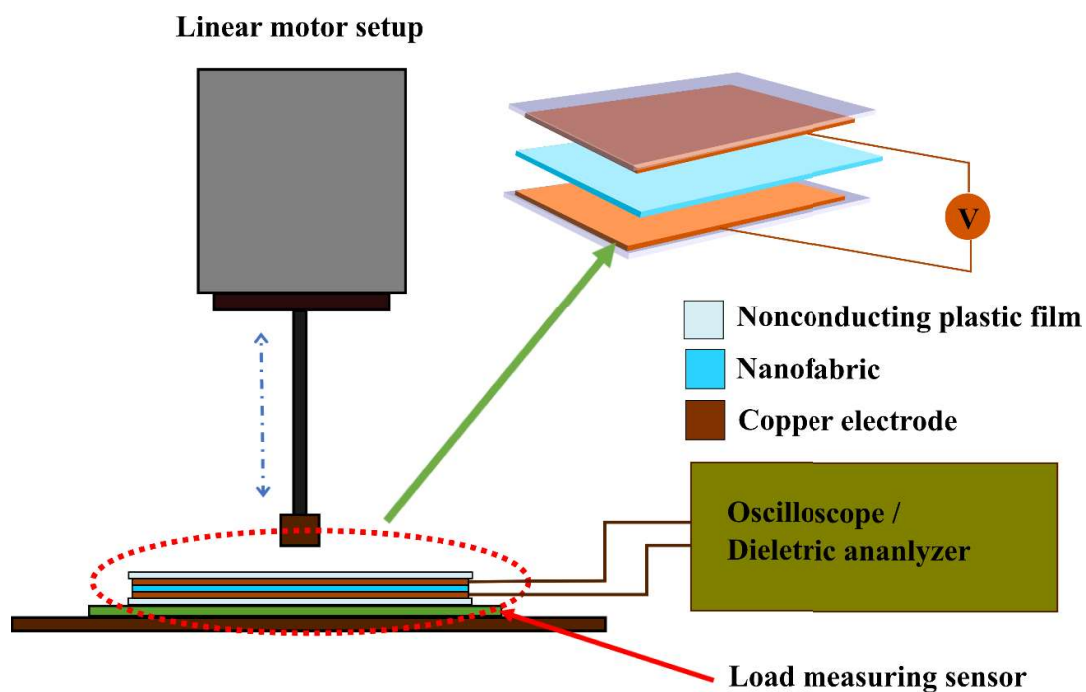


Fig. 2.2 Schematic illustration of the PENG and the piezoelectric and piezo capacitive response measurement setup.

#### 2.4.2 Triboelectric setup

The performance TENG based PVDF-based nanofabrics was studied using a digital oscilloscope (Tektronix, TDS 2012C, USA). The TENG was fabricated using the nanofabric as the tribo-negative material (2 cm  $\times$  2 cm) and a copper strip as the tribo-positive material (2 cm  $\times$  2 cm). The nanofabric was pasted onto a copper electrode, and another copper electrode was attached to the transparent acrylic sheet as shown in Fig

2.3. The top copper electrode, i.e., the tribo-positive material, was glued to the acrylic sheet such that it creates an arc shape above the tribo-negative material. The distance between the tribo-positive and tribo-negative materials was 10 mm.

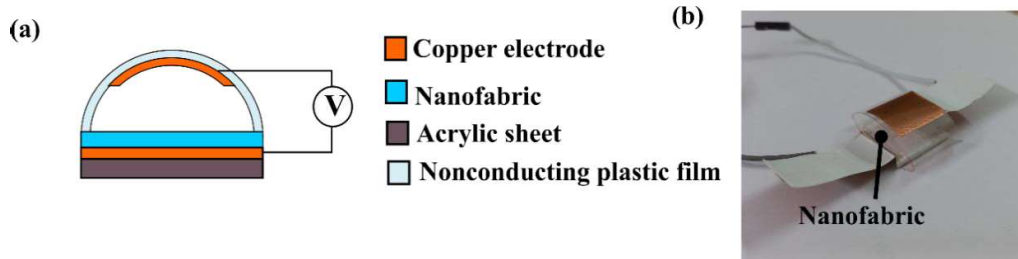


Fig. 2.3 (a) Schematic illustration, and (b) digital photograph of TENG.

The fluttering-driven triboelectric nanogenerator (FDTENG) was fabricated to harvest energy from wind, as illustrated in Fig. 2.4. FDTENG is the small rectangular wind channel of acrylic sheets attached. The length of the wind channel was 9 cm, and its cross-sectional area was  $2.8 \times 2 \text{ cm}^2$ . At the top and bottom of the wind channel, a nanofabric with copper electrodes was attached. The copper foil of a thickness of  $30 \mu\text{m}$  was used as a flag for the FDTENG device, which was attached horizontally at the inlet of the wind channel. The copper flag acts as an electrode as well as a fluttering body in the FDTENG device. An electric fan (Tornado II, Orient electric, India) was used to blow wind at different speeds (measured using Professional Instruments Anemometer, India).

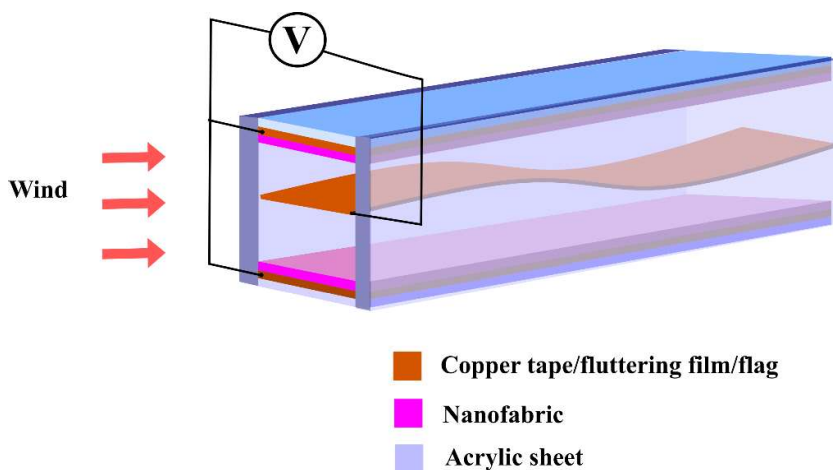


Fig. 2.4 Schematic illustration of the FDTENG.

# CHAPTER 3

---

The results of this chapter have been published in *Soft Matter*, 2021,17, 2215-2222.



## CHAPTER 3

### CATIONIC SURFACTANT ASSISTED ENHANCEMENT OF DIELECTRIC AND PIEZOELECTRIC PROPERTIES OF PVDF NANOFIBERS FOR ENERGY HARVESTING APPLICATION

---

*In this study, PVDF nanofabrics were electrospun from a PVDF solution that contained TBAC. The effect of TBAC on the morphology, crystallinity, and polymorphism of PVDF/TBAC doped nanofabrics was studied using various characterization techniques. The introduction of TBAC led to a significant improvement in the electroactive  $\beta$ -phase of PVDF and its dielectric constant. A piezoelectric nanogenerator was developed using PVDF/TBAC doped nanofabrics to assess the piezoelectric response. The combined effect of electrospinning and TBAC resulted in an enhanced piezoelectric performance of the PVDF doped nanofabrics.*

#### 3.1 RESULTS AND DISCUSSION

##### 3.1.1 Morphology

Fig. 3.1 shows the SEM images of EPVDF and PVDF/TBAC doped nanofibers with different loading of TBAC. The addition of TBAC increases the surface charge density of PVDF solution, which augments the stretching effect during fiber formation through electrospinning. However, the stretching effect also depends on the tangential electrical field (Angamma and Jayaram 2011). AFD decreased with an increase in TBAC loading up to 3 wt%, beyond which it increased slightly. The reduction in the AFD is attributed to the combined effect of high surface charge density and decreased tangential electric field. However, further addition of TBAC above the critical concentration causes a drastic reduction in the tangential electric field, thereby depleting the resultant effect that increases AFD (Angamma and Jayaram 2011). Ico et al. (2016) reported the influence of fiber diameter on piezoelectric performance of PENG. The study revealed that, as fiber diameter decreased, the piezoelectric performance was increased. The relationship between fiber diameter and piezoelectric coefficient is given by equation 3.1.

$$\log d_{33} = 1.96 + 0.19 \log \frac{1}{d} \quad (3.1)$$

where  $d_{33}$  is piezoelectric coefficient, and  $d$  is fiber diameter.

The stretching effect is one of the important parameters, which may influence the electroactive phase formation; it also determines the fiber diameter. In some studies, it was observed that when the fiber diameter decreased electroactive phase increased and vice versa (Khalifa et al. 2016; Khalifa and Anandhan 2019; Shetty et al. 2019). The same trend was observed in our study. Thus, the enhanced electroactive phase can be related to the fiber diameter.

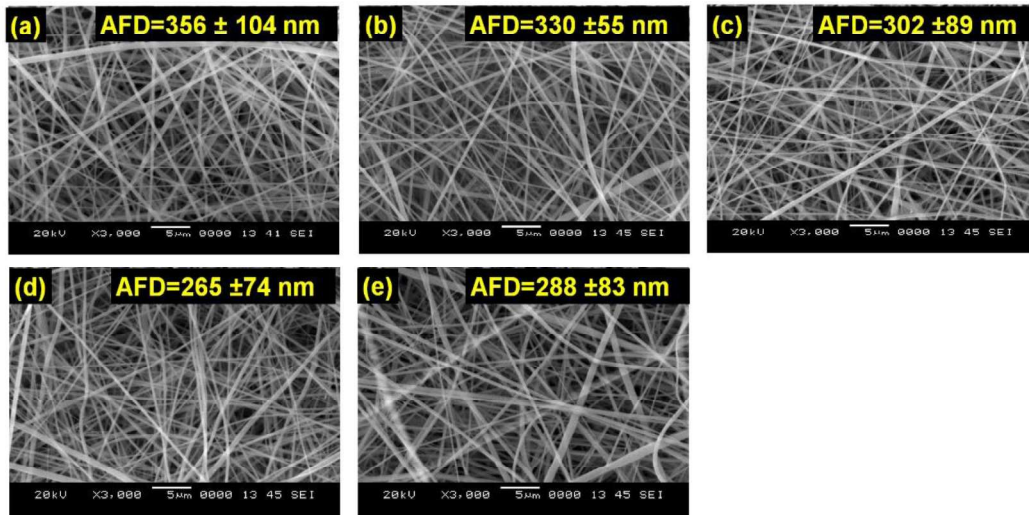


Fig. 3.1 SEM images of (a) EPVDF; and PVDF/TBAC doped nanofibers: (b) PVDF/TBAC-1.0, (c) PVDF/TBAC-2.0, (d) PVDF/TBAC-3.0, (e) PVDF/TBAC-5.0.

### 3.1.2 FTIR spectral analysis

Fig. 3.2(a) shows the FTIR spectra of EPVDF and PVDF/TBAC doped nanofabrics. In the spectrum of EPVDF, peaks at  $763$  and  $975$   $\text{cm}^{-1}$  are the signature peaks of the  $\alpha$ -phase. On the other hand, the peaks at  $839$ ,  $1275$ , and  $1401$   $\text{cm}^{-1}$  are attributed to the  $\beta$ -phase of PVDF (Cai et al. 2017; Khalifa et al. 2016). The peaks at  $975$  and  $763$   $\text{cm}^{-1}$  weakened upon the addition of TBAC, while the peak intensity at  $839$   $\text{cm}^{-1}$  increased. The peak at  $876$   $\text{cm}^{-1}$  ( $\text{CF}_2$ ) shifted to  $878$   $\text{cm}^{-1}$  after the addition of TBAC to PVDF (Fig. 3.2(b)), suggesting strong interaction between the fluorine atoms of PVDF and

the cations of TBAC. The strong ion-dipole interaction between  $\text{CF}_2$  groups of PVDF and the cation of TBAC molecule induces crystallization of PVDF, specifically in the all-trans conformation (Liang et al. 2014a; b). The hydrogen bonding or dipolar interaction between PVDF and DMF also helps to induce  $\beta$ -phase to some extent (He and Yao 2006; Khalifa and Anandhan 2019; Ma et al. 2008). Fig. 3.3 depicts the schematic of ion-dipole interaction between  $\text{CF}_2$  groups of PVDF and the cation of the TBAC molecule; hydrogen bonding or dipolar interaction between  $\text{CH}_2$  of PVDF chain and carbonyl oxygen ( $\text{C}=\text{O}$ ) of DMF is also shown. The  $\beta$ -phase content in PVDF/TBAC doped nanofabrics was calculated using equation (2.1).

The synergistic effect of electrospinning and strong interaction between TBAC and PVDF resulted in the formation of the  $\beta$ -phase in PVDF. As discussed in section 3.1.1, the stretching effect also facilitates the formation of the  $\beta$ -phase of PVDF. The doped nanofabric containing 3 wt% of TBAC showed the highest  $\beta$ -phase content of 89 % in PVDF. Also, this system had the lowest AFD, which is expected to exhibit the best piezoelectric behavior according to equation (3.1). At 5wt% TBAC loading, the  $\beta$ -phase weakened, which may be possibly the result of a decreased stretching effect on the fiber jets during electrospinning, as mentioned in the previous section.

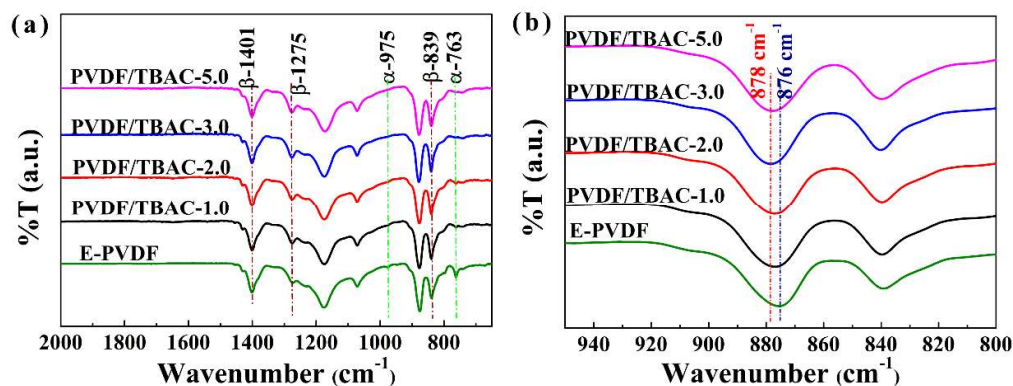


Fig. 3.2 FTIR spectra (a) EPVDF and PVDF/TBAC doped nanofabrics, (b) Shift in the C-F band of PVDF upon the addition of TBAC.

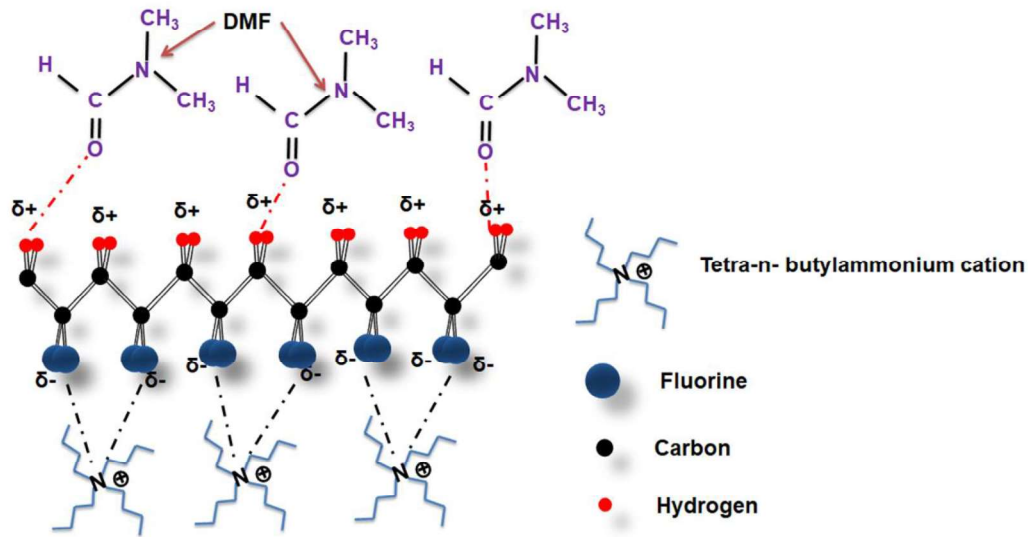


Fig. 3.3 Plausible mechanism of interaction between PVDF, DMF and TBAC.

### 3.1.3 Phase and crystallinity analysis using WAXD and DSC results

Fig. 3.4 shows the WAXD patterns of EPVDF and PVDF/TBAC doped nanofabrics. For EPVDF, peaks at  $20.6^\circ$  and  $36.3^\circ$  correspond to (1 1 0/2 0 0) and (0 2 0) planes of the  $\beta$ -phase. The shoulder peak at  $18.3^\circ$  indicates the presence of the  $\alpha$ -phase of PVDF that corresponds to its (0 2 0) crystal plane (Cai et al. 2017; Shetty et al. 2019). The peak corresponding to the  $\alpha$ -phase ( $18.3^\circ$ ) got weakened upon the addition of TBAC, which is attributed to an increase in the  $\beta$ -phase content. The WAXD results are in line with the FTIR spectral results.

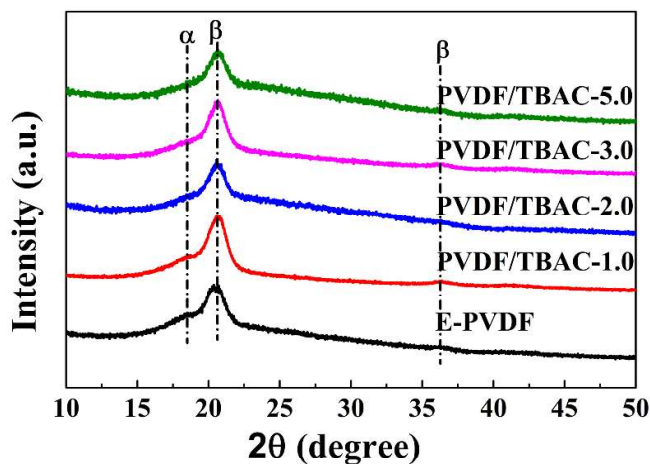


Fig. 3.4 WAXD patterns of EPVDF and PVDF/TBAC doped nanofabrics.

DSC is the most commonly used method for determination of crystallinity in polymers. DSC-based crystallinity measurement is more accurate, as the measurement is based on the enthalpy of melting in which the heat associated with the melting of every crystal can be recorded (Bairagi and Ali 2020; Govinna et al. 2019). DSC curves of EPVDF and PVDF/TBAC doped nanofabrics are shown in Fig. 3.5 and the values of melting temperature, enthalpy, and crystallinity have been highlighted in Table 3.1. The melting temperature of PVDF/TBAC doped nanofabrics was increased by 4°C with respect to that of EPVDF. The higher melting temperature of PVDF/TBAC doped nanofabrics is due to the recrystallization of PVDF chains from the  $\alpha$ -phase to the  $\beta$ -phase (Andrew and Clarke 2008; Liang et al. 2014a; Pramoda et al. 2005; Xue et al. 2017). Also, the formation of the  $\beta$ -phase was confirmed from FTIR spectral and WAXD analyses. The total crystallinity of PVDF/TBAC decreased as the loading of TBAC was increased up to a loading of 3 wt%. The reduction in total crystallinity was found ~8% at 3 wt% loading. Moreover, this system had the lowest average fiber diameter as discussed before. This trend may be attributed to the high evaporation rate of solvent. The high evaporation rate inhibits crystal rearrangement, which produced slightly less ordered crystalline structure. The rate of evaporation of solvent from an electrospinning jet depends on the extent of stretching; as stretching effect increases, the solvent evaporation rate also increases and vice-versa. Thus, the stretching effect

influences the evaporation rate of solvent, which in turn alters the crystallinity of the fibers (Itoh et al. 2016).

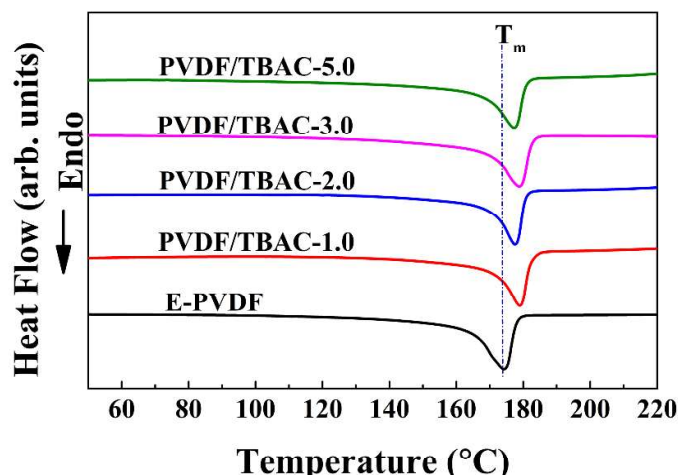


Fig. 3.5 DSC curves (second heating cycle) of EPVDF and PVDF/TBAC doped nanofabrics.

Table 3.1 Melting temperature ( $T_m$ ), enthalpy of melting ( $\Delta H_s$ ), crystallinity  $\chi_{c(DSC)}$ (%) and  $F(\beta)$ (%) of EPVDF and PVDF/TBAC doped nanofabrics.

| Sample        | $\Delta H_s$ (J/g) | $T_m$ (°C) | $\chi_{c(DSC)}$ (%) | $F(\beta)$ (%) |
|---------------|--------------------|------------|---------------------|----------------|
| EPVDF         | 48.6               | 174.2      | 46.4                | 57             |
| PVDF/TBAC-1.0 | 46.7               | 178.9      | 44.6                | 83             |
| PVDF/TBAC-2.0 | 46.1               | 177.5      | 44.0                | 85             |
| PVDF/TBAC-3.0 | 44.9               | 178.6      | 42.8                | 89             |
| PVDF/TBAC-5.0 | 47.3               | 177.4      | 45.1                | 86             |

### 3.1.4 Piezoelectric Performance

The performances of EPVDF and PVDF/TBAC doped nanofabrics based piezoelectric nanogenerator (PENG) were evaluated under the constant force of 2.5 N (Fig. 3.6(a)). The  $V_{OC}$  of 10.2 V was observed for PVDF/TBAC-3.0. Its enhanced piezoelectric response may be attributed to the presence of high  $\beta$ -phase content. On the other hand,  $V_{OC}$  of 0.9, 2.2, 4.5 and 4.6 V were generated from EPVDF, PVDF/TBAC-1.0,

PVDF/TBAC-2.0, and PVDF/TBAC-5.0, respectively. Since PVDF/TBAC-3.0 showed the highest voltage output, it was tested under different values of the applied force (0.5, 1, 2, 3, and 5 N), and results are shown in Fig. 3.6(b). With an increase in the applied force, the voltage output increased significantly, and it reached up to 17.2 V at 5 N, which is higher than the piezoelectric response previously reported by Zaarour et al. (2020) i.e., ~2.6 V (Table I.1). The voltage output generated by PVDF/TBAC-3.0 was 19.1 times higher than that of EPVDF. Piezoelectric output of PVDF depends on the presence of the electroactive phase in it. However, the fineness of fibers (Abbasipour et al. 2017), relative humidity (RH) (Szewczyk et al. 2020), additives (morphology and surface nature of additives) (Abbasipour et al. 2017; Mokhtari et al. 2017; Sharma et al. 2016) can also influence the piezoresponse. Abbasipour et al. (2017) reported that the piezoelectric response cannot be assessed only through the electroactive phase; the fineness and orientation of the nanofibers also play an important role. Szewczyk et al. (2020) reported that, along with the electroactive phase, RH, and voltage polarity in the electrospinning process are also vital for the enhancement of piezoresponse of PVDF nanofabric. Their study ascribed the higher relative humidity to the higher piezoresponse of their PVDF nanofabrics. Zaarour et al. (2020) prepared PVDF nanofabrics with relatively higher loading of the surfactant i.e. 0.2 mol/L (0.5558 g/10 mL) at a relative humidity (RH) of 10%. In our study, the RH was kept at  $55 \pm 2$  %, and the surfactant loading was lower (0.0135 g/10 mL to 0.0675 g/10 mL) than that of their study. In our study, we believe that the synergistic effect of the electrospinning parameter (such as RH), fiber morphology, and optimized loading of TBAC has improved the piezoelectric response of PVDF nanofabric. The output voltage showed signals in the positive and negative directions. The positive signal is attributed to the aligned dipoles in the direction of the applied force. The dipoles are aligned due to the resultant potential difference when a compressive force is applied. The negative signal is attributed to the release of the applied force, producing a reverse output voltage when the material returns back to its initial position. The comparison of piezoelectric performance of PVDF/TBAC doped nanofiber-based PENG with reported PVDF/ionic liquid or alkyl ammonium salts in the literature is given in Table I.1. The results are comparable with published literature.

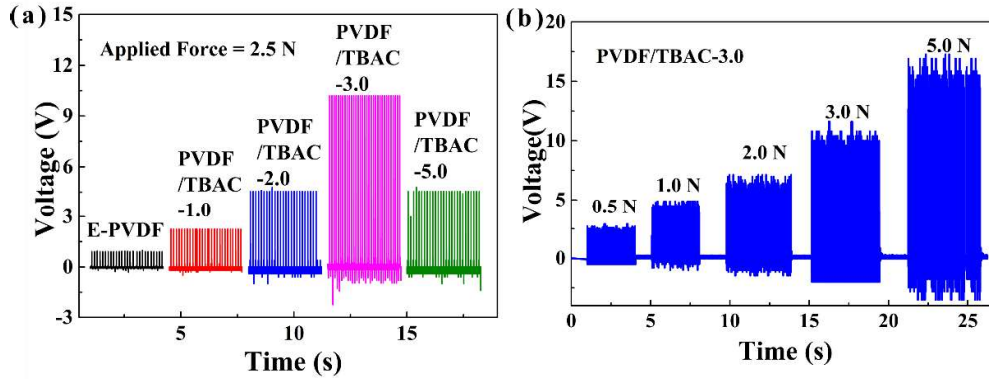


Fig. 3.6 (a) Piezoelectric response of EPVDF and PVDF/TBAC doped nanofabrics at different loading of TBAC (under a constant applied force of 2.5 N), (b) Piezoelectric response of PVDF/TBAC-3.0 under different values of applied force.

Fig. 3.7 shows the change in voltage and current outputs as a function of load resistance (1-10 M $\Omega$ ) upon application on 3 N force on the PENG-based on PVDF/TBAC-3. The voltage generated by the PENG increased with respect to the load resistance, and a reverse trend was observed in the case of current. The power density (P) was calculated using the following equation:

$$P = \frac{V^2}{A \times R_l} \quad (3.2)$$

where V is the output voltage, A is an effective area and  $R_l$  is the load resistance across the circuit. The maximum power density of  $\sim 1.4 \mu\text{W}/\text{cm}^2$  was observed at a load resistance of 8 M $\Omega$ .

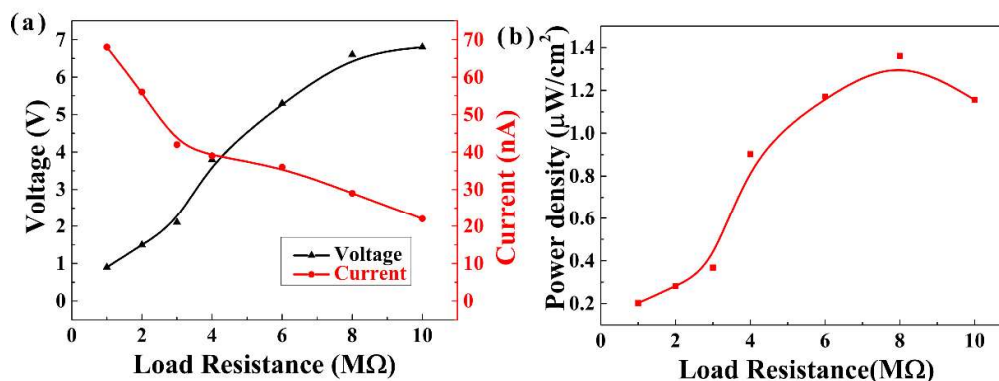


Fig. 3.7 (a) The output voltage and current across different load resistances, (b) calculated power density of PVDF/TBAC-3.0 based PENG under 3 N load at different load resistance values.

### 3.1.5 Dielectric studies

The frequency-dependent dielectric properties of EPVDF and PVDF/TBAC doped nanofabrics are shown in Fig. 3.8. The dielectric constant of the doped nanofabrics increased as a function of TBAC loading. At 1000 Hz, the dielectric constant of PVDF/TBAC-3.0 was 22.5, which is 210% higher than that of EPVDF. For all the loadings of TBAC, doped nanofabrics showed a dielectric constant higher than that of EPVDF. This enhancement in dielectric constant may be ascribed to the following reasons: First, an improved stretching effect during electrospinning, attributed to the addition of TBAC. Stretching causes polymer chains to align and form the  $\beta$ -phase, which might lead to the enhancement of dielectric constant (Ye et al. 2013). Second is the Maxwell–Wagner–Sillars interfacial polarization (MWS) effect. The differences in conductivity and permittivity of PVDF and TBAC causes space charges to accumulate at the interface, which results in the MWS effect (Fan et al. 2019; Shetty et al. 2019). Also, the porous structure in the nanofabrics varies the dipole density, thus affecting the dielectric constant (Yang et al. 2014). The dielectric loss was suppressed upon the addition of TBAC. These results indicate that the PVDF/TBAC nanofabrics developed in this study have the potential to be used in flexible electronics.

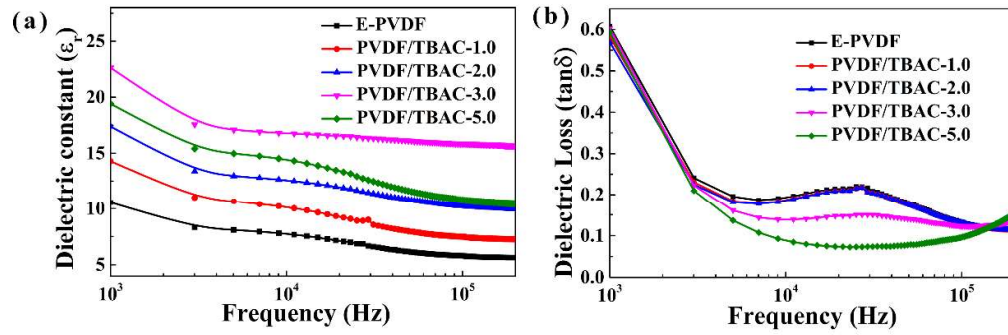


Fig. 3.8 Frequency-dependent; (a) dielectric constant, (b) dielectric loss of EPVDF and PVDF/TBAC doped nanofabrics.

# CHAPTER 4

---

The results of this chapter have been published in *Flexible and Printed Electronics*, 2023, 8 025011.



## CHAPTER 4

### DEVELOPMENT OF A FLEXIBLE PIEZOELECTRIC AND TRIBOELECTRIC ENERGY HARVESTER WITH PIEZO CAPACITIVE SENSING ABILITY FROM BARIUM TUNGSTATE NANOROD-DISPERSED PVDF NANOFABRICS

---

*Herein, We have investigated in detail the effect of the addition of reverse microemulsion synthesized BWN on morphology, crystallinity, and polymorphism of electrospun PVDF nanofabrics. The electroactive phase content ( $\beta$  and  $\gamma$ -phases) of the nanofabrics was enhanced upon the addition of BWN, which may be attributed to the synergistic effect of filler-polymer interaction and electrospinning. The dielectric constant of the nanofabrics containing BWN was enhanced compared to EPVDF. Additionally, piezo capacitive sensing ability was improved upon the introduction of BWN. The piezoelectric and triboelectric nanogenerators were fabricated using PVDF/BWN composite nanofabrics. The nanogenerators fabricated using PVDF/BWN composite nanofabrics exhibited enhanced performance than that of EPVDF based nanogenerators.*

#### 4.1 RESULTS AND DISCUSSION

##### 4.1.1 Characterization of BWN

Fig. 4.1(a) shows the X-ray diffractogram of the synthesized BWN. The diffraction peaks located at  $17.26^\circ$ ,  $26.47^\circ$ ,  $28.0^\circ$ ,  $31.9^\circ$ ,  $43.0^\circ$ ,  $45.7^\circ$ ,  $48.64^\circ$ ,  $53.6^\circ$ , and  $54.5^\circ$  represent the (1 0 1), (1 1 2), (0 0 4), (2 0 0), (2 0 4), (2 2 0), (1 1 6), (3 1 2) and (2 2 4) crystal planes of  $\text{BaWO}_4$  respectively. This result matches with the ICDD pattern no. 00-043-0646, confirming the successful obtention of tetragonal  $\text{BaWO}_4$ . In the FTIR spectrum of BWN (Fig. 4.1(b)), the intense band at  $801\text{ cm}^{-1}$  corresponds to the asymmetric stretching vibration of W–O and a small hump at a lower wavenumber could be due to the weak bending vibration of W–O (Khan et al. 2018; Sadiq and Nesaraj 2015). The  $\zeta$ -potential curve of BWN in Fig. 4.1(c) confirms that the particles are negatively charged with a mean  $\zeta$ -potential value of  $-38.8\text{ mV}$ . SEM image (Fig. 4.1(d)) reveals that  $\text{BaWO}_4$  has crystallized in the shape of rods. The average diameter

and length of these rods were  $252 \pm 47$  nm and  $1421 \pm 370$  nm, respectively (the measurements were done on 50 nanorods using the image-J tool).

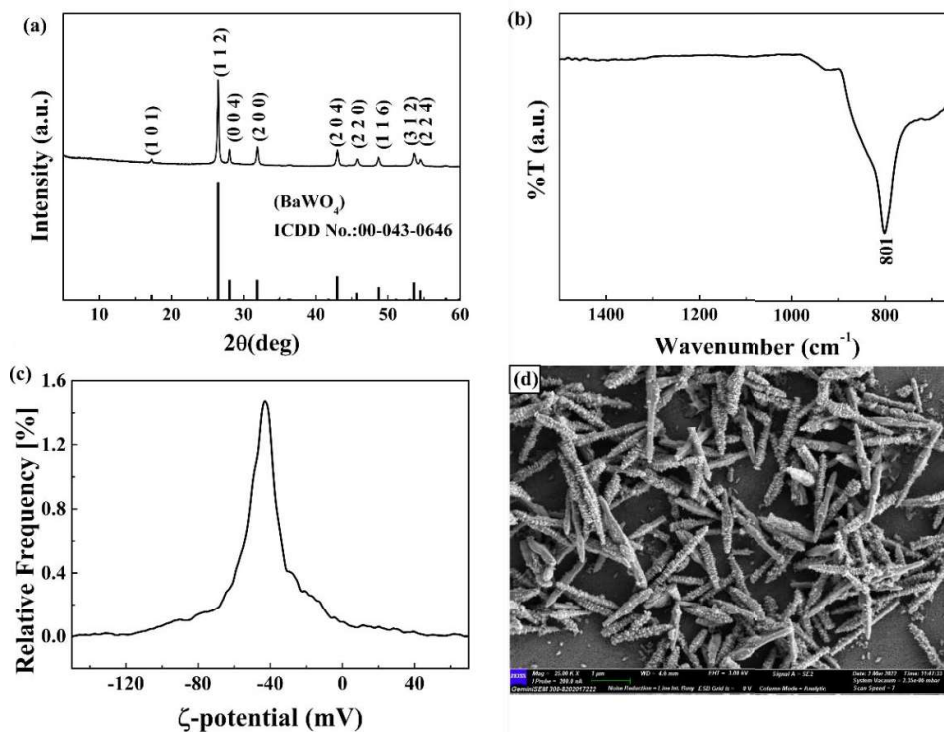


Fig. 4.1 (a) WAXD, (b) FTIR spectrum, (c)  $\zeta$ -potential curve, and (d) FESEM image of BWN.

## 4.1.2 Characterization of PVDF/BWN composite nanofabrics

### 4.1.2.1 Morphology

The AFD of composite nanofabrics increased upon increasing the loading of BWN (Fig. 4.2), which could be attributed to the increased viscosity of the polymer solution upon the addition of BWN (Hosseini and Yousefi 2017; Tiwari et al. 2019). The diameter of fiber signifies the amount of stretching that occurred during the electrospinning, and this stretching could induce the formation of the electroactive phase in PVDF, as discussed in our previous reports (Ekbote et al. 2021; Shetty et al. 2020). However, apart from the stretching effect, the interaction between the nanofiller particles and PVDF chains also has a significant role in inducing the electroactive phase. Herein, the

interaction between the PVDF chains and the surface of BWN could be the dominating factor over the stretching effect, leading to enhancement in the electroactive phase content.

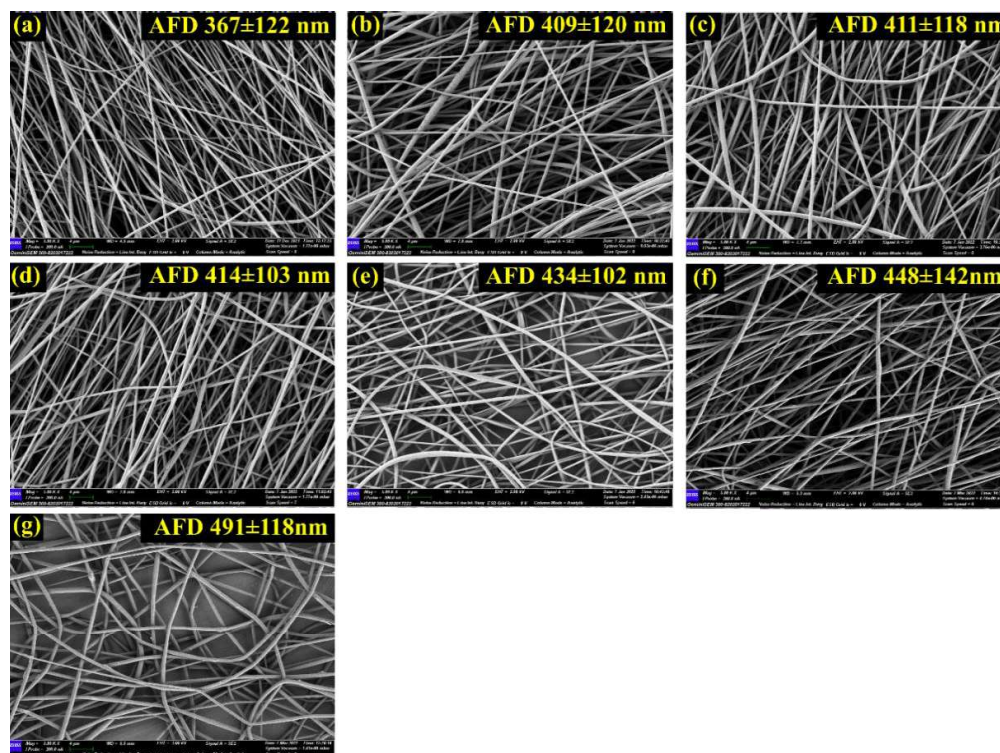


Fig. 4.2 FESEM images of (a) EPVDF, (b) PVDF/BWN-0.5, (c) PVDF/BWN-1, (d) PVDF/BWN-1.5, (e) PVDF/BWN-2, (f) PVDF/BWN-3, (g) PVDF/BWN-5 (the AFD and SD values are indicated as inset within each image).

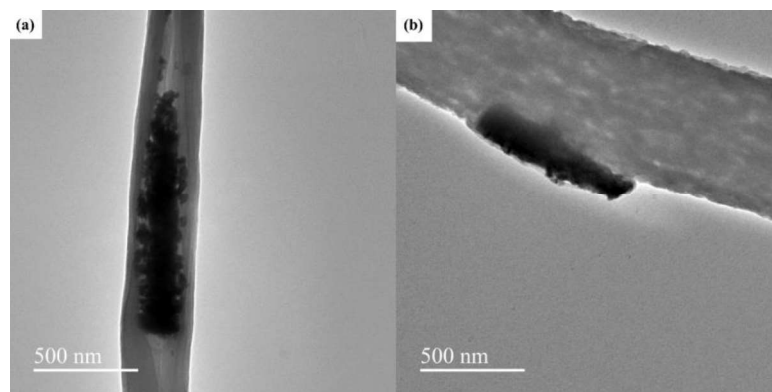


Fig. 4.3 TEM images of a single nanofiber of PVDF/BWN-3 imaged at two locations.

Fig. 4.3 shows the representative TEM images of PVDF/BWN-3 nanofiber imaged at two locations. The BWN were finely dispersed and encapsulated by the PVDF (Fig. 4.3(a)). Also, the particles were aligned along the fiber axis due to the stretching of the fiber jets during electrospinning. Some nanorods are also observed on the surface of the nanofiber, as shown in Fig. 4.3(b).

#### 4.1.2.2 FTIR spectral analysis

FTIR spectroscopy was carried out to study the polymorphism in the EPVDF and PVDF/BWN composite nanofabrics (Fig. 4.4). The peaks at 762, 796, and 975  $\text{cm}^{-1}$  are the signatures of the  $\alpha$ -phase. The peaks 840 and 1275  $\text{cm}^{-1}$  represent the  $\beta$ -phase. The characteristic peak of the  $\gamma$ -phase didn't appear at 1232  $\text{cm}^{-1}$  in EPVDF (Cai et al. 2017; Martins et al. 2014). The FTIR spectra of PVDF/BWN composite nanofabrics reveal that the intensities of the peaks representing the  $\alpha$ -phase, i.e., those at 763, 795, and 975  $\text{cm}^{-1}$ , were diminished upon the addition of BWN. Also, the intensity of the polar phase peak at 840  $\text{cm}^{-1}$  was improved, and a small shoulder peak of the  $\gamma$ -phase appeared at 1232  $\text{cm}^{-1}$ , which can be seen in the enlarged view of FTIR spectra in Fig. 4.4(b). However, the significant peak at 1275  $\text{cm}^{-1}$  of the  $\beta$ -phase and the absence of peaks at 776, 811, and 833  $\text{cm}^{-1}$  of the  $\gamma$ -phase hint at the predominance of the  $\beta$ -phase in the polar phase content (Cai et al. 2017; Martins et al. 2014; Shetty et al. 2021). The peaks at 3022  $\text{cm}^{-1}$  and 2981  $\text{cm}^{-1}$  correspond to the  $\text{CH}_2$  stretching vibrations of the PVDF. The peaks of  $\text{CH}_2$  were shifted to a lower wavenumber (Fig. 4.4(c)), which may be attributed to the interfacial/electrostatic interaction between the negatively charged surface of the BWN particle (with a  $\zeta$ -potential of -38.8 mV) and  $\text{CH}_2$  group of the PVDF chains (Dutta et al. 2015; Kar et al. 2015; Martins et al. 2012). The  $F(\text{EA})$ ,  $F(\beta)$ , and  $F(\gamma)$  in PVDF/BWN composite nanofabrics were calculated using equations (2.2), (2.3), and (2.4.).

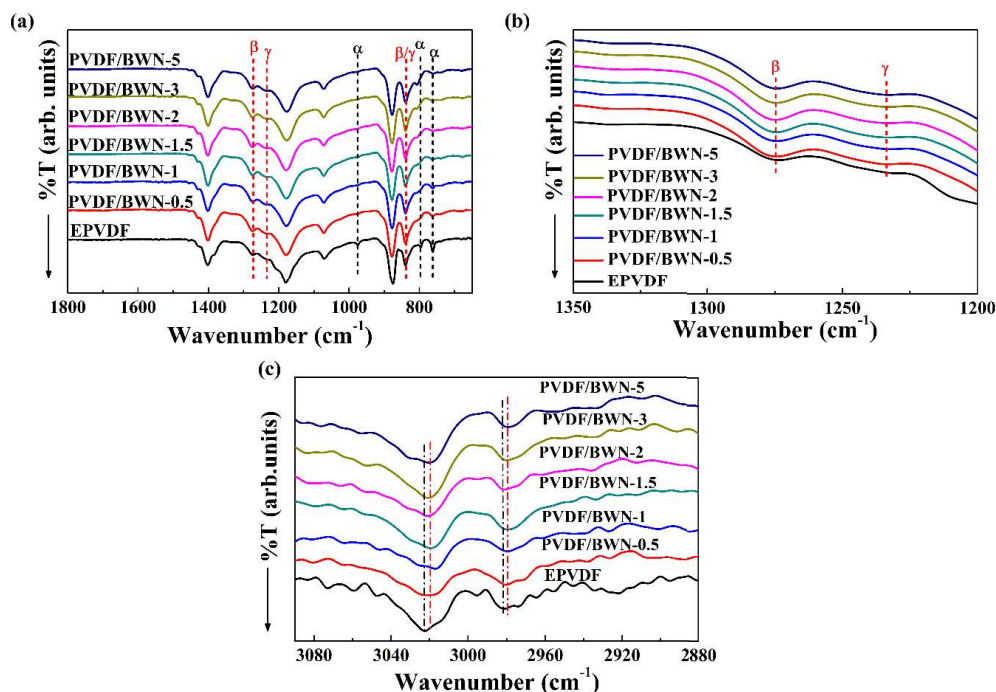


Fig. 4.4 FTIR spectra of EPVDF and PVDF/BWN composite nanofabrics in the wavenumber ranges of (a) 1800-650  $\text{cm}^{-1}$ , (b) 1350-1200  $\text{cm}^{-1}$ , (c) 3100-2880  $\text{cm}^{-1}$ .

The F(EA) was improved with the BWN loading up to 3 wt%; after which the polar phase content was decreased, as detailed in Table 4.1. The decrease in the F(EA) at higher loading of BWN was possibly due to the agglomeration of particles. The highest F(EA) of 86.5% was observed for PVDF/BWN-3. The enhancement in the polar phase could be attributed to the following reasons: first, the C=O group of the polar solvent DMF might have weakly interacted with  $\text{CH}_2$  of PVDF chains, lowering the energy barrier for the formation of the electroactive phase (Ekbote et al. 2021; Khalifa et al. 2021). Second, the interaction between the negatively charged surface of BWN and the positively charged  $\text{CH}_2$  group of PVDF might have compelled to arrange the PVDF chains in the polar conformation (Dutta et al. 2015; Jiang et al. 2020; Kar et al. 2015; Martins et al. 2012; Parangusan et al. 2019). However, the variation in surface charge distribution over the nanoparticles causes repulsion between  $\text{CH}_2$  and positive charge, and attraction between  $\text{CF}_2$  and positive charge of BWN led to the formation of a small fraction of the  $\gamma$ -phase along with its  $\beta$ -counterpart (Fig. 4.5). Similar results were also reported by other researchers (Sarkar et al. 2014). Finally, the electrospinning

process is proven to enhance the electroactive phase by mechanical stretching and local electrical poling of the fiber. The synergism of all these factors could have contributed to enhancement in F(EA).

Table 4.1 F(EA)(%), F( $\beta$ )(%), F( $\gamma$ )(%), and total crystallinity of PVDF/BWN composite nanofabrics.

| Composite    | F(EA)<br>(%) | F( $\beta$ )<br>(%) | F( $\gamma$ )<br>(%) | Total<br>Crystallinity by<br>WAXD<br>$\chi_{c(WAXD)}$ (%) |
|--------------|--------------|---------------------|----------------------|---|
| EPVDF        | 63.6         | 63.6                | 0                    | 36.5  |
| PVDF/BWN-0.5 | 77           | 71.5                | 5.5                  | 41.0  |
| PVDF/BWN-1   | 78.1         | 73.0                | 5.1                  | 42.7  |
| PVDF/BWN-1.5 | 82           | 76.7                | 5.4                  | 44.4  |
| PVDF/BWN-2   | 83.5         | 78.3                | 5.2                  | 45.1  |
| PVDF/BWN-3   | 86.5         | 80                  | 6.5                  | 46.0  |
| PVDF/BWN-5   | 85.7         | 77.3                | 8.4                  | 45.5  |

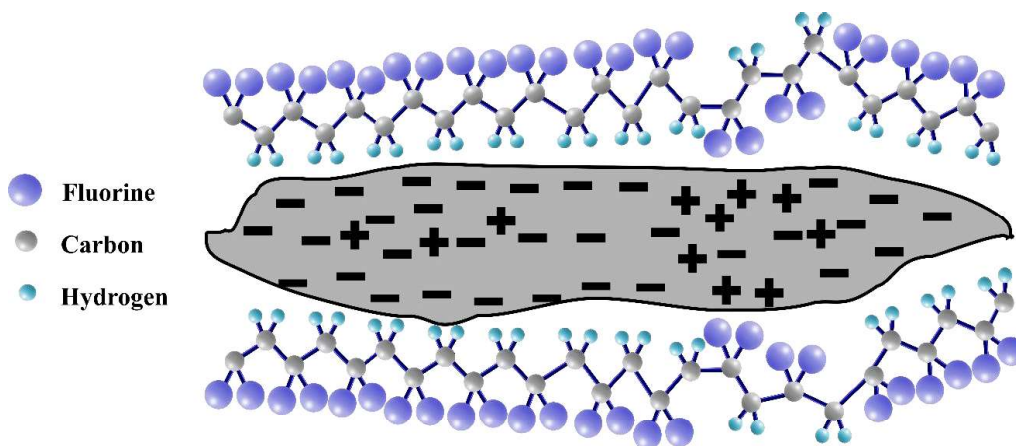


Fig. 4.5 Schematic representation of plausible mechanism of interaction between the surface of BWN and PVDF chains.

## 4.1.2.3 WAXD analysis

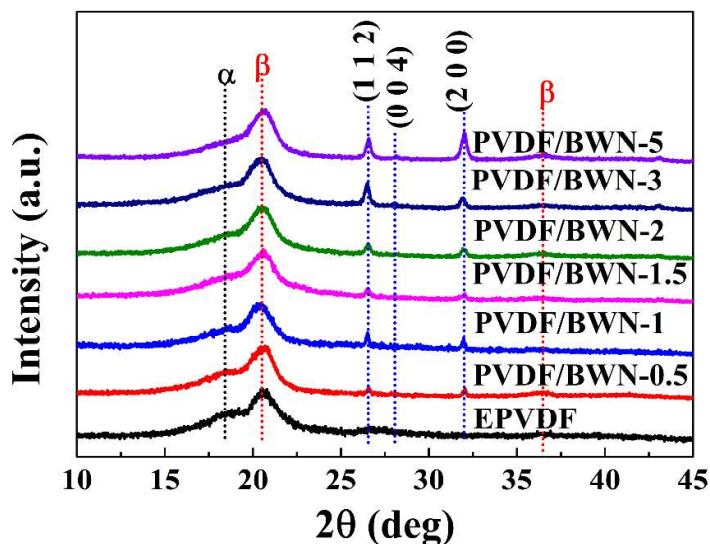


Fig. 4.6 WAXD patterns of EPVDF and PVDF/BWN composite nanofabrics.

WAXD was carried out to study the polymorphism in EPVDF and PVDF/BWN composite nanofabrics, and the diffractograms are shown in Fig. 4.6. The signature peaks of the  $\alpha$ -phase are observed at  $18.3^\circ$  (0 2 0) and  $27^\circ$  (0 2 1), and the signature peaks of the  $\beta$ -phase are observed at  $20.6^\circ$  (1 1 0/ 2 0 0) and  $36.3^\circ$  (2 0 1) (Esterly and Love 2004; Martins et al. 2014). The peaks at  $26.6^\circ$ ,  $28.1^\circ$ , and  $32^\circ$  correspond to BWN. The intensity of the  $\alpha$ -phase peak was reduced while that of the  $\beta$ -phase was enhanced upon the addition of BWN, which may be due to the improved F(EA) in PVDF. The results suggest that the electroactive phase of PVDF was enhanced upon the addition of BWN, which agrees with the FTIR spectral results. In WAXD curves, the peaks of the  $\gamma$ -phase were not observed. The  $\gamma$ -phase peaks overlap with that of the  $\alpha$ -phase at  $18.5^\circ$ ,  $20^\circ$ , and  $26.7^\circ$ , and these overlapped peaks hinder the identification of a small amount of the  $\gamma$ -phase present in the PVDF/BWN composite nanofabrics using only the WAXD data (Ince-Gunduz et al. 2010; Martins et al. 2014). However, the FTIR data confirm the absence of the  $\gamma$ -phase in EPVDF, which concludes that the peak at  $18.5^\circ$  belongs to the  $\alpha$ -phase in EPVDF. So, the FTIR spectral results were taken into account for the phase study along with that of WAXD.

The total crystallinity was calculated by deconvoluting the WAXD curves, as depicted in Fig. 4.7. As the peaks of the  $\gamma$ -phase were absent in WAXD, it was not considered for calculating the total crystallinity. The crystallinity of the composites increased upon the addition of BWN. The higher total crystallinity of composite nanofabrics is due to the nucleating effect of the BWN for the PVDF macromolecules (Bharath et al. 2019; Chandran et al. 2021; Jahan et al. 2017; Tsonos et al. 2019).

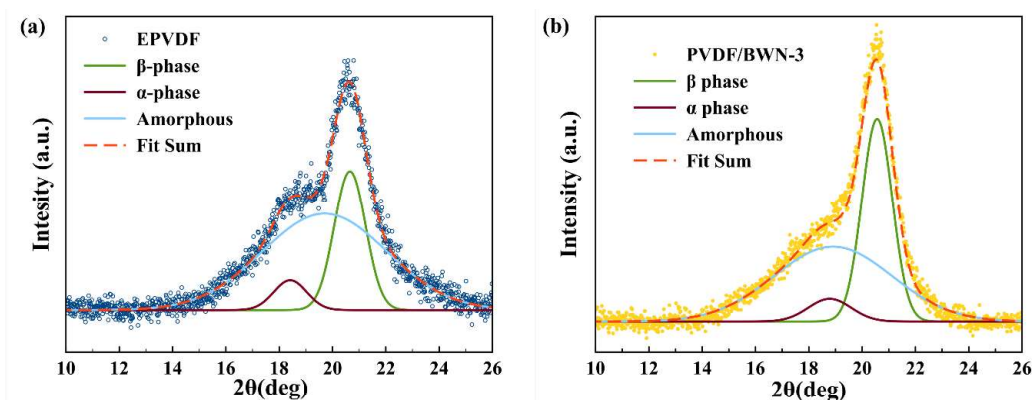


Fig. 4.7 Deconvoluted WAXD patterns of (a) EPVDF and (b) PVDF/BWN-3.

#### 4.1.2.4 Dielectric studies

The dielectric properties of the EPVDF and PVDF/BWN composite nanofabrics were measured with respect to frequency at room temperature (Fig. 4.8). In the composites, the dielectric constant increased slowly with an increase in the filler loading at all frequencies. The resultant improvement in the dielectric constant of composite nanofabrics may be attributed to the enhanced F(EA) (Shetty et al. 2020; Ye et al. 2013), the addition of the filler with a high dielectric constant (Dash et al. 2019; Patil et al. 2021), and the charge accumulation at the interface of PVDF and BWN particles in the low-frequency region (Shamitha et al. 2020). At 1 kHz, the highest dielectric constants of 17.64 and 17.68 were observed for the PVDF/BWN-3 and PVDF/BWN-5, respectively. The dielectric constant decreased as the frequency was increased, which could be due to frequency-dependent dipolar and space charge polarization; when dipoles fail to align themselves to the applied field as frequency increases, the dielectric constant decreases (Lu et al. 2017). The conduction loss and polarization (dipolar, distortion, and interfacial) determine the dielectric loss in polymer composites (Prateek

et al. 2016). The dielectric loss of EPVDF was low compared to that of the composites. The composites have a high dielectric loss, which could be due to the interfacial polarization and conductive loss caused by the formation of smaller domains of the network (Hu et al. 2015). The increase in the loading of the filler leads to an increase in heterogeneity, which leads to an increase in interfacial polarization resulting in the high dielectric constant and dielectric loss at low frequency. In addition to the dielectric properties of the filler and polymer, the morphology, dispersion, and polymer-filler interaction also affect the dielectric properties of the composites (Dash et al. 2019). Also, the dipole density of nanofabrics varies due to their porous structure, affecting the dielectric property (Shetty et al. 2019). The dielectric constant represents the charge storage ability, whereas the dielectric loss represents the leaky nature or inefficacy of the material to maintain the charges. A material with a low dielectric loss can maintain the charges efficiently, and the high dielectric constant can improve triboelectric charge density due to enhanced capacitance of the material. Therefore, the high dielectric constant and low dielectric loss of the composite nanofabrics makes them ideal for good triboelectric performance.

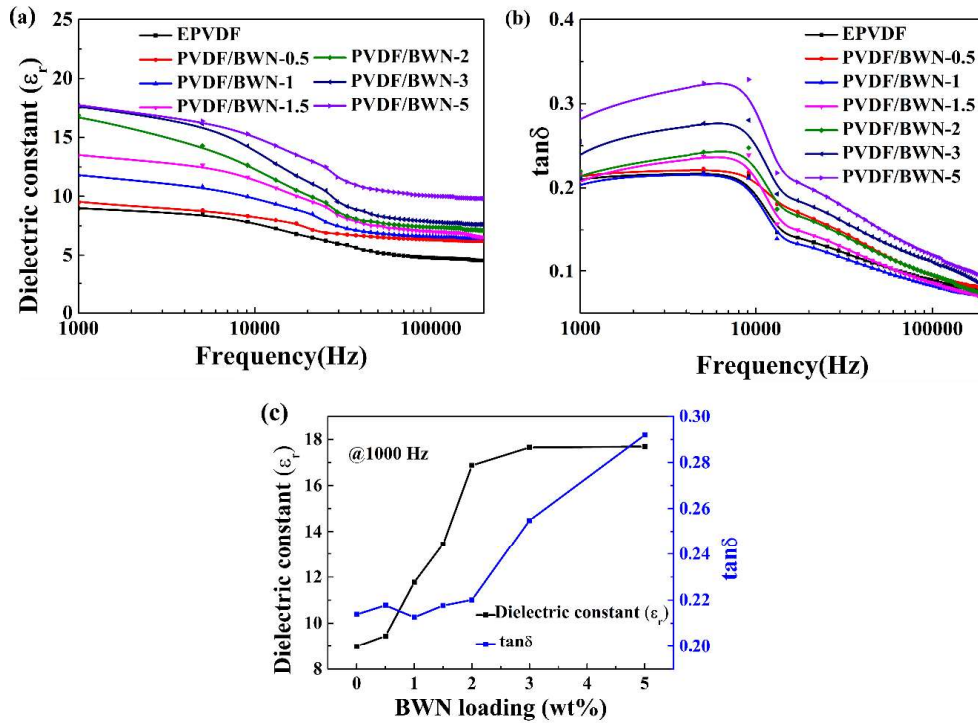


Fig. 4.8 Frequency-dependent (a) dielectric constant and (b) dielectric loss of EPVDF and PVDF/BWN composite nanofabrics, (c) dielectric constant and dielectric loss values at 1000 Hz as a function of the loading of BWN.

#### 4.1.2.5 Piezo capacitance evaluation

The capacitive-based sensor was fabricated using two copper electrodes and PVDF/BWN-5 as the dielectric material (parallel plate configuration), and linear motor setup was used for the application of external force (Fig. 2.1). The PVDF/BWN-5 was used to fabricate the capacitive-based pressure sensor as it has the highest dielectric constant among all the composite nanofabrics. Fig. 4.9 depicts the performance of the capacitive-based sensor of EPVDF and PVDF/BWN-5.

The capacitance of the PVDF/BWN-5 nanofabric-based sensor was higher than that of the EPVDF nanofabric-based one. The enhanced capacitive performance of former may be due to its higher dielectric constant value. The ratio of change in capacitance to the initial capacitance of the composite nanofabric-based sensor increased linearly upon the application of external force, and its value increased by  $\sim 4$

times that of EPVDF based sensor under a load of 8 N. The increase in capacitance of the sensor could be due to the decrease in the distance between the electrode and the improved effective dielectric constant of the PVDF/BWN-5. The increase in dielectric constant could be due to improved packing density of the nanofabric upon application of external load, which gradually eliminated the pores (Kwon et al. 2016; Yang et al. 2019; Zhu et al. 2020). The sensitivity was determined by calculating the slope of the curve representing the capacitive response ( $\Delta C/C_0$ ) as a function of the applied force. The sensitivity of the fabricated device was found to be 0.66/N. The PVDF/BWN-5 based capacitive sensor with good sensitivity could find application in touch sensing, wearable devices, and medical devices (Ma et al. 2018; Wan et al. 2017).

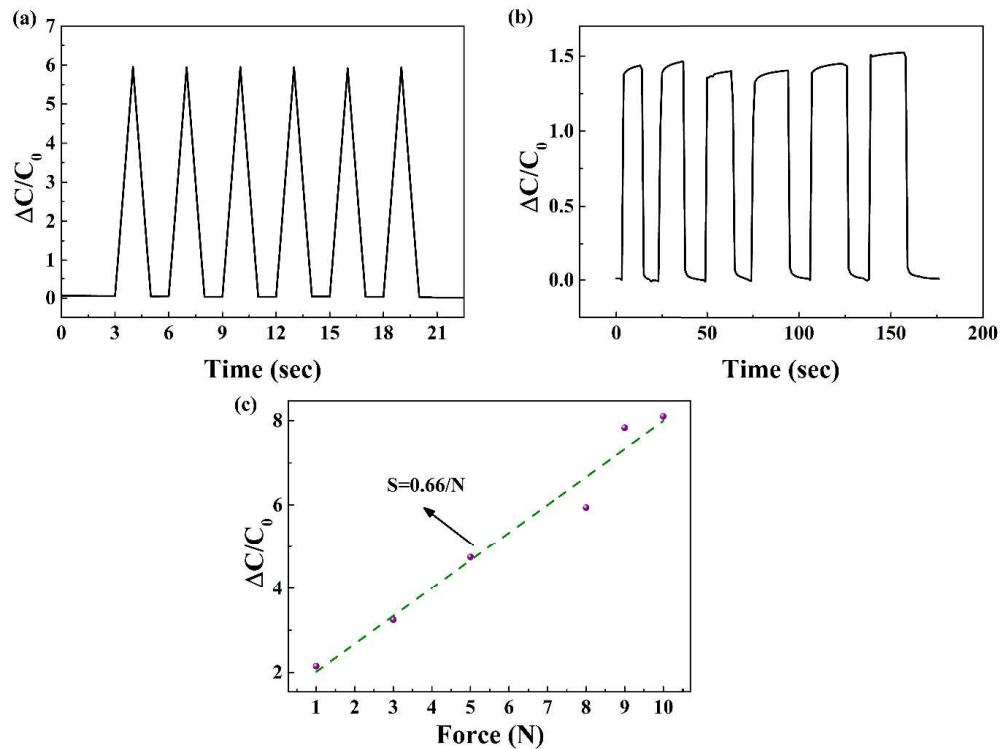


Fig. 4.9 (a) Ratio of relative change in capacitance to the initial capacitance ( $\Delta C/C_0$ ) of the sensor fabricated from PVDF/BWN-5 and (b) ratio of relative change in capacitance to the initial capacitance ( $\Delta C/C_0$ ) of EPVDF at 8 N load, and (c) ratio of relative change in the capacitance to the initial capacitance ( $\Delta C/C_0$ ) of the sensor based on PVDF/BWN-5 with respect to the applied force.

#### 4.1.2.6 Piezoelectric properties

The piezoelectric response of PENG based on EPVDF and PVDF/BWN composite nanofabrics was assessed using a standard linear motor kit (Fig. 2.2). Fig. 4.10 shows the piezoelectric performance of EPVDF and PVDF/BWN composite nanofabrics based PENG. The PENG was tested under an applied force of 8 N (at a frequency of 1.25 Hz), and force was applied normal to the plane of the nanogenerator. The piezoelectric  $V_{OC}$  was increased upon the addition of filler and continued to increase up to 3 wt% loading of the BWN, beyond which it decreased. The highest  $V_{OC}$  recorded was 8 V for the PVDF/BWN-3 based PENG, which was  $\sim 6.4$  times that of the EPVDF based device. The enhanced piezoelectric response may be attributed to the improved  $F(EA)$  in the PVDF (Khalifa et al. 2016; Shetty et al. 2020). The morphology and surface nature of additives and relative humidity may also contribute to the enhanced piezoelectric performance (Abbasipour et al. 2017; Mokhtari et al. 2017; Sharma et al. 2016). The  $V_{OC}$  was decreased at 5 wt% loading of the filler, which may be due to the reduction of the  $F(EA)$ . The piezoelectric voltage generation in EPVDF and PVDF/BWN composite nanofabrics is due to the piezoelectric potential developed across the surface of the nanogenerator upon the application of external force. The developed piezoelectric potential causes electrons to flow, which are collected by the electrode and supplied to the external load. The reverse output voltage is produced due to the release of external load that brings the nanogenerator back to its initial position.

Fig. 4.10(b) shows the change in  $V_{OC}$  and power density across the different load resistances for the PVDF/BWN-3 based PENG. The voltage and power density were increased as the load resistance increased. The instantaneous power density was calculated using equation (3.2). The maximum instantaneous power density of  $4.3 \mu\text{W}/\text{cm}^2$  was recorded across the load resistance of  $8 \text{ M}\Omega$ .

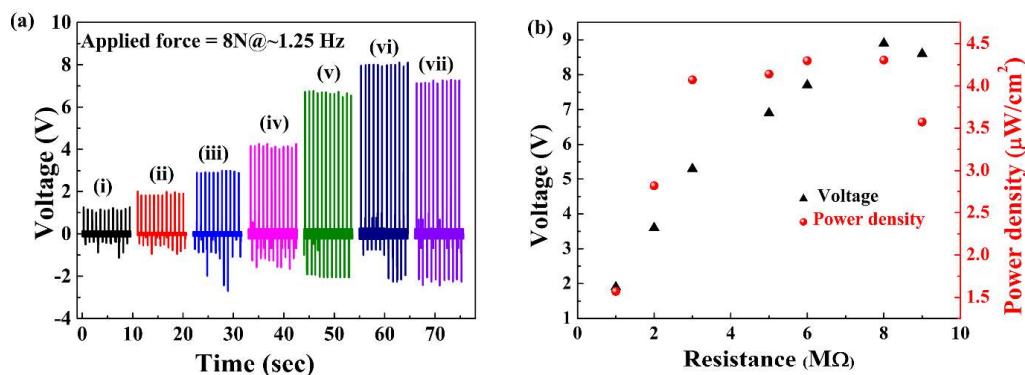


Fig. 4.10 (a) Piezoelectric response of (i) EPVDF, (ii) PVDF/BWN-0.5, (iii) PVDF/BWN-1, (iv) PVDF/BWN-1.5, (v) PVDF/BWN-2, (vi) PVDF/BWN-3, (vii) PVDF/BWN-5, (b) instantaneous power density and  $V_{OC}$  of PVDF/BWN-3 across different load resistances at 10 N applied force.

#### 4.1.2.7 Triboelectric properties

TENG based on EPVDF and PVDF/BWN composite nanofabrics were fabricated as mentioned in the experimental section (Fig. 2.3). In order to evaluate the influence of the BWN loading on the triboelectric performance of the PVDF/BWN composite nanofabrics, TENG was fabricated using composite nanofabrics with different loading of BWN. The performance of the fabricated TENG was evaluated under one finger tapping ( $\sim$  avg 3.8 N @  $4.5 \pm 0.5$  Hz) in contact-separation mode (Fig. 4.11).

The EPVDF based TENG showed a triboelectric  $V_{OC}$  of 112.8 V, where the pressing signal was in the upward direction, and the releasing signal was in the downward direction. The PVDF/BWN composite nanofabric TENGs showed better triboelectric performance than EPVDF based TENG. The triboelectric  $V_{OC}$  was improved upon an increase in the loading of the BWN up to 3 wt%, and at higher filler loading, it was decreased. The TENG based on PVDF/BWN-3 displayed the highest  $V_{OC}$  with a maximum peak output voltage of 200 V. The  $V_{OC}$  of the TENG based on PVDF/BWN-3 has improved performance by  $\sim 1.77$  times as high as that of EPVDF.

The following equation can be used for expressing the triboelectric output voltage of TENG (Chen et al. 2016a):

$$V = \frac{(\sigma_0 - \Delta\sigma) \cdot x(t)}{\varepsilon_0} - \frac{\Delta\sigma \cdot d_c}{\varepsilon_0 \varepsilon_r} \quad (4.1)$$

where  $\varepsilon_0$  and  $\varepsilon_r$  are the permittivity of vacuum and the nanofabrics, respectively. The  $\sigma_0$  and  $\Delta\sigma$  are the triboelectric charge density on the nanofabric and the transferred charge density on the electrode, respectively.  $x(t)$  is the interlayer distance,  $d_c$  is the thickness of the nanofabric, and  $t$  is time.

For  $V_{OC}$ , the above equation will be given as follows:

$$V_{oc} = \frac{\sigma_0 x(t)}{\varepsilon_0} \quad (4.2)$$

The above equation implies that the  $V_{OC}$  depends on the distance of separation and triboelectric charge density. The capacitance of the triboelectric material determines the surface charge density in contact mode TENG because the TENG acts both as energy storage and energy producing device. Therefore, the surface charge density is proportional to the capacitance of the triboelectric material (Chen et al. 2016a; He et al. 2015).

The capacitance is directly proportional to the dielectric constant ( $\varepsilon_r$ ) and the contact surface area for the same thickness of tribo-materials, so it can be concluded that the improvement in the dielectric constant and contact surface area could enhance the triboelectric performance of the TENG. The PVDF/BWN composite nanofabric-based TENG showed an increase in the triboelectric performance with an increase in the loading of BWN up to 3 wt%, beyond which the output decreased. The increase in the triboelectric output of PVDF/BWN composite nanofabrics based TENG could be due to the rise in the dielectric constant. In addition, the enhanced electroactive phase will cause prompt alignment of dipoles, leading to the quick introduction of negative charges onto the surface of composite nanofabrics, which could have improved triboelectric performance (Im and Park 2018; Paranjape et al. 2022; Shi et al. 2021).

However, at a higher loading of the filler, even though the dielectric constant was high, the triboelectric performance was reduced. The decrease in triboelectric

performance at higher loading could be due to the high dielectric loss and reduction in the electroactive phase (Liu et al. 2021). Also, at higher loading, fillers present on the surface of nanofiber will be more, which could potentially reduce the surface contact area of PVDF with copper, causing the reduction in triboelectric performance at higher loading (Fatma et al. 2020).

The instantaneous power density of PVDF/BWN-3 was determined using the measured voltage across various resistances, i.e., 0.39 M $\Omega$  to 13 M $\Omega$ . Equation (3.2) was employed for the calculation of instantaneous power density. As depicted in Fig. 4.11(b), the voltage across resistance increased as the resistance was increased. The maximum instantaneous power density of 646  $\mu\text{W}/\text{cm}^2$  was obtained at 5.2 M $\Omega$ . The triboelectric performance of TENG based on PVDF/BWN-3 was comparable with that of some similar systems reported in the literature (Table I.3).

Furthermore, the structural integrity and triboelectric performance of TENG remained almost unchanged even after  $\sim$ 600 tapping cycles, suggesting the excellent durability of the device (Fig. 4.11(d)). The PVDF/BWN-3 based TENG was used to light commercial LEDs, and a maximum of 40 LEDs were illuminated (Fig. 4.11(e)).

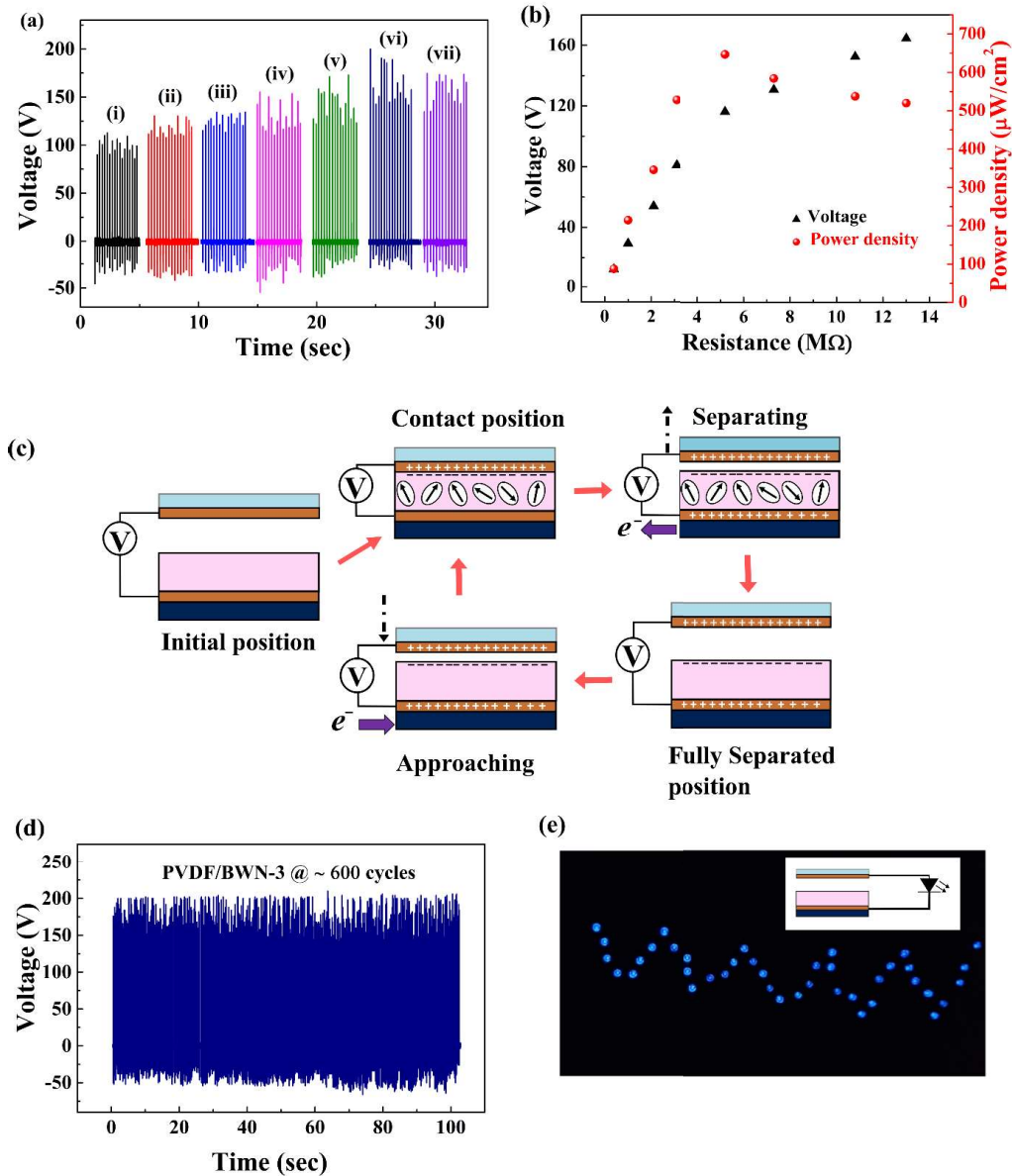


Fig. 4.11 (a) Variation of the triboelectric  $V_{OC}$  of (i) EPVDF, (ii) PVDF/BWN-0.5, (iii) PVDF/BWN-1, (iv) PVDF/BWN-1.5, (v) PVDF/BWN-2, (vi) PVDF/BWN-3, (vii) PVDF/BWN-5, TENG, (b) instantaneous power density and  $V_{OC}$  of PVDF/BWN-3 based TENG across the different values of resistances, (c) schematic illustration of the working mechanism of TENG, (d)  $V_{OC}$  of TENG over ~600 cycles, (e) photograph shows forty LEDs directly connected in series to TENG based on PVDF/BWN-3

nanofabric, which were illuminated by finger tapping force (inset shows schematic of TENG device directly connected to LED).

Fig. 4.11(c) shows the working mechanism of TENG, where the combined effect of the triboelectric effect and piezoelectric effect of EPVDF and PVDF/BWN TENG under contact-separation mode is demonstrated. The fabricated TENG was arch-shaped at one side, where the copper tape was used as the top electrode as well as tribo-positive material for the device. The other side was flat, where the PVDF/BWN composite nanofabric was placed over the copper tape (bottom electrode), which acts as tribo-negative material. At the initial position, there was no contact between the triboelectric surfaces, which led to no charge transfer/generation resulting in no electric potential across the electrodes. Upon the application of external force, the top copper electrode approaches the PVDF/BWN composite nanofabric, and when it comes in contact with the nanofabric causes friction/rubbing between both materials, which leads to the generation of charges at the interface due to the triboelectric effect. The copper tape is positively charged as it gives the electrons, and the PVDF/BWN nanofabric is negatively charged as it accepts the electrons. The piezoelectric material also generates charges under the application of an external load due to the alignment of dipoles in the direction of the applied force. The enhanced negative charge generation due to the piezoelectric effect could promote triboelectric performance. When the force is released, both surfaces are separated, and the charges generated on the surface introduce the opposite charges on the copper electrodes due to electrostatic induction that causes the development of great electrical potential difference between the electrodes. In order to balance the developed electrical potential, the electrons move from the bottom electrode to the top electrode through the external circuit resulting in an electrical signal. Once the top electrode reaches its top position, electrical potential comes to equilibrium, resulting in no further flow of electrons. As the external force is applied on the top surface again, the top copper electrode approaches the bottom layer recreating the opposite potential difference between the electrodes, which forces charges to flow back to the bottom electrode resulting in an electrical signal (Fatma et al. 2020; Paranjape et al. 2022).

The FDTENG was fabricated to harvest energy from wind, as illustrated in Fig. 2.4(a). Fig. 4.12 (a) shows the  $V_{OC}$  of FDTENG at different wind speeds. The  $V_{OC}$  increased as the wind speed increased. The increase in wind speed causes an increase in the fluttering frequency. With the restricted amplitude of the flag, increased frequency causes the contact force to rise between the flag and nanofabric. Due to the high contact force, the surface charge density increases, which could have led to the higher output voltage of FDTENG at the highest wind speed (Xu et al. 2017). The highest  $V_{OC}$  of 84 V at a wind speed of 7 m/s was observed. Meanwhile,  $V_{OC}$  values of 48.4 and 72.8 V were recorded at the wind speeds of 6.3 and 6.6 m/s, respectively.

Fig. 4.12(b) shows the working principle of the FDTENG. As wind flows through the channel at a particular speed, the copper flag starts fluttering, leading to alternate contact and separation between the tribo-positive and tribo-negative materials. As the copper flag comes in contact with PVDF/BWN composite nanofabric, charge transfer occurs between the tribo-positive copper flag and tribo-negative nanofabric due to the triboelectric effect. An electric potential is developed across the copper flag and nanofabric due to electrostatic induction as soon as the flag is separated. This leads to the flow of electrons through the external circuit. When the flag approaches the nanofabric again, the reverse potential is created, causing charges to flow in the reverse direction, thus developing an alternating voltage (Tcho et al. 2022; Xu et al. 2017).

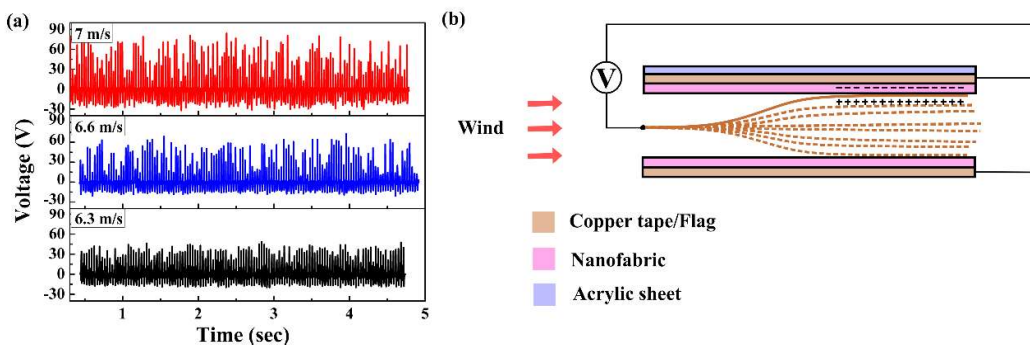


Fig. 4.12 (a) Variation of the triboelectric  $V_{OC}$  of the FDTENG at different wind speeds, and (b) working principle of FDTENG.

# CHAPTER 5

---

The results of this chapter have been published in *RSC Applied Polymers*, 2023, 1, 266 - 280 (**invited paper as part of the themed collection: Celebrating the scientific accomplishments of RSC Fellows**).



## CHAPTER 5

### A NEW MULTIFUNCTIONAL ENERGY HARVESTER BASED ON MICA NANOSHEETS-DISPERSED PVDF NANOFABRICS FEATURING PIEZOCAPACITIVE, PIEZOELECTRIC AND TRIBOELECTRIC EFFECTS

*In this work, PENG and TENG based on PVDF composite nanofabrics-infused MNS were developed. The morphology, crystallinity, and polymorphism of PVDF/MNS composite nanofabrics were studied using different characterization techniques. The incorporation of MNS into PVDF resulted in enhanced  $\beta$ -phase content of PVDF. The composite nanofabrics exhibited enhanced dielectric constant and capacitive sensing ability than that of EPVDF. The piezoelectric and triboelectric performances of composite nanofabrics have enhanced upon the incorporation of MNS into the PVDF matrix.*

#### 5.1 RESULTS AND DISCUSSION

##### 5.1.1 SEM and TEM analysis of the nanofabrics

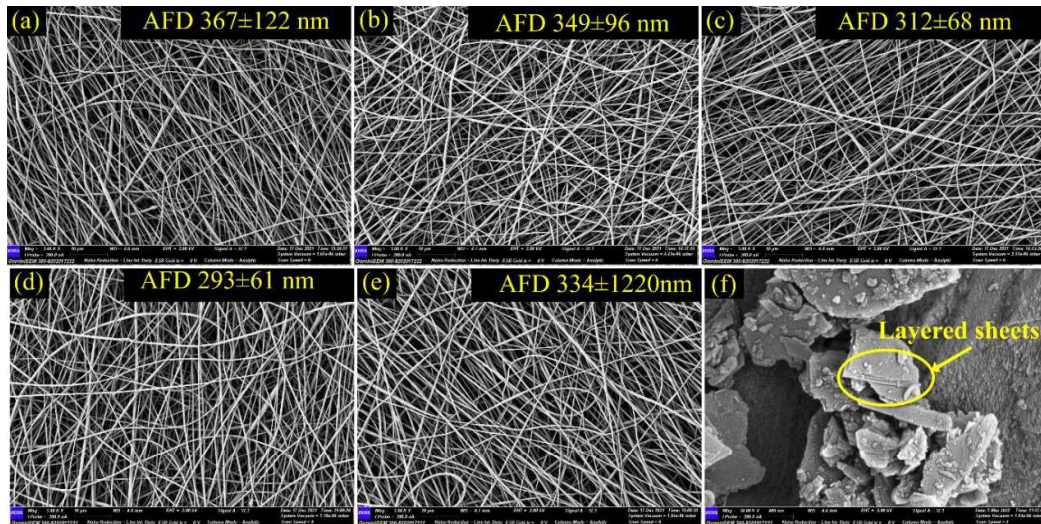


Fig. 5.1 SEM images of (a) EPVDF, (b) PVDF/MNS-0.25, (c) PVDF/MNS-0.5, (d) PVDF/MNS-0.75, (e) PVDF/MNS-1 nanofibers, (f) MNS.

Fig. 5.1(a-e) shows the SEM images of EPVDF and PVDF/MNS composite nanofibers. Fig. 5.1(f) shows the SEM image of MNS that reveals their lamellar structure. The AFD of the nanofibers was reduced upon incorporation of MNS. It was observed that the AFD was decreased up to a loading of 0.75 wt% MNS, after which it increased. The lowest AFD of  $293\pm 61$  nm was recorded for PVDF/MNS-0.75. The incorporation of MNS in precursor solution increased the surface charge density, leading to an enhanced stretching effect during electrospinning which reduced the AFD (Khalifa et al. 2016; Shetty et al. 2020). As the loading of MNS increases in the precursor solution, the viscosity of the solution also rises. The increased viscosity of the solution may have contributed to a reduction in mechanical stretching experienced during electrospinning. This reduction in mechanical stretching led to higher AFD in the composite nanofabrics loaded with 1 wt% of MNS (Rasel and Rizvi 2018; Shetty et al. 2020). The  $d_{33}$  is a direct measure of the piezoelectric performance of piezoelectric materials. Ico et al.(2016) revealed the relationship between the fiber diameter and the  $d_{33}$  in their study, where the  $d_{33}$  was inversely proportional to the fiber diameter (equation 3.1). Thus, the improved  $\beta$ -phase content and piezoelectric performance can be correlated with the fiber diameter. For the PVDF/MNS-1, apart from the reduced mechanical stretching effect, one more reason for the low  $\beta$ -phase content could be the lesser surface area of the MNS for polymer-filler interaction, possibly due to the agglomeration of MNS particles.

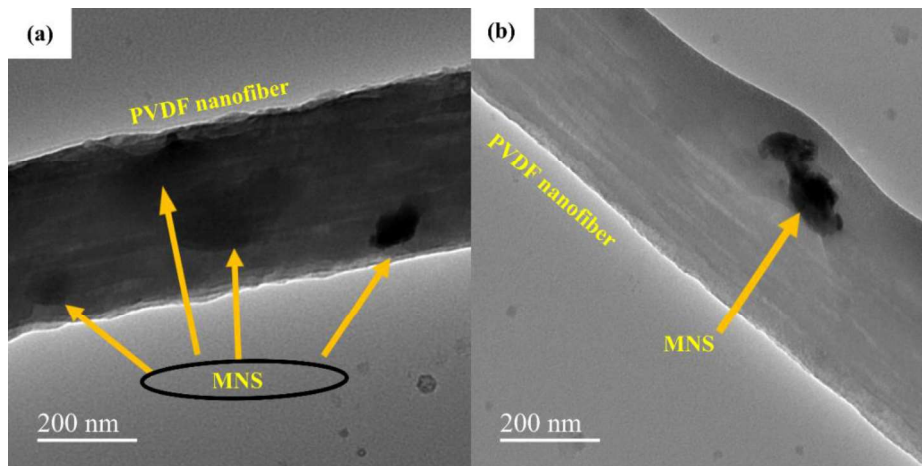


Fig. 5.2. TEM images of PVDF/MNS-0.75 nanofiber at two different locations.

The TEM images of PVDF/MNS-0.75 nanofiber are shown in Fig. 5.2. The PVDF matrix effectively encapsulates the well-dispersed MNS sheets facilitated by the electrospinning process. The fine dispersion of the MNS sheets helps in effective polymer-filler interaction.

### 5.1.2 FTIR spectral analysis

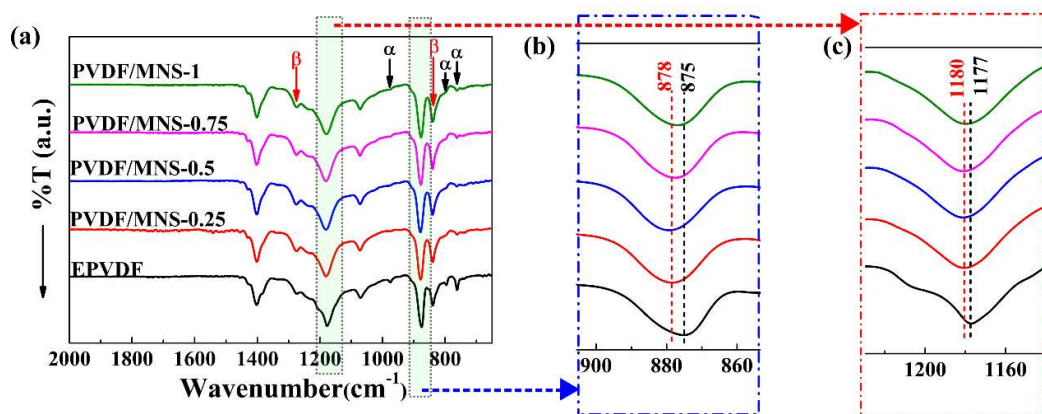


Fig. 5.3 FTIR spectra of EPVDF and PVDF/MNS composite nanofabrics (a) 2000-650  $\text{cm}^{-1}$ , (b) 900-860  $\text{cm}^{-1}$ , (c) 1230-1140  $\text{cm}^{-1}$ .

FTIR spectroscopy was used to analyze the electroactive phase content of EPVDF and PVDF/MNS composite nanofabrics (Fig. 5.3). The presence of the  $\alpha$ -phase is indicated by the peaks at 762, 796, and 974  $\text{cm}^{-1}$ , while the electroactive phase is identified by a peak at 840  $\text{cm}^{-1}$ . The peaks at 1234  $\text{cm}^{-1}$  and 1275  $\text{cm}^{-1}$  represent the signature peaks of the  $\gamma$  and  $\beta$ -phases, respectively (Cai et al. 2017; Martins et al. 2014). The enhanced peak intensity at 840  $\text{cm}^{-1}$  corresponding to the polar phase, coupled with reduced peak intensities at 762, 796, and 974  $\text{cm}^{-1}$  associated with  $\alpha$ -phase, indicates an increase in the electroactive phase content with the incorporation of MNS. Furthermore, the strong peak at 1275  $\text{cm}^{-1}$ , along with the minuscule shoulder peak at 1234  $\text{cm}^{-1}$ , and the absence of other  $\gamma$ -phase peaks such as 776, 811, and 833  $\text{cm}^{-1}$  indicate the dominance of the polar  $\beta$ -phase in the composite nanofabrics (Fig. 5.3(d)) (Shetty et al. 2021). Therefore, the  $\gamma$ -phase was not considered for further analysis. The peak at 875  $\text{cm}^{-1}$ , associated with C-C asymmetric stretching, exhibited a shift to the range of 876-879  $\text{cm}^{-1}$ , while the peak at 1177  $\text{cm}^{-1}$ , corresponding to the  $\text{CF}_2$  symmetric stretching, showed a shift to a range of 1179-1180  $\text{cm}^{-1}$  in the composite nanofabrics (Sharma et

al. 2015; Shetty et al. 2021) (Fig. 5.3 (b) and (c)). The observed shifts in the vibrational bands suggest significant interaction between the MNS and the PVDF chains, facilitating the conversion of the  $\alpha$ -phase into the  $\beta$ -phase. The  $F(\beta)$  in PVDF/MNS composite nanofabrics were calculated using equation (2.1).

In EPVDF, the the  $\beta$ -phase content was 63.6%. On the other hand, the  $F(\beta)$  of PVDF increased in the presence of MNS in the composite nanofabrics. The  $F(\beta)$  increased with the loading of MNS up to 0.75 wt%, reaching 86.3%; after that, it declined. The  $\beta$ -phase content of electrospun nanofabrics is shown in Table 5.1. The enhancement in  $F(\beta)$  may be attributed to a synergistic effect of the polymer-filler interaction, weak solvent polymer chain interaction, and the influence of electrospinning. The  $\text{CH}_2$  group of PVDF may have weakly interacted with the  $\text{C}=\text{O}$  of DMF through hydrogen bonding, facilitating the emergence of polar phases by lowering the energy barrier for the same (Ekbote et al. 2021; Khalifa et al. 2021). Also, polymer-filler interaction promoted the alignment of PVDF chains in all-trans conformation. Here, the interaction between the O-atoms of MNS and the  $\text{CH}_2$  group of the PVDF chains and the hydrogen bonding between the hydroxyl groups of MNS and the  $\text{CF}_2$  groups of the PVDF might have played a significant role in the improvement in the  $\beta$ -phase content. Also, the negatively charged MNS ( $\zeta$ -potential (average) = -33.4 mV) (Fig. I.3) could have interacted with  $\text{CH}_2$  of PVDF, enhancing the  $\beta$ -phase content in PVDF (Fig. 5.4) (Khalifa et al. 2021).

Table 5.1.  $F(\beta)(\%)$  and  $\chi_{c(WAXD)}(\%)$  of PVDF/MNS composite nanofabrics.

| <b>Nanofabrics</b> | <b>F(<math>\beta</math>)%</b> | <b>Total crystallinity by WAXD<br/>(<math>\chi_{c(WAXD)}(\%)</math>)</b> |
|--------------------|-------------------------------|--|
| EPVDF              | 63.6                          | 36.5   |
| PVDF/MNS-0.25      | 79.6                          | 42.9   |
| PVDF/MNS-0.5       | 81.8                          | 44.7   |
| PVDF/MNS-0.75      | 84.3                          | 46.8   |
| PVDF/MNS-1         | 83.4                          | 45.4   |

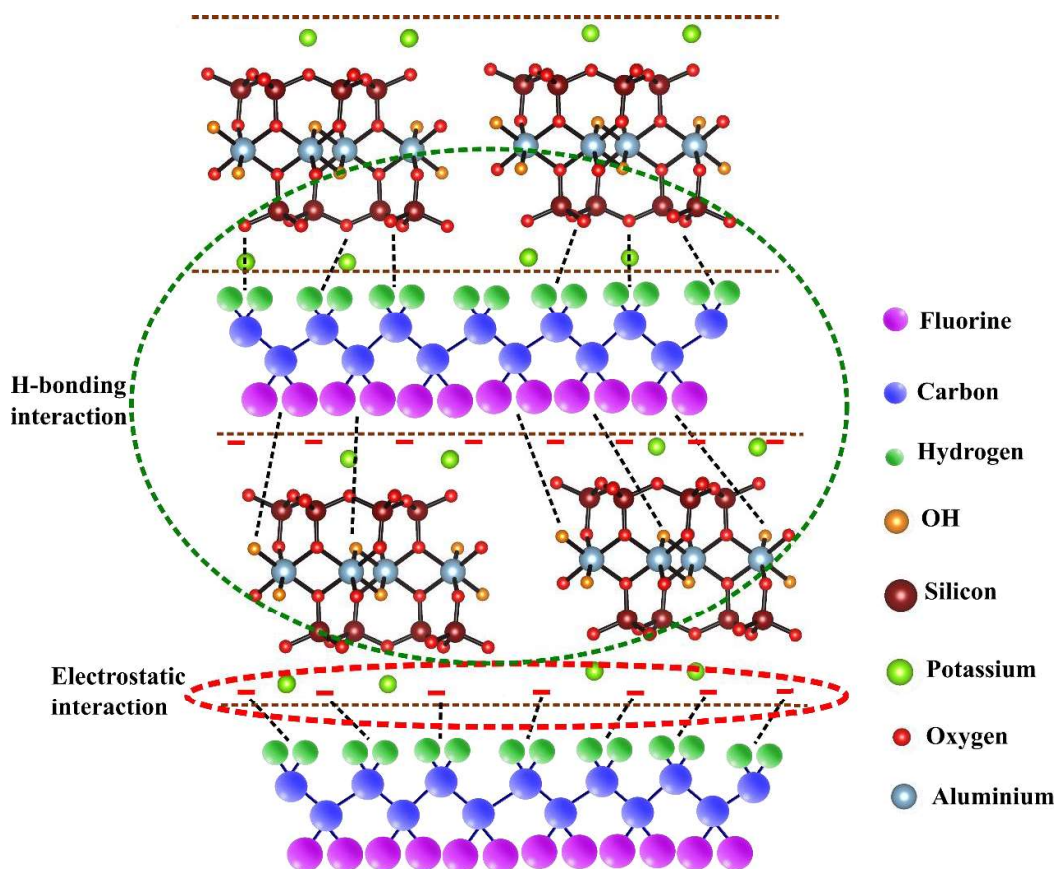


Fig. 5.4 Visual depiction illustrating the potential mechanism of interaction between MNS and PVDF chains (Momma and Izumi 2011).

### 5.1.3 WAXD analysis

WAXD was used to analyze the phases and crystallinity in EPVDF and PVDF/MNS composite nanofabrics (Fig. 5.5). In EPVDF, the peak pertaining to  $18.3^\circ$  (0 2 0) and  $27^\circ$  (0 2 1) represent the  $\alpha$ -phase, and the peaks at  $20.6^\circ$  (1 1 0/ 2 0 0) and  $36.3^\circ$  (2 0 1) represent the  $\beta$ -phase, indicating the presence of  $\alpha$  and  $\beta$ -phases (Esterly and Love 2004; Martins et al. 2014). Upon the addition of MNS, the intensity of the  $\alpha$ -phase peak was weakened, and the intensity of the  $\beta$ -phase peak was intensified, suggesting improvement in  $F(\beta)$ . Moreover, the peaks at  $8.7^\circ$ ,  $17.7^\circ$ , and  $26.5^\circ$  belong to MNS (ICDD-00-006-0263), which confirms the presence of MNS in the composite nanofabrics. Also, the diffraction peak of the  $\alpha$ -phase at  $27^\circ$  was diminished and masked by the diffraction peak of MNS. In accordance with the FTIR results, the WAXD results also suggest that the addition of MNS improved the  $F(\beta)$  of PVDF.

Deconvoluted X-ray diffractograms were used to determine the total crystallinity of the nanofabrics (Fig. 5.6). The incorporation of MNS resulted in an increase in the overall crystallinity of the nanofabrics. The nanolayer surface of the filler particles in the composite nanofabrics serve as nucleation sites, interacting with the polymer chains during the electrospinning process, thereby promoting the crystallinity of PVDF (AlAhzm et al. 2021; Bharath et al. 2019; Jahan et al. 2017; Tsonos et al. 2019). However, at 1 wt% loading of MNS, the surface area available for nucleation is reduced possibly due to agglomeration of MNS, which led to a decrease in total crystallinity of PVDF/MNS-1.

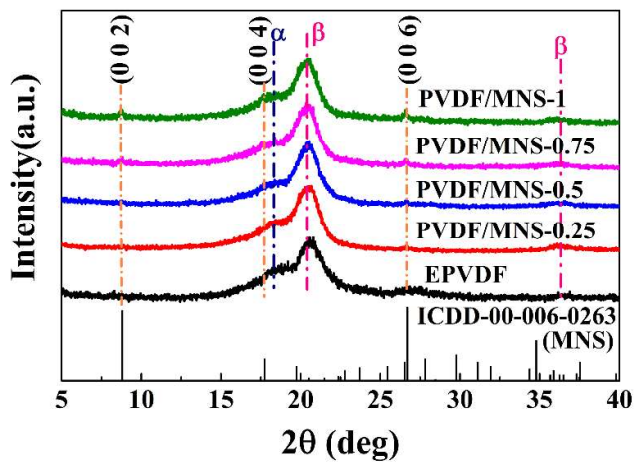


Fig. 5.5 X-ray diffractograms of EPVDF and PVDF/MNS composite nanofabrics.

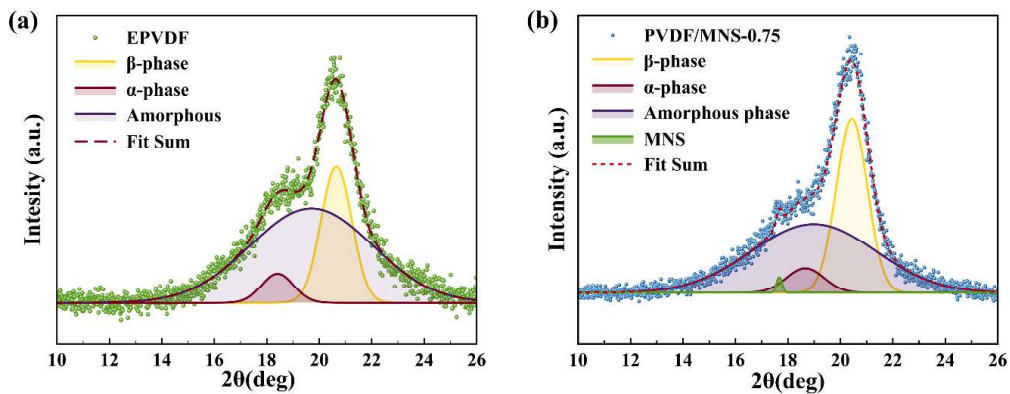


Fig. 5.6 Deconvoluted X-ray diffractograms of (a) EPVDF and (b) PVDF/MNS-0.75.

## 5.1.4 Dielectric studies

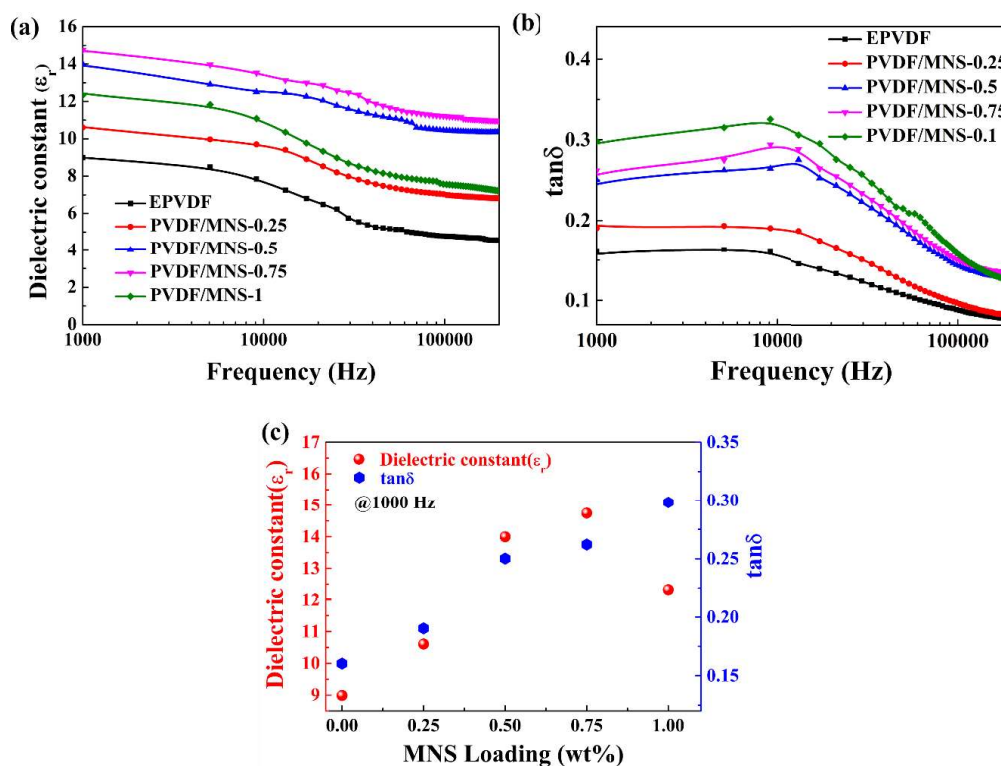


Fig. 5.7 (a) Dielectric constant and (b) dielectric loss of EPVDF and PVDF/MNS composite nanofabrics as a function of frequency, (c) variation of dielectric constant and dielectric loss with respect to MNS loading (at 1000 Hz) of the nanofabrics.

Dielectric properties of EPVDF and PVDF/MNS composite nanofabrics were measured at 25°C across the 1000 Hz- 200 kHz frequency range. Fig. 5.7 illustrates the dielectric properties of the nanofabrics with different loading of MNS as a function of frequency. The dielectric constant of composite nanofabrics was significantly improved with the incorporation of MNS. At 1000 Hz, the PVDF/MNS-0.75 had the maximum dielectric constant value of 14.7, which was 64 % greater than that of EPVDF. The enhancement of the dielectric constant at lower frequencies may be a result of the interfacial polarization (Shamitha et al. 2020). The overall improvement in the dielectric constant could be ascribed to the following contributing factors: first, the enhanced  $\beta$ -phase content (Shetty et al. 2019; Ye et al. 2013), and second, the incorporation of MNS (Dash et al. 2019; Khalifa et al. 2021). At the highest loading of MNS, the dielectric constant considerably decreased, which could be attributed to a

decline in the  $\beta$ -phase content and poor dispersion of MNS. In general, the dielectric constant value progressively decreases as the frequency of the applied electric field increases, which is due to the failure of the dipoles to align with the field (Lu et al. 2017; Shetty et al. 2019).

Dielectric loss in polymer composites depends on the dipolar, distortion, and interfacial polarization. In addition, conduction loss also contributes to the dielectric loss (Prateek et al. 2016). The dielectric loss of PVDF/MNS composite nanofabrics was higher than that of EPVDF. The increase in the dielectric loss may be attributed to the formation of small domain networks resulting from the addition of MNS, which leads to enhanced interfacial polarization and conduction loss (Hu et al. 2015). The broad peak of dielectric loss at higher frequency could be due to dipolar/orientation polarization. Additionally, the dielectric properties of composite nanofabrics are influenced by the morphology of the filler, dispersion of the filler, and polymer-filler interaction (Dash et al. 2017). The porous structure of nanofabric also affects the dielectric properties by varying dipole density (Shetty et al. 2019). The ability of a material to store charges is represented by its dielectric constant, while the dielectric loss indicates its leakiness. Materials with high dielectric constants can offer enhanced triboelectric charge density, whereas those with low dielectric loss can efficiently hold charges. Therefore, selecting a material that exhibits a high dielectric constant and a low dielectric loss is essential for optimal triboelectric performance.

### 5.1.5 Piezo capacitance evaluation

The performance of the capacitive sensor was evaluated using a standard linear motor kit, where the applied force was perpendicular to the sensor (Fig. 2.1 (a) and 2.2). The PVDF/MNS-0.75 was chosen for further investigation among the prepared composites because of its high dielectric constant. To create the capacitive sensor, the PVDF/MNS-0.75 was placed between two copper electrodes (parallel plate capacitor configuration).

Fig. 5.8 shows the responses of the capacitive sensor based on EPVDF and PVDF/MNS-0.75 to an external load. The PVDF/MNS-0.75 based capacitive sensor's response ( $\Delta C/C_0$ ) was  $\sim 4.4$  times higher than that of the EPVDF based sensor when

subjected to 9 N force. The curve depicting the response ( $\Delta C/C_0$ ) as a function of the applied external force was plotted for the PVDF/MNS-0.75 based sensor, and the sensitivity was calculated by measuring the slope of the curve. The two sections were overserved with distinct sensitivities; the first, within a low force range (2-9 N), demonstrated a sensitivity of 0.6/N, while the second, high force range (10-20 N), exhibited a sensitivity of 0.1/N. At higher applied forces, the sensor's sensitivity was reduced. The change in distance and effective dielectric constant of the sensor are crucial factors in the determination of the sensor's sensitivity. When prominent deformation of nanofabric is reduced, and porosity is eliminated at higher force, the change in distance, as well as effective dielectric constant, is minimum, resulting in reduced sensitivity of the sensor. The same trend was observed in PVDF/MNS-0.75 based sensor.

Capacitance is determined by the dielectric constant, the distance between the electrodes, and electrode contact area. The change in capacitance of the nanofabric may be due to two reasons: first, the force applied may reduce the distance between electrodes, thereby increasing the capacitance. Second, the material's dielectric constant may change due to the external load, leading to an increase in the sensor's effective dielectric constant caused by the reduction of pores, however, the dielectric constant of composite nanofabrics is crucial factor in determining effective dielectric constant (Kwon et al. 2016; Yang et al. 2019; Zhu et al. 2020). These pores could reappear upon the removal of the externally applied load. The improved sensing property of the PVDF/MNS-0.75 could be ascribed to its higher dielectric constant value and porosity within the material. This capacitive sensor holds potential for applications in pressure sensors, tactile sensing, and wearable devices (Ma et al. 2018).

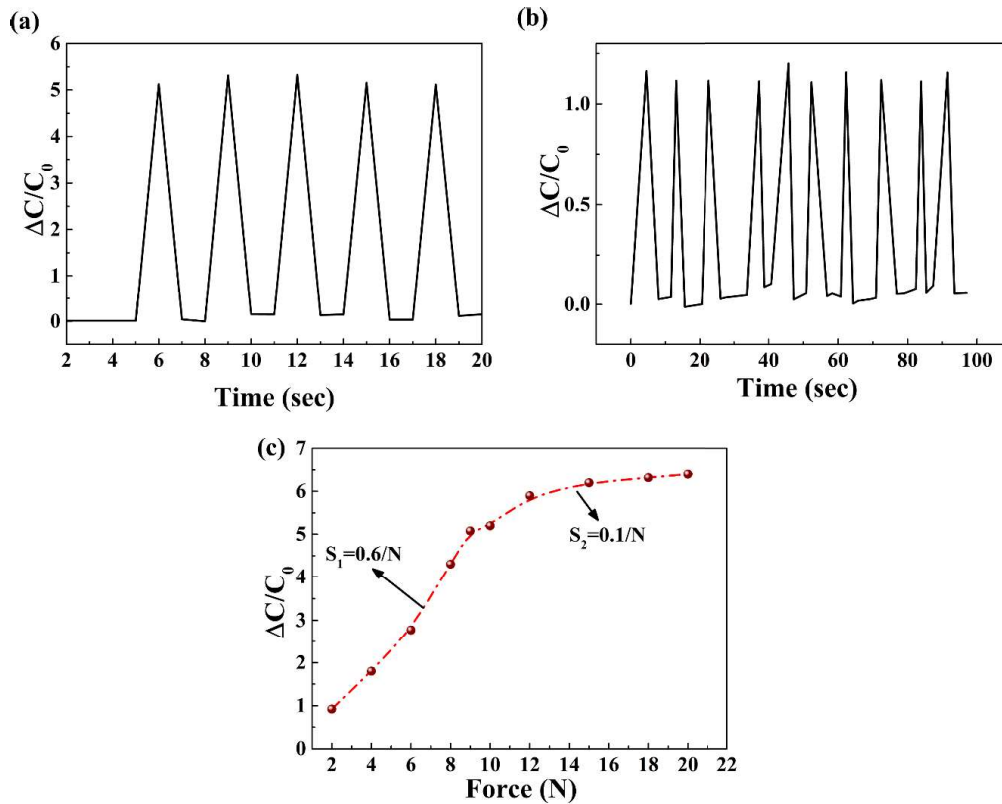


Fig. 5.8 (a) The response ( $\Delta C/C_0$ ) of PVDF/MNS-0.75 based capacitive sensor (under 9 N load), (b) the response ( $\Delta C/C_0$ ) of EPVDF based capacitive sensor (under 9 N load), and (c) ratio of relative change in capacitance to the initial capacitance of the sensor as a function of the applied load.

### 5.1.6 Piezoelectric performance

The response of PENG based on EPVDF and PVDF/MNS composite nanofabrics was evaluated under 8 N force (Fig. 5.9) applied using a linear motor kit in the normal direction (Fig. 2.2). The  $V_{OC}$  of PENG based on composite nanofabrics was improved upon the incorporation of MNS into the PVDF matrix. PVDF/MNS composite nanofabrics based PENGs demonstrated better piezoelectric performance due to their improved  $\beta$ -phase content (Khalifa et al. 2016; Shetty et al. 2020). The  $V_{OC}$  increased as the filler loading increased, peaking at 0.75 wt% of MNS, and the maximum  $V_{OC}$  of 8.4 V was attained when subjected to 8 N force. Additionally, the piezoelectric behavior of composite nanofabrics may depend on the nanofiller's morphology and surface

characteristics, as well as the humidity levels maintained during the electrospinning (Abbasipour et al. 2017; Mokhtari et al. 2017; Sharma et al. 2016). As the loading of fillers exceeded 0.75 wt%, there was a decrease in the  $V_{OC}$ , potentially due to a decline in the  $\beta$ -phase content at 1wt% of MNS loading.

Upon the application of an external force, the dipoles orient themselves in response to the force. As a result, a piezoelectric potential is generated across the top and bottom surfaces of the electrode. The piezoelectric potential between the top and bottom electrode causes electrons to flow across the external circuit, which produces an electric signal. When the applied force is removed, the dipoles return to their initial position, and the electrons flow back in the opposite direction leading to a reverse signal.

PVDF/MNS-0.75 based PENG was used for power density measurement since it showed the highest  $V_{OC}$ . In order to calculate the power density, voltage across the load resistance was measured. In response to an increase in load resistance, the voltage increased. At a load resistance of 2  $M\Omega$ , a peak power density of 3  $\mu W/cm^2$  was attained. The instantaneous power density was determined using equation (3.2).

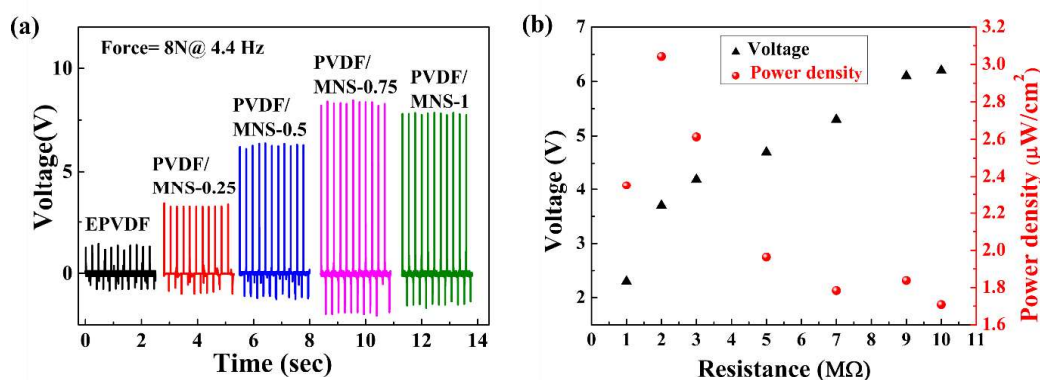


Fig. 5.9 (a) Piezoelectric response of EVPDF and PVDF/MNS composite nanofabrics based PENG with varying loading of MNS, (b) piezoelectric voltage generated, and instantaneous power density of PVDF/MNS-0.75 based PENG across the different resistances (applied force of 8 N).

## 5.1.7 Triboelectric performance

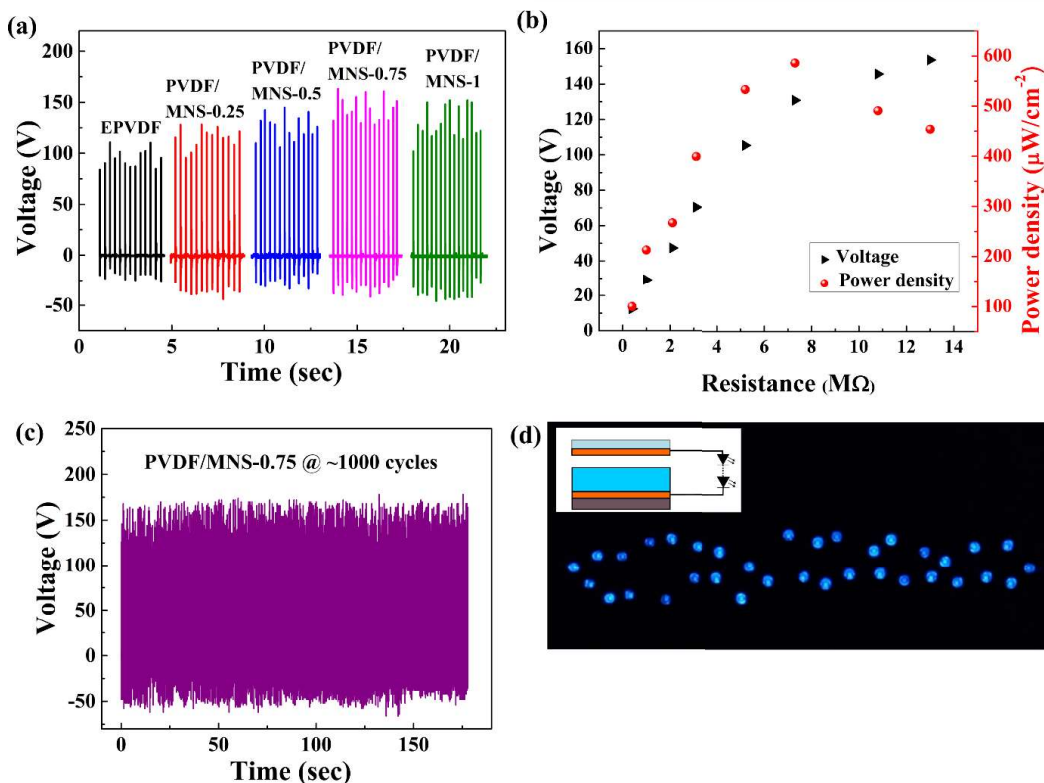


Fig. 5.10 (a) Triboelectric response of the TENG based on nanofabrics with different loading of MNS, (b) voltage response and instantaneous power density at different load resistances, (c) triboelectric response of PVDF/MNS-0.75 based TENG for ~1000 cycles, (d) the photograph of thirty-five LEDs connected to TENG based on PVDF/MNS-0.75 in series, lit under one finger tapping (inset: schematic of LEDs connected to TENG in series).

TENGs based on composite nanofabrics containing different amounts of MNS were prepared to evaluate the effects of MNS on the triboelectric response (Fig. 5.10). The fabrication process of the triboelectric nanogenerators is detailed in the experimental section, and the schematic of the same is depicted in Fig. 2.3. The TENGs were evaluated under the application of one finger tapping force ( $\sim$ avg 3.8 N) in contact-separation mode. The  $V_{\text{OC}}$  of 110 V was observed for EPVDF based TENG. The  $V_{\text{OC}}$  values of 128, 142, 163, and 152 V were recorded for TENGs made from

PVDF/MNS-0.25, PVDF/MNS-0.5, PVDF/MNS-0.75, and PVDF/MNS-1, respectively. The performance of TENGs based on composite nanofabrics were enhanced upon the addition of MNS. The triboelectric output showed an upward trend with the increase in MNS loading, peaking at 0.75 wt% MNS loading. A maximum triboelectric  $V_{OC}$  of 163 V was generated by PVDF/MNS-0.75 based TENG. However, a further increase in MNS loading led to a decline in the triboelectric voltage output. The TENG consisting of composite nanofabric with 0.75 wt% of MNS exhibited a triboelectric output  $\sim 1.48$  times higher than that of the TENG based on EPVDF. The triboelectric output voltage can be described by equation (4.1). The equation for  $V_{OC}$  was derived from equation (4.1) and was described using equation (4.2) (Chen et al. 2016a).

The  $V_{OC}$  of TENG is determined by the triboelectric charge density and distance of separation, as shown in equation (4.2). In a contact-separation mode TENG, the capacitance of the triboelectric material plays a crucial role in determining the surface charge density, as the device has the ability to both store and generate energy. Therefore, the capacitance of the triboelectric material serves as a determining factor for the surface charge density in the contact-separation mode (Chen et al. 2016a; He et al. 2015; Ippili et al. 2021). It is worth noting that a material's capacitance is determined by its dielectric constant and the effective contact area, assuming uniform thickness. As a result, improving both the effective contact area and dielectric constant would enhance the triboelectric response of the TENG.

The enhanced triboelectric performance of PVDF/MNS composite nanofabrics could be attributed to its improved dielectric properties. Furthermore, the improved  $\beta$ -phase content enhances its triboelectric performance by rapidly introducing charges onto the composite nanofabrics (Im and Park 2018; Paranjape et al. 2022; Shi et al. 2021). A lower dielectric constant, a lower  $\beta$ -phase content, and increased dielectric loss were all contributing factors to reduced triboelectric output at the highest loading of the MNS (Im and Park 2018; Ippili et al. 2021; Liu et al. 2021; Paranjape et al. 2022; Shi et al. 2021; Zhang et al. 2022).

Since PVDF/MNS composite nanofabric containing 0.75 wt% of MNS showed the highest  $V_{OC}$ ; as a result, PVDF/MNS-0.75 was used for the instantaneous power density measurement (Fig. 5.10(b)). The voltage measured across different load resistances (0.39 M $\Omega$  to 13 M $\Omega$ ) was used for the calculation of the instantaneous power density. The voltage generated across the load resistance increased with the increase in load resistance value. The instantaneous power density was calculated using equation (3.2). It was possible to obtain a maximum power density of  $\sim 585 \mu\text{W}/\text{cm}^2$  across a load resistance value of 7.3 M $\Omega$ . The PVDF/MNS composite nanofabric based TENG's performance is on par with the systems in the previously published literature (Table I.3).

Roughness of the tribolayers affects the device's triboelectric performance and durability. The surface morphology and roughness of the copper tape were studied to ensure its flatness. The copper tape surface was found to exhibit a flat line-type microstructured pattern (Fig. I.1 and I.2), with an average roughness value  $R_a$  of 0.2 to 0.215  $\mu\text{m}$  (Table I.2), indicating that the surface is flat, which is beneficial for the durability of the TENG. Due to the soft nature of PVDF/MNS nanofabrics, the flatness of copper aids in the device's durability. The TENG's electrical performance showed no evidence of degradation after  $\sim 1000$  cycles, demonstrating its durability and structural integrity (Fig. 5.10(c)). The 35 LEDs connected in series with TENG based on PVDF/MNS-0.75 were illuminated under the force exerted by one finger tapping (Fig. 5.10(d)). The operational mechanism of the fabricated TENG has been thoroughly discussed in section 4.1.8, and Fig. 4.11(c) depicts its working principle.

FDTENG was developed to capture wind energy (Fig. 2.4). The triboelectric performance of FDTENG under various wind speeds is depicted in Fig. 5.11(a). With there is a rise in the wind speed, the  $V_{OC}$  of FDTENG exhibits an upward trend. The limited motion of the fluttering film leads to an increased contact force between the copper film and composite nanofabric. This phenomenon is attributed to an increase in the fluttering frequency induced by the increased wind speed (Xu et al. 2017). The maximum  $V_{OC}$  recorded at 7 m/s was 70 V, which was the highest compared to the  $V_{OC}$  at the other two speeds. At wind speeds of 6.3 m/s and 6.6 m/s, the FDTENG generated

$V_{OC}$  of 39 V and 58 V, respectively. The working mechanism of FDTENG is shown in Fig. 5.11(b). Initially, the fluttering film remains stationary due to the absence of wind flow, but as soon as the wind flows at a particular speed, it flutters. The fluttering creates periodic contact and separation between the fluttering film and the composite nanofabric. When the fluttering film comes in contact with the composite nanofabric, it generates triboelectric charges. Subsequently, as the tribo-negative and tribo-positive layers separate, the charges present at the interface of the composite nanofabric induce opposite charges on the electrode through electrostatic induction. These charges create a strong electric field between the fluttering film and the electrode, enabling the electron flow across an external circuit, resulting in the generation of an electric current. When the fluttering film approaches again, an opposite electric potential is created, which causes electrons to flow in the reverse direction, creating an electrical signal in the opposite direction (Tcho et al. 2022; Xu et al. 2017).

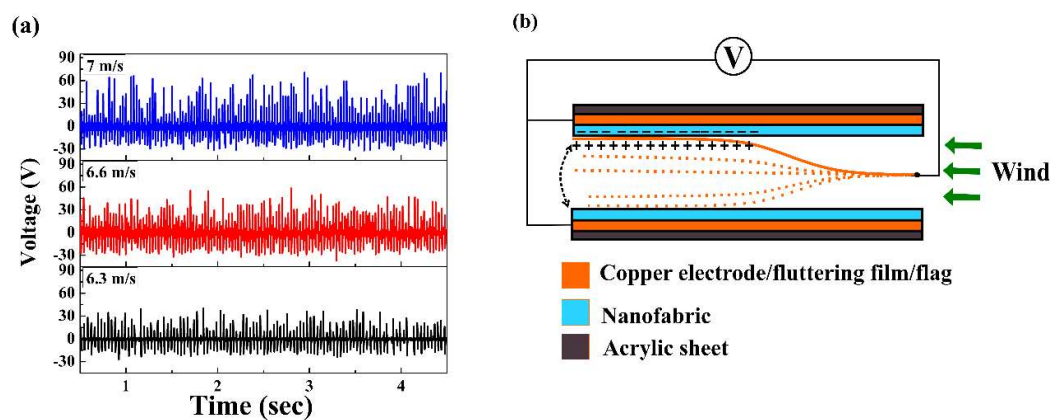


Fig. 5.11 (a) Triboelectric performance of PVDF/MNS-0.75 based FDTENG when exposed to varying wind speeds, (b) schematic of the working mechanism of FDTENG.



# **CHAPTER 6**



## CHAPTER 6

### SUMMARY AND CONCLUSIONS

---

The PVDF based nanofabrics with enhanced electroactivity were developed using electrospinning. The incorporation of the cationic surfactant (tetra-n-butyl ammonium chloride) and mica nanosheets reduced the average fiber diameter (AFD) of PVDF composite/doped nanofibers due to an increase in stretching effect, while the incorporation of barium nanorods (BWN) increased the AFD of PVDF composite nanofibers due to increased viscosity of the precursor solution. The enhanced  $\beta$ -phase content in TBAC-based nanofabrics may be attributed to the improved stretching effect augmented by increased charge density of precursor solution and ion-dipole interaction between TBAC and PVDF chains. In the case of MNS-infused PVDF nanofabrics, the H-bonding and electrostatic interaction between MNS and PVDF chain and enhanced stretching effect boosted the  $\beta$ -phase content of PVDF nanofabrics. Lastly, in BWN-incorporated electrospun PVDF nanofabrics; the electrostatic/interfacial interaction was a crucial factor in the enhancement of the electroactive phase content of PVDF nanofabrics. The PVDF nanofabric, with a loading of 3 wt% of TBAC, demonstrated the highest  $\beta$ -phase content of 89%. Meanwhile, the inclusion of 3 wt% BWN resulted in an electroactive phase content of 86.5%, and the addition of 0.75 wt% MNS showed an  $\beta$ -phase content of 84.3%. The total crystallinity of the PVDF/TBAC nanofabric decreased, whereas it increased in the case of PVDF/BWN and PVDF/MNS based composite nanofabrics.

The piezoelectric and dielectric properties of PVDF nanofabrics were enhanced upon the inclusion of nanoscale fillers or cationic surfactant. A PENG based on PVDF nanofabrics containing 3 wt% of TBAC generated a  $V_{OC}$  of 17.2 V and an instantaneous power density of  $1.4 \mu\text{W}/\text{cm}^2$ . The PENG based on the nanofabric containing 3 wt% BWN produced  $V_{OC}$  up to 8 V and power density up to  $\sim 4.3 \mu\text{W}/\text{cm}^2$ . The piezoelectric nanogenerator employing PVDF composite nanofabric with loading a 0.75 wt% MNS demonstrated a  $V_{OC}$  of 8.4 V and achieved a power density of  $\sim 3 \mu\text{W}/\text{cm}^2$ . The piezo capacitance of composite nanofabrics was increased upon the incorporation of BWN and MNS. The sensitivity values of 0.66/N and 0.6/N were achieved in composite nanofabrics containing 3 wt% of BWN and 0.75 wt% of MNS, respectively. Enhanced

dielectric properties and higher electroactive phase content significantly contributed to the improvement of the triboelectric performance of the composite nanofabrics. Under one finger tapping, the triboelectric nanogenerator fabricated using PVDF composite nanofabric containing 3 wt% of BWN generated a triboelectric output of 200 V and an instantaneous power density of  $\sim 646 \mu\text{W}/\text{cm}^2$ . The TENG developed based on PVDF composite nanofabric containing 0.75 wt% of MNS exhibited a  $V_{\text{OC}}$  of 163 V and an instantaneous power density of  $\sim 585 \mu\text{W}/\text{cm}^2$ , whereas the TENGs fabricated based on PVDF composite nanofabric containing 3 wt% of BWN and PVDF composite nanofabric containing 0.75 wt% of MNS were capable of illuminating 40 and 35 LEDs, respectively. The developed fluttering-driven triboelectric nanogenerator, incorporating PVDF composite nanofabrics with 3 wt% of BWN and 0.75 wt% of MNS, demonstrated an impressive electric output of 84 V and 70 V, respectively, at a wind speed of 7 m/s.

In summary, the utilization of cationic surfactant and nanofillers, and their interactions with PVDF chains, played a crucial role in promoting the formation of the electroactive phases in PVDF nanofabrics. In this work, the synergistic of electrospinning and cationic surfactant/nanofillers have been employed effectively to significantly enhance the dielectric properties, piezo capacitance, piezoelectric and triboelectric performance of PVDF nanofabrics. Thus, the composite/doped nanofabrics developed in this study could be a potential power source for miniature devices, IoT, and wearables.

The following scheme summarizes the properties observed in the developed PVDF based nanofabrics in this study.

## CHAPTER 6

|   |  |   |
|---|--|---|
| <p><b>Electrospun PVDF/TBAC doped nanofabrics</b></p> <p><b>Solvent: DMF</b><br/> <b>Concentration of PVDF: 13.5 w/v%</b><br/> <b>TBAC loading: 1, 2, 3, and 5 wt%</b></p> <p><b>Piezoelectric energy harvester</b></p>                     | <p><b>Electrospun PVDF/BWN composite nanofabrics</b></p> <p><b>Solvent: DMF/Acetone (9:1)</b><br/> <b>Concentration of PVDF: 13.5 w/v%</b><br/> <b>BWN loading: 0.5, 1, 1.5, 2, 3, and 5 wt%</b></p> <p><b>Piezo capacitive sensor, Piezoelectric energy harvester, Triboelectric energy harvester.</b></p>  | <p><b>Electrospun PVDF/MNS composite nanofabrics</b></p> <p><b>Solvent: DMF/Acetone (9:1)</b><br/> <b>Concentration of PVDF: 13.5 w/v%</b><br/> <b>MNS loading: 0.25, 0.5, 0.75, and 1 wt%</b></p> <p><b>Piezo capacitive sensor, Piezoelectric energy harvester, Triboelectric energy harvester.</b></p>   |
| <p><b>AFD: 265±74 nm</b><br/> <b>Ion-dipole interaction between PVDF chains and TBAC</b><br/> <b>β-phase content %: 89%</b><br/> <b>Max <math>V_{oc}</math>: 17.2 V</b><br/> <b>Instantaneous power density: 1.4 μW.cm<sup>-2</sup></b></p> | <p><b>AFD: 448±142 nm</b><br/> <b>Electrostatic/interfacial interaction between PVDF chains and BWN</b><br/> <b>Electroactive content %: 86.5%</b><br/> <b>Piezo capacitive sensitivity: 0.66/N</b><br/> <b>Max Piezoelectric <math>V_{oc}</math>: 8 V</b><br/> <b>Piezoelectric power density: 4.3 μW.cm<sup>-2</sup></b><br/> <b>Max Triboelectric <math>V_{oc}</math>: 200 V</b><br/> <b>Triboelectric power density: 646 μW.cm<sup>-2</sup></b><br/> <b>Fluttering driven TENG <math>V_{oc}</math>: 84 V</b></p> | <p><b>AFD: 293±61 nm</b><br/> <b>H-bonding and Electrostatic interaction between MNS and PVDF chains.</b><br/> <b>B-phase content %: 84.3%</b><br/> <b>Piezo capacitive sensitivity: 0.6/N</b><br/> <b>Max Piezoelectric <math>V_{oc}</math>: 8.4 V</b><br/> <b>Piezoelectric power density: 3 μW.cm<sup>-2</sup></b><br/> <b>Max Triboelectric <math>V_{oc}</math>: 163 V</b><br/> <b>Triboelectric power density: 585 μW.cm<sup>-2</sup></b><br/> <b>Fluttering driven TENG <math>V_{oc}</math>: 70 V</b></p> |

The mentioned results in this scheme are of optimum loading of nanoscale fillers and cationic surfactant.

## CHAPTER 6

## SCOPE FOR FURTHER WORK

---

- PVDF based nanofabrics could be used to develop a combination of piezoelectric and triboelectric hybrid energy harvesting systems.
- PVDF based nanofabrics could be explored in fuel cells, supercapacitors, filtration membranes, and hydrogen storage.
- The PVDF based nanofabric could be explored in self-charging Li/Na ion batteries as a separator.
- The ferroelectric and pyroelectric nature of PVDF based nanofabrics could be explored.
- The optimized model of piezoelectric and triboelectric energy harvesters in terms of materials, devices, and electric circuits could be developed to be used in real life.



## APPENDIX -I

**Table I.1** Comparison of piezoelectric performance of PVDF/TBAC doped nanofabric based PENG with reported PVDF/Ionic liquid or alkyl ammonium salts in literature.

| <b>Composition of nanogenerator</b>  | <b>Output voltage</b>     | <b>Output current</b>     | <b>Power density</b>                      | <b>Reference</b>                |
|--|---------------------------|---------------------------|---|---------------------------------|
| PVDF/1-octadecyl-3-methylimidazolium bromide ([OMD]Br)(Ionic liquid) nanofabrics | 7.89 ± 1.84 V             | 0.025 μA                  | 0.195 μW/ cm <sup>2</sup>                 | (Mahdavi Varposhti et al. 2020) |
| PVDF/1-ethyl-3-methylimidazolium tetrafluoroborate (Ionic liquid) Film           | ~2 V                      | -                         | -   | (Ting et al. 2020)              |
| PVDF/TBAC nanofabrics  | 2.6 V (under 10 N)        | 3.1 μA                    | -   | (Zaarour et al. 2020)           |
| <b>PVDF/TBAC nanofabrics</b>   | <b>17.2 V (under 5 N)</b> | <b>70 nA (under 1 MΩ)</b> | <b>1.4 μW/ cm<sup>2</sup> (under 3 N)</b> | <b>This work</b>                |

## 1. Surface roughness measurement of Cu tape/Cu electrode

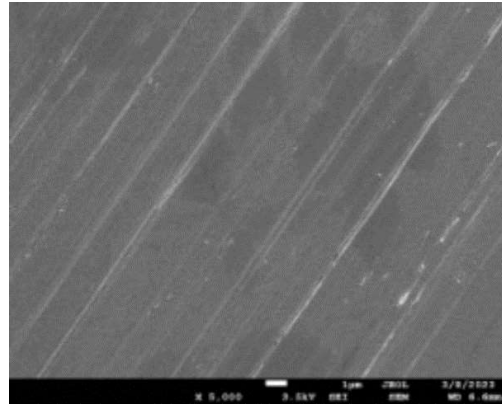


Fig. I.1 FESEM image of the surface of the copper tape.

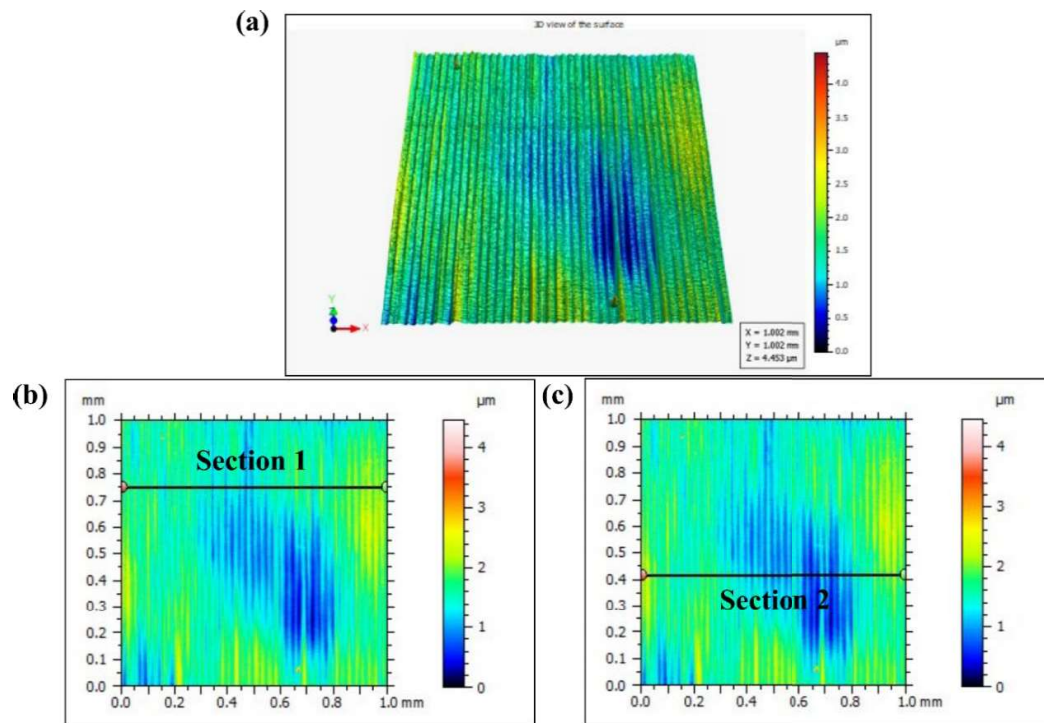


Fig. I.2 (a) 3D image of copper tape surface, (b) 2D image of copper tape surface with measurement of roughness at section 1, and (c) 2D image of copper tape surface with measurement of roughness at section 2.

**Table I.2:** The surface roughness value (Ra) (arithmetical mean deviation of absolute height) at section 1 and section 2

| Amplitude parameters | Value ( $\mu\text{m}$ ) |              |
|----------------------|-------------------------|--------------|
|                      | At section 1            | At section 2 |
| Ra                   | 0.2001                  | 0.2149       |

## 2. $\zeta$ -potential of MNS

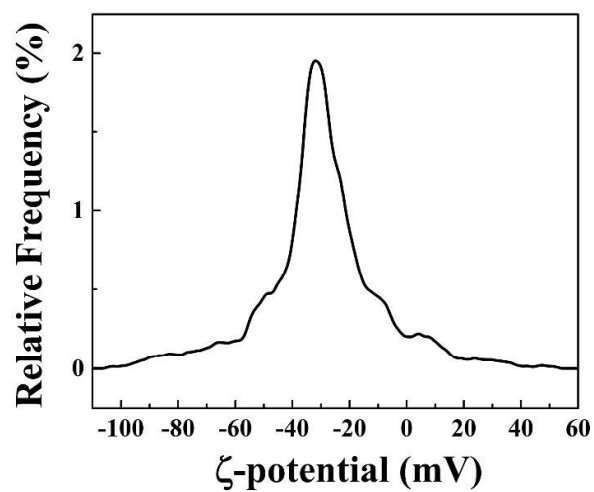


Fig. I.3  $\zeta$ -potential curve of MNS with mean  $\zeta$ -potential value of -33.4 mV.

**Table I.3** Comparison of triboelectric performance of PVDF/BWN and PVDF/MNS composite nanofabrics based TENG with reported in literature.

| <b>Polymer</b> | <b>Filler</b>  | <b>Process</b>  | <b>Voltage (V)</b> | <b>Current (<math>\mu\text{A}/\text{cm}^2</math>)</b> | <b>Power density (<math>\mu\text{W}/\text{cm}^2</math>)</b> | <b>Force (N)</b> | <b>References</b>       |
|----------------|--|-----------------|--------------------|---|---|------------------|-------------------------|
| PVDF           | AgNW (3 wt%)   | Electrospinning | 240                | 3   | -   | 5                | (Cheon et al. 2018)     |
| PVDF           | GQD (5 Vol%)   | Electrospinning | ~75                | ~0.05   | 2.7   | -                | (Choi et al. 2019)      |
| PVDF           | Fullerene (C <sub>60</sub> ) (0.2 mg)                    | Electrospinning | ~80                | ~2  | 70.5  | -                | (Sim et al. 2022)       |
| PVDF           | Fe <sub>3</sub> O <sub>4</sub> nanoparticles (11.34 wt%) | Electrospinning | 138                | ~0.18   | -   | -                | (Im and Park 2018)      |
| PVDF           | Dopamine treated SnO <sub>2</sub> (0.6 wt%)              | Electrospinning | 60                 | 0.38  | 81  | 4.5              | (Paranjape et al. 2022) |

|             |   |                        |            |          |            |                          |                    |
|-------------|---|------------------------|------------|----------|------------|--------------------------|--------------------|
| PVDF        | BTO(11.25 wt%)                              | Doctor-blade           | 131        | 1.025    | -          | 12                       | (Kang et al. 2020) |
| PVDF        | Ti <sub>0.87</sub> O <sub>2</sub> (1.5 wt%) | Solution casting       | 52.8       | 5.7      | -          | -                        | (Wen et al. 2018)  |
| PVDF        | Graphene nanosheets                         | Electrospinning        | 1511       | 18.9     | 13020      | 50                       | (Shi et al. 2021)  |
| <b>PVDF</b> | <b>MNS</b>                                  | <b>Electrospinning</b> | <b>163</b> | <b>-</b> | <b>585</b> | <b>Finger tapping</b>    | <b>This work</b>   |
|             |   |                        |            |          |            | (~avg 3.8 N)             |                    |
| <b>PVDF</b> | <b>BWN</b>                                  | <b>Electrospinning</b> | <b>200</b> | <b>-</b> | <b>646</b> | <b>Finger tapping</b>    | <b>This work</b>   |
|             |   |                        |            |          |            | (~avg 3.8 N@ 4.5±0.5 Hz) |                    |



## REFERENCES

---

- Abbasipour, M., Khajavi, R., Yousefi, A. A., Yazdanshenas, M. E., and Razaghian, F. (2017). "The piezoelectric response of electrospun PVDF nanofibers with graphene oxide, graphene, and halloysite nanofillers: a comparative study." *J. Mater. Sci. Mater. Electron.*, 28(21), 15942–15952.
- Ahn, Y., Lim, J. Y., Hong, S. M., Lee, J., Ha, J., Choi, H. J., and Seo, Y. (2013). "Enhanced piezoelectric properties of electrospun poly(vinylidene fluoride)/multiwalled carbon nanotube composites due to high  $\beta$ -phase formation in poly(vinylidene fluoride)." *J. Phys. Chem. C*, 117(22), 11791–11799.
- AlAhzm, A. M., Alejli, M. O., Ponnamma, D., Elgawady, Y., and Al-Maadeed, M. A. A. (2021). "Piezoelectric properties of zinc oxide/iron oxide filled polyvinylidene fluoride nanocomposite fibers." *J. Mater. Sci. Mater. Electron.*, 32(11), 14610–14622.
- Andrady, A. L. (2009). "Introduction, Science and Technology of Polymer Nanofibers." *SCIENCE AND TECHNOLOGY OF POLYMER NANOFIBERS*, Hoboken, New Jersey: John Wiley & Sons, Inc., 1-26.
- Andrew, J. S., and Clarke, D. R. (2008). "Enhanced ferroelectric phase content of polyvinylidene difluoride fibers with the addition of magnetic nanoparticles." *Langmuir*, 24(3), 670–672.
- Angamma, C. J., and Jayaram, S. H. (2011). "Analysis of the effects of solution conductivity on electrospinning process and fiber morphology." *IEEE Trans. Ind. Appl.*, 47(3), 1109–1117.
- Atif, R., Khaliq, J., Combrinck, M., Hassanin, A. H., Shehata, N., Elnabawy, E., and Shyha, I. (2020). "Solution blow spinning of polyvinylidene fluoride based fibers for energy harvesting applications: A review." *Polymers*, 12(6), 1–29.
- Bafqi, M. S. S., Bagherzadeh, R., Latifi, M., Sorayani Bafqi, M. S., Bagherzadeh, R., and Latifi, M. (2015). "Fabrication of composite PVDF-ZnO nanofiber mats by electrospinning for energy scavenging application with enhanced efficiency." *J. Polym.*

*Res.*, 22(130), 130.

Bairagi, S., and Ali, S. W. (2020). “Investigating the role of carbon nanotubes (CNTs) in the piezoelectric performance of a PVDF/KNN-based electrospun nanogenerator.” *Soft Matter*, 16(20), 4876–4886.

Baytekin, B., Baytekin, H. T., and Grzybowski, B. A. (2012). “What really drives chemical reactions on contact charged surfaces?” *J. Am. Chem. Soc.*, 134(17), 7223–7226.

Baytekin, H. T., Patashinski, A. Z., Branicki, M., Baytekin, B., Soh, S., and Grzybowski, B. A. (2011). “The mosaic of surface charge in contact electrification.” *Science* (80), 333(6040), 308–312.

Beachley, V., and Wen, X. (2009). “Effect of electrospinning parameters on the nano fiber diameter and length.” *Mater. Sci. Eng. C*, 29(3), 663–668.

Bharath, R. S., Chakraborty, T., Nhalil, H., Masin, B., Ashok, K., Sreemoolanadhan, H., Oommen, C., and Elizabeth, S. (2019). “Synthesis and evaluation of PVDF–MgTiO<sub>3</sub> polymer–ceramic composites for low-k dielectric applications.” *J. Mater. Chem. C*, 7(15), 4484–4496.

Bhatta, T., Maharjan, P., Cho, H., Park, C., Yoon, S. H., Sharma, S., Salauddin, M., Rahman, M. T., Rana, S. S., and Park, J. Y. (2021). “High-performance triboelectric nanogenerator based on MXene functionalized polyvinylidene fluoride composite nanofibers.” *Nano Energy*, 81(March 2021), 105670.

Cai, X., Lei, T., Sun, D., and Lin, L. (2017). “A critical analysis of the  $\alpha$ ,  $\beta$  and  $\gamma$  phases in poly(vinylidene fluoride) using FTIR.” *RSC Adv.*, 7(25), 15382–15389.

Caliò, R., Rongala, U. B., Camboni, D., Milazzo, M., Stefanini, C., Petris, G. De, and Oddo, C. M. (2014). “Piezoelectric Energy Harvesting Solutions.” *Sensors*, 14(3), 4755–4790.

Cardoso, V. F., Minas, G., Costa, C. M., Tavares, C. J., and Lanceros-Mendez, S. (2011). “Micro and nanofilms of poly(vinylidene fluoride) with controlled thickness,

morphology and electroactive crystalline phase for sensor and actuator applications.” *Smart Mater. Struct.*, 20(8), 087002.

Chandran, A. M., Varun, S., and Mural, P. K. S. (2021). “Flexible electroactive PVDF/ZnO nanocomposite with high output power and current density.” *Polym. Eng. Sci.*, 61(6), 1829–1841.

Chanmal, C. V., and Jog, J. P. (2011). “Electrospun PVDF/BaTiO<sub>3</sub> nanocomposites: Polymorphism and thermal emissivity studies.” *Int. J. Plast. Technol.*, 15(1), 1–9.

Chen, B., Yang, Y., and Wang, Z. L. (2018). “Scavenging Wind Energy by Triboelectric Nanogenerators.” *Adv. Energy Mater.*, 8(10), 1702649.

Chen, C., Bai, Z., Cao, Y., Dong, M., Jiang, K., Zhou, Y., Tao, Y., Gu, S., Xu, J., Yin, X., and Xu, W. (2020). “Enhanced piezoelectric performance of BiCl<sub>3</sub>/PVDF nanofibers-based nanogenerators.” *Compos. Sci. Technol.*, 192, 108100.

Chen, J., Guo, H., He, X., Liu, G., Xi, Y., Shi, H., and Hu, C. (2016a). “Enhancing Performance of Triboelectric Nanogenerator by Filling High Dielectric Nanoparticles into Sponge PDMS Film.” *ACS Appl. Mater. Interfaces*, 8(1), 736–744.

Chen, J., and Wang, Z. L. (2017). “Reviving Vibration Energy Harvesting and Self-Powered Sensing by a Triboelectric Nanogenerator.” *Joule*, 1(3), 480–521.

Chen, S., Zhuo, B., and Guo, X. (2016b). “Large Area One-Step Facile Processing of Microstructured Elastomeric Dielectric Film for High Sensitivity and Durable Sensing over Wide Pressure Range.” *ACS Appl. Mater. Interfaces*, 8(31), 20364–20370.

Chen, W., and Yan, X. (2020). “Progress in achieving high-performance piezoresistive and capacitive flexible pressure sensors: A review.” *J. Mater. Sci. Technol.*, 43, 175–188.

Chen, Z., Cao, Y., Yang, W., An, L., Fan, H., and Guo, Y. (2022). “Embedding in-plane aligned MOF nanoflakes in silk fibroin for highly enhanced output performance of triboelectric nanogenerators.” *J. Mater. Chem. A*, 10(2), 799–807.

Cheng, G. G., Jiang, S. Y., Li, K., Zhang, Z. Q., Wang, Y., Yuan, N. Y., Ding, J. N.,

and Zhang, W. (2017). “Effect of argon plasma treatment on the output performance of triboelectric nanogenerator.” *Appl. Surf. Sci.*, 412, 350–356.

Cheon, S., Kang, H., Kim, H., Son, Y., Lee, J. Y., Shin, H. J., Kim, S. W., and Cho, J. H. (2018). “High-Performance Triboelectric Nanogenerators Based on Electrospun Polyvinylidene Fluoride–Silver Nanowire Composite Nanofibers.” *Adv. Funct. Mater.*, 28(2), 1703778.

Chilabi, H. J., Salleh, H., Supeni, E. E., As’array, A. B., Md Rezali, K. A., and Atrah, A. B. (2020). “Harvesting energy from planetary gear using piezoelectric material.” *Energies*, 13(1), 223.

Cho, S., Yun, Y., Jang, S., Ra, Y., Choi, J. H., Hwang, H. J., Choi, D., and Choi, D. (2020). “Universal biomechanical energy harvesting from joint movements using a direction-switchable triboelectric nanogenerator.” *Nano Energy*, 71, 104584.

Choi, G. J., Baek, S. H., Lee, S. S., Khan, F., Kim, J. H., and Park, I. K. (2019). “Performance enhancement of triboelectric nanogenerators based on polyvinylidene fluoride/graphene quantum dot composite nanofibers.” *J. Alloys Compd.*, 797, 945–951.

Dani, S. S., Tripathy, A., Alluri, N. R., Balasubramaniam, S., and Ramadoss, A. (2022). “A critical review: the impact of electrical poling on the longitudinal piezoelectric strain coefficient.” *Mater. Adv.*, 3(24), 8886–8921.

Dash, S., Choudhary, R. N. P., and Goswami, M. N. (2017). “Enhanced dielectric and ferroelectric properties of PVDF-BiFeO<sub>3</sub> composites in 0–3 connectivity.” *J. Alloys Compd.*, 715, 29–36.

Dash, S., Choudhary, R. N. P., Kumar, A., and Goswami, M. N. (2019). “Enhanced dielectric properties and theoretical modeling of PVDF–ceramic composites.” *J. Mater. Sci. Mater. Electron.*, 30(21), 19309–19318.

Dhakras, D., Borkar, V., Ogale, S., and Jog, J. (2012). “Enhanced piezoresponse of electrospun PVDF mats with a touch of nickel chloride hexahydrate salt.” *Nanoscale*, 4(3), 752–756.

Dong, K., Hu, Y., Yang, J., Kim, S. W., Hu, W., and Wang, Z. L. (2021). “Smart textile triboelectric nanogenerators: Current status and perspectives.” *MRS Bull.*, 46(6), 512–521.

Dutta, B., Kar, E., Bose, N., and Mukherjee, S. (2015). “Significant enhancement of the electroactive  $\beta$ -phase of PVDF by incorporating hydrothermally synthesized copper oxide nanoparticles.” *RSC Adv.*, 5(127), 105422–105434.

Ekbote, G. S., Khalifa, M., Mahendran, A., and Anandhan, S. (2021). “Cationic surfactant assisted enhancement of dielectric and piezoelectric properties of PVDF nanofibers for energy harvesting application.” *Soft Matter*, 17(8), 2215–2222.

Ekbote, G. S., Khalifa, M., Venkatesa Perumal, B., and Anandhan, S. (2023). “Development of a flexible piezoelectric and triboelectric energy harvester with piezo capacitive sensing ability from barium tungstate nanorod-dispersed PVDF nanofabrics.” *Flex. Print. Electron.*, 8(2), 025011.

Emamian, S., Avuthu, S. G. R., Narakathu, B. B., Eshkeiti, A., Chlahawi, A. A., Bazuin, B. J., Joyce, M. K., and Atashbar, M. Z. (2015). “Fully printed and flexible piezoelectric based touch sensitive skin.” *2015 IEEE SENSORS*, Busan, Korea (South): IEEE, 1–4.

Esterly, D. M., and Love, B. J. (2004). “Phase Transformation to  $\beta$ -Poly ( vinylidene fluoride ) by Milling.” *J. Polym. Sci. Part B Polym. Phys.*, 42(1), 91–97.

Fan, F. R., Lin, L., Zhu, G., Wu, W., Zhang, R., and Wang, Z. L. (2012a). “Transparent triboelectric nanogenerators and self-powered pressure sensors based on micropatterned plastic films.” *Nano Lett.*, 12(6), 3109–3114.

Fan, F. R., Tang, W., and Wang, Z. L. (2016). “Flexible Nanogenerators for Energy Harvesting and Self-Powered Electronics.” *Adv. Mater.*, 28(22), 4283–4305.

Fan, F. R., Tian, Z. Q., and Wang, Z. L. (2012b). “Flexible triboelectric generator.” *Nano Energy*, 1(2), 328–334.

Fan, Y., Wu, K., and Cheng, C. (2019). “The conductivity characteristics of different

oils and papers and their effects on the interface charge of oil- paper.” *IEEE Conf. Electr. Insul. Dielectr. Phenom.*, Richland, WA, USA: IEEE, 785–788.

Fatma, B., Gupta, S., Chatterjee, C., Bhunia, R., Verma, V., and Garg, A. (2020). “Triboelectric generators made of mechanically robust PVDF films as self-powered autonomous sensors for wireless transmission based remote security systems.” *J. Mater. Chem. A*, 8(30), 15023–15033.

Feng, Y., Zheng, Y., Rahman, Z. U., Wang, D., Zhou, F., and Liu, W. (2016). “Paper-based triboelectric nanogenerators and their application in self-powered anticorrosion and antifouling.” *J. Mater. Chem. A*, 4(46), 18022–18030.

Fong, H., Chun, I., and Reneker, D. H. (1999). “Beaded nanofibers formed during electrospinning.” *Polymer*, 40(16), 4585–4592.

Fu, R., Chen, S., Lin, Y., Zhang, S., Jiang, J., Li, Q., and Gu, Y. (2017). “Improved piezoelectric properties of electrospun poly(vinylidene fluoride) fibers blended with cellulose nanocrystals.” *Mater. Lett.*, 187, 86–88.

Gonçalves, R., Martins, P., Moya, X., Ghidini, M., Sencadas, V., Botelho, G., Mathur, N. D., and Lanceros-Mendez, S. (2015). “Magnetoelectric CoFe<sub>2</sub>O<sub>4</sub>/polyvinylidene fluoride electrospun nanofibres.” *Nanoscale*, 7(17), 8058–8061.

Govinna, N., Sadeghi, I., Asatekin, A., and Cebe, P. (2019). “Thermal properties and structure of electrospun blends of PVDF with a fluorinated copolymer.” *J. Polym. Sci. Part B Polym. Phys.*, 57(6), 312–322.

Gregorio JR., R., and Capitão, R. C. (2000). “Morphology and phase transition of high melt temperature crystallized poly(vinylidene fluoride).” *J. Mater. Sci.*, 35(2), 299–306.

Gregorio, R., and Cestari, M. (1994). “Effect of crystallization temperature on the crystalline phase content and morphology of poly(vinylidene fluoride).” *J. Polym. Sci. Part B Polym. Phys.*, 32(5), 859–870.

Han, M., Li, Z., Sun, X., and Zhang, H. (2014). “Analysis of an in-plane

electromagnetic energy harvester with integrated magnet array.” *Sensors Actuators, A Phys.*, 219, 38–46.

Harstad, S. M., Zhao, P., Soin, N., El-Gendy, A. A., Gupta, S., Pecharsky, V. K., Luo, J., and Hadimani, R. L. (2019). “Gd<sub>5</sub>Si<sub>4</sub>-PVDF nanocomposite films and their potential for triboelectric energy harvesting applications.” *AIP Adv.*, 9(3), 035116.

He, X., Guo, H., Yue, X., Gao, J., Xi, Y., and Hu, C. (2015). “Improving energy conversion efficiency for triboelectric nanogenerator with capacitor structure by maximizing surface charge density.” *Nanoscale*, 7(5), 1896–1903.

He, X., and Yao, K. (2006). “Crystallization mechanism and piezoelectric properties of solution-derived ferroelectric poly(vinylidene fluoride) thin films.” *Appl. Phys. Lett.*, 89(11), 112909.

Hedau, B., Kang, B. C., and Ha, T. J. (2022). “Enhanced Triboelectric Effects of Self-Poled MoS<sub>2</sub>-Embedded PVDF Hybrid Nanocomposite Films for Bar-Printed Wearable Triboelectric Nanogenerators.” *ACS Nano*, 16(11), 18355–18365.

Hosseini, S. M., and Yousefi, A. A. (2017). “Electrospun PVDF/MWCNT/OMMT hybrid nanocomposites: preparation and characterization.” *Iran. Polym. J.*, 26(5), 331–339.

Hu, G., Gao, F., Kong, J., Yang, S., Zhang, Q., Liu, Z., Zhang, Y., and Sun, H. (2015). “Preparation and dielectric properties of poly(vinylidene fluoride)/Ba<sub>0.6</sub>Sr<sub>0.4</sub>TiO<sub>3</sub> composites.” *J. Alloys Compd.*, 619, 686–692.

Hu, Y., Yang, J., Niu, S., Wu, W., and Wang, Z. L. (2014). “Hybridizing triboelectrification and electromagnetic induction effects for high-efficient mechanical energy harvesting.” *ACS Nano*, 8(7), 7442–7450.

Huang, S., Yee, W. A., Tjiu, W. C., Liu, Y., Kotaki, M., Yin, C., Boey, Y. C. F., Ma, J., Liu, T., and Lu, X. (2008). “Electrospinning of Polyvinylidene Difluoride with Carbon Nanotubes : Synergistic Effects of Extensional Force and Interfacial Interaction on Crystalline Structures.” *Langmuir*, 24(23), 13621–13626.

Hussein, A. D., Sabry, R. S., Abdul Azeez Dakhil, O., and Bagherzadeh, R. (2019). "Effect of Adding BaTiO<sub>3</sub> to PVDF as Nano Generator." *J. Phys. Conf. Ser.*, IOP Publishing Ltd, 022012.

Ico, G., Showalter, A., Bosze, W., Gott, S. C., Kim, B. S., Rao, M. P., Myung, N. V., and Nam, J. (2016). "Size-dependent piezoelectric and mechanical properties of electrospun P(VDF-TrFE) nanofibers for enhanced energy harvesting." *J. Mater. Chem. A*, 4(6), 2293–2304.

Im, J. S., and Park, I. K. (2018). "Mechanically Robust Magnetic Fe<sub>3</sub>O<sub>4</sub> Nanoparticle/Polyvinylidene Fluoride Composite Nanofiber and Its Application in a Triboelectric Nanogenerator." *ACS Appl. Mater. Interfaces*, 10(30), 25660–25665.

Ince-Gunduz, B. S., Alpern, R., Amare, D., Crawford, J., Dolan, B., Jones, S., Kobylarz, R., Reveley, M., and Cebe, P. (2010). "Impact of nanosilicates on poly(vinylidene fluoride) crystal polymorphism: Part 1. Melt-crystallization at high supercooling." *Polymer*, 51(6), 1485–1493.

Ippili, S., Jella, V., Thomas, A. M., Yoon, C., Jung, J. S., and Yoon, S. G. (2021). "ZnAl-LDH-induced electroactive  $\beta$ -phase and controlled dielectrics of PVDF for a high-performance triboelectric nanogenerator for humidity and pressure sensing applications." *J. Mater. Chem. A*, 9(29), 15993–16005.

Issa, A. A., Al-Maadeed, M. A. A. S., Mrlík, M., and Luyt, A. S. (2016). "Electrospun PVDF graphene oxide composite fibre mats with tunable physical properties." *J. Polym. Res.*, 23, 232.

Issa, A. A., Al-maadeed, M. A., Luyt, A. S., Ponnamma, D., and Hassan, M. K. (2017). "Physico-Mechanical, Dielectric, and Piezoelectric Properties of PVDF Electrospun Mats Containing Silver Nanoparticles." *C*, 3(4), 30.

Itoh, H., Li, Y., Chan, K. H. K., and Kotaki, M. (2016). "Morphology and mechanical properties of PVA nanofibers spun by free surface electrospinning." *Polym. Bull.*, 73(10), 2761–2777.

Jahan, N., Mighri, F., Rodrigue, D., and Ajji, A. (2017). "Enhanced electroactive  $\beta$

phase in three phase PVDF/CaCO<sub>3</sub>/nanoclay composites: Effect of micro-CaCO<sub>3</sub> and uniaxial stretching.” *J. Appl. Polym. Sci.*, 134(24), 44940.

Jiang, J., Tu, S., Fu, R., Li, J., Hu, F., Yan, B., Gu, Y., and Chen, S. (2020). “Flexible Piezoelectric Pressure Tactile Sensor Based on Electrospun BaTiO<sub>3</sub>/Poly(vinylidene fluoride) Nanocomposite Membrane.” *ACS Appl. Mater. Interfaces*, 12(30), 33989–33998.

Jin, L., Ma, S., Deng, W., Yan, C., Yang, T., Chu, X., Tian, G., Xiong, D., Lu, J., and Yang, W. (2018). “Polarization-free high-crystallization  $\beta$ -PVDF piezoelectric nanogenerator toward self-powered 3D acceleration sensor.” *Nano Energy*, 50, 632–638.

Jong, M. De, Chen, W., Geerlings, H., Asta, M., and Persson, K. A. (2015). “A database to enable discovery and design of piezoelectric materials.” *Sci. Data*, 2, 150053.

Kalimuldina, G., Turdakyn, N., Abay, I., Medeubayev, A., Nurpeissova, A., Adair, D., and Bakenov, Z. (2020). “A review of piezoelectric pvdf film by electrospinning and its applications.” *Sensors*, 20(18), 5214.

Kang, X., Pan, C., Chen, Y., Pu, X., Kang, X., Chen, Y., Pu, X., Pan, C., and Pu, X. (2020). “Boosting performances of triboelectric nanogenerators by optimizing dielectric properties and thickness of electrification layer.” *RSC Adv.*, 10(30), 17752–17759.

Kar, E., Bose, N., Das, S., Mukherjee, N., and Mukherjee, S. (2015). “Enhancement of electroactive  $\beta$  phase crystallization and dielectric constant of PVDF by incorporating GeO<sub>2</sub> and SiO<sub>2</sub> nanoparticles.” *Phys. Chem. Chem. Phys.*, 17(35), 22784–22798.

Khalifa, M., and Anandhan, S. (2019). “PVDF Nanofibers with Embedded Polyaniline-Graphitic Carbon Nitride Nanosheet Composites for Piezoelectric Energy Conversion.” *ACS Appl. Nano Mater.*, 2(11), 7328–7339.

Khalifa, M., Mahendran, A., and Anandhan, S. (2016). “Probing the synergism of halloysite nanotubes and electrospinning on crystallinity, polymorphism and piezoelectric performance of poly(vinylidene fluoride).” *RSC Adv.*, 6(115), 114052–

114060.

Khalifa, M., Mahendran, A., and Anandhan, S. (2019). "Synergism of graphitic-carbon nitride and electrospinning on the physico-chemical characteristics and piezoelectric properties of flexible poly(vinylidene fluoride) based nanogenerator." *J. Polym. Res.*, 26(3), 73.

Khalifa, M., Schoeffmann, E., Lammer, H., Mahendran, A. R., Wuzella, G., and Anandhan, S. (2021). "A study on electroactive PVDF/mica nanosheet composites with an enhanced  $\gamma$ -phase for capacitive and piezoelectric force sensing." *Soft Matter*, 17(48), 10891–10902.

Khan, M. Y. A., Zahoor, M., Shaheen, A., Jamil, N., Arshad, M. I., Bajwa, S. Z., Shad, N. A., Butt, R., Ali, I., Iqbal, M. Z., Wu, A., Nabi, G., Hussain, S., Mahmood, T., Aslam, I., and Khan, W. S. (2018). "Visible light photocatalytic degradation of crystal violet dye and electrochemical detection of ascorbic acid & glucose using BaWO<sub>4</sub> nanorods." *Mater. Res. Bull.*, 104, 38–43.

Khan, U., and Kim, S. W. (2016). "Triboelectric Nanogenerators for Blue Energy Harvesting." *ACS Nano*, 10(7), 6429–6432.

Kim, S., Song, Y., and Heller, M. J. (2017a). "Influence of MWCNTs on  $\beta$ -Phase PVDF and Triboelectric Properties." *J. Nanomater.*, 2017, 2697382.

Kim, W. G., Kim, D. W., Tcho, I. W., Kim, J. K., Kim, M. S., and Choi, Y. K. (2021). "Triboelectric Nanogenerator: Structure, Mechanism, and Applications." *ACS Nano*, 15(1), 258–287.

Kim, Y. J., Lee, J., Park, S., Park, C., Park, C., and Choi, H. J. (2017b). "Effect of the relative permittivity of oxides on the performance of triboelectric nanogenerators." *RSC Adv.*, 7(78), 49368–49373.

Kim, Y., Wu, X., and Oh, J. H. (2020). "Fabrication of triboelectric nanogenerators based on electrospun polyimide nanofibers membrane." *Sci. Rep.*, 10, 2742.

Knorr, N. (2011). "Squeezing out hydrated protons: Low-frictional-energy triboelectric

insulator charging on a microscopic scale.” *AIP Adv.*, 1(2), 022119.

Korkmaz, S., and Kariper, I. A. (2022). “BaTiO<sub>3</sub>-based nanogenerators: fundamentals and current status.” *J. Electroceramics*, 48(1), 8–34.

Kumar, R. S., Sarathi, T., Venkataraman, K. K., and Bhattacharyya, A. (2019). “Enhanced piezoelectric properties of polyvinylidene fluoride nanofibers using carbon nanofiber and electrical poling.” *Mater. Lett.*, 255, 126515.

Kwon, D., Lee, T. I., Kim, M. S., Kim, S., Kim, T. S., and Park, I. (2015). “Porous dielectric elastomer based ultra-sensitive capacitive pressure sensor and its application to wearable sensing device.” *2015 Transducers - 2015 18th Int. Conf. Solid-State Sensors, Actuators Microsystems, TRANSDUCERS 2015*, Anchorage, AK, USA: IEEE, 299–302.

Kwon, D., Lee, T. I., Shim, J., Ryu, S., Kim, M. S., Kim, S., Kim, T. S., and Park, I. (2016). “Highly Sensitive, Flexible, and Wearable Pressure Sensor Based on a Giant Piezocapacitive Effect of Three-Dimensional Microporous Elastomeric Dielectric Layer.” *ACS Appl. Mater. Interfaces*, 8(26), 16922–16931.

Li, H., Tian, C., and Deng, Z. D. (2014). “Energy harvesting from low frequency applications using piezoelectric materials.” *Appl. Phys. Rev.*, 1(4), 041301.

Li, H., Wu, T., Xie, M., Shi, Y., Shen, S., Zhao, M., Yang, X., Figueroa-Cosme, L. M., Ke, Q., and Xia, Y. (2018). “Enhancing the tactile and near-infrared sensing capabilities of electrospun PVDF nanofibers with the use of gold nanocages.” *J. Mater. Chem. C*, 6(38), 10263–10269.

Li, J., Chen, S., Liu, W., Fu, R., Tu, S., Zhao, Y., Dong, L., Yan, B., and Gu, Y. (2019). “High Performance Piezoelectric Nanogenerators Based on Electrospun ZnO Nanorods/Poly(vinylidene fluoride) Composite Membranes.” *J. Phys. Chem. C*, 123(18), 11378–11387.

Li, R., Zhou, Q., Bi, Y., Cao, S., Xia, X., Yang, A., Li, S., and Xiao, X. (2021). “Research progress of flexible capacitive pressure sensor for sensitivity enhancement approaches.” *Sensors Actuators, A Phys.*, 321, 112425.

- Liang, C. L., Mai, Z. H., Xie, Q., Bao, R. Y., Yang, W., Xie, B. H., and Yang, M. B. (2014a). "Induced Formation of Dominating Polar Phases of Poly(vinylidene fluoride): Positive Ion–CF<sub>2</sub> Dipole or Negative Ion–CH<sub>2</sub> Dipole Interaction." *J. Phys. Chem. B*, 118(30), 9104–9111.
- Liang, C. L., Xie, Q., Bao, R. Y., Yang, W., Xie, B. H., and Yang, M. B. (2014b). "Induced formation of polar phases in poly(vinylidene fluoride) by cetyl trimethyl ammonium bromide." *J. Mater. Sci.*, 49(12), 4171–4179.
- Lin, L., Xie, Y., Wang, S., Wu, W., Niu, S., Wen, X., and Wang, Z. L. (2013). "Trielectroactive sensor array for self-powered static and dynamic pressure detection and tactile imaging." *ACS Nano*, 7(9), 8266–8274.
- Lin, Y., Xu, Z., Yu, D., Lu, L., Yin, M., Tavakoli, M. M., Chen, X., Hao, Y., Fan, Z., Cui, Y., and Li, D. (2016). "Dual-Layer Nanostructured Flexible Thin-Film Amorphous Silicon Solar Cells with Enhanced Light Harvesting and Photoelectric Conversion Efficiency." *ACS Appl. Mater. Interfaces*, 8(17), 10929–10936.
- Liu, J., Lu, X., and Wu, C. (2013). "Effect of preparation methods on crystallization behavior and tensile strength of poly(vinylidene fluoride) membranes." *Membranes*, 3(4), 389–405.
- Liu, J., Yu, D., Zheng, Z., Huangfu, G., and Guo, Y. (2021a). "Lead-free BiFeO<sub>3</sub> film on glass fiber fabric: Wearable hybrid piezoelectric-triboelectric nanogenerator." *Ceram. Int.*, 47(3), 3573–3579.
- Liu, P., Sun, N., Mi, Y., Luo, X., Dong, X., Cai, J., Jia, X., Ramos, M. A., Hu, T. S., and Xu, Q. (2021b). "Ultra-low CNTs filled high-performance fast self-healing triboelectric nanogenerators for wearable electronics." *Compos. Sci. Technol.*, 208, 108733.
- Liu, Y., and Jiayan, Y. (1998). "Studies on uniaxially drawn poly (vinylidene fluoride) films." *J. Polym. Eng.*, 18(4), 275–282.
- Lovinger, A. J., Laboratories, H., and Hill, M. (1980). "Crystallization and Morphology of Melt-Solidified Poly (vinylidene Fluoride)." 18, 793–809.

- Lu, H., Liu, L., Lin, J., Yang, W., Weng, L., Zhang, X., Chen, G., and Huang, W. (2017). "Polarization and space charge performance in PVDF with MPB composition BCZT doped composite films." *J. Appl. Polym. Sci.*, 134(40), 45362.
- Lund, H. (2007). "Renewable energy strategies for sustainable development." *Energy*, 32(6), 912–919.
- Luo, J., and Wang, Z. L. (2020). "Recent progress of triboelectric nanogenerators: From fundamental theory to practical applications." *EcoMat*, 2(4), 12059.
- Luo, Y., Shao, J., Chen, S., Chen, X., Tian, H., Li, X., Wang, L., Wang, D., and Lu, B. (2019). "Flexible Capacitive Pressure Sensor Enhanced by Tilted Micropillar Arrays." *ACS Appl. Mater. Interfaces*, 11(19), 17796–17803.
- Ma, L., Shuai, X., Hu, Y., Liang, X., Zhu, P., Sun, R., and Wong, C. P. (2018). "A highly sensitive and flexible capacitive pressure sensor based on a micro-arrayed polydimethylsiloxane dielectric layer." *J. Mater. Chem. C*, 6(48), 13232–13240.
- Ma, W., Zhang, J., Chen, S., and Wang, X. (2008). "Crystalline phase formation of poly(vinylidene fluoride) from tetrahydrofuran/N,N-dimethylformamide mixed solutions." *J. Macromol. Sci. Part B Phys.*, 47(3), 434–449.
- Mahdavi Varposhti, A., Yousefzadeh, M., Kowsari, E., and Latifi, M. (2020). "Enhancement of  $\beta$ -Phase Crystalline Structure and Piezoelectric Properties of Flexible PVDF/Ionic Liquid Surfactant Composite Nanofibers for Potential Application in Sensing and Self-Powering." *Macromol. Mater. Eng.*, 305(3), 1900796.
- Mannsfeld, S. C. B., Tee, B. C. K., Stoltenberg, R. M., Chen, C. V. H. H., Barman, S., Muir, B. V. O., Sokolov, A. N., Reese, C., and Bao, Z. (2010). "Highly sensitive flexible pressure sensors with microstructured rubber dielectric layers." *Nat. Mater.*, 9(10), 859–864.
- Martins, P., Costa, C. M., Benelmekki, M., Botelho, G., and Lanceros-Mendez, S. (2012). "On the origin of the electroactive poly(vinylidene fluoride)  $\beta$ -phase nucleation by ferrite nanoparticles via surface electrostatic interactions." *CrystEngComm*, 14(8), 2807–2811.

Martins, P., Lopes, A. C., and Lanceros-Mendez, S. (2014). "Electroactive phases of poly(vinylidene fluoride): Determination, processing and applications." *Prog. Polym. Sci.*, 39(4), 683–706.

Mason, W. P. (1981). "Piezoelectricity , its history and applications." *J. Acoust. Soc. Am.*, 70, 1561.

McCarty, L. S., and Whitesides, G. M. (2008). "Electrostatic charging due to separation of ions at interfaces: Contact electrification of ionic electrets." *Angew. Chemie- Int. Ed.*, 47(12), 2188–2207.

Mishra, S., Unnikrishnan, L., Nayak, S. K., and Mohanty, S. (2019). "Advances in Piezoelectric Polymer Composites for Energy Harvesting Applications: A Systematic Review." *Macromol. Mater. Eng.*, 304(1), 1800463.

Moghadam, B. H., Hasanzadeh, M., and Simchi, A. (2020). "Self-Powered Wearable Piezoelectric Sensors Based on Polymer Nanofiber – Metal – Organic Framework Nanoparticle Composites for Arterial Pulse Monitoring." *ACS Appl. Nano Mater.*, 3(9), 8742–8752.

Mokhtari, F., Shamshirsaz, M., Latifi, M., and Asadi, S. (2017). "Comparative evaluation of piezoelectric response of electrospun PVDF (polyvinylidene fluoride) nanofiber with various additives for energy scavenging application." *J. Text. Inst.*, 108(6), 906–914.

Mokhtari, F., Shamshirsaz, M., Latifi, M., and Foroughi, J. (2020). "Nanofibers-based piezoelectric energy harvester for self-powered wearable technologies." *Polymers*, 12(11), 2697.

Momma, K., and Izumi, F. (2011). "VESTA 3 for three-dimensional visualization of crystal, volumetric and morphology data." *J. Appl. Crystallogr.*, 44(6), 1272–1276.

Niu, S., and Wang, Z. L. (2014). "Theoretical systems of triboelectric nanogenerators." *Nano Energy*, 14, 161–192.

Parandeh, S., Kharaziha, M., and Karimzadeh, F. (2019). "An eco-friendly triboelectric

hybrid nanogenerators based on graphene oxide incorporated polycaprolactone fibers and cellulose paper.” *Nano Energy*, 59, 412–421.

Parangusan, H., Ponnamma, D., and Almaadeed, M. A. A. (2019). “Toward High Power Generating Piezoelectric Nano fibers : Influence of Particle Size and Surface Electrostatic Interaction of Ce – Fe<sub>2</sub>O<sub>3</sub> and Ce – Co<sub>3</sub>O<sub>4</sub> on PVDF.” *ACS Omega*, 4(4), 6312–6323.

Paranjape, M. V., Graham, S. A., Patnam, H., Manchi, P., and Yu, J. S. (2022). “Dopamine treated SnO<sub>2</sub>/PVDF composite films for hybrid mechanical energy harvester.” *Compos. Sci. Technol.*, 221, 109323.

Patil, P. N., Subramanian, U., and Hyam, R. S. (2021). “Enhanced electrical and thermoelectric power properties of BaWO<sub>4</sub>/CaWO<sub>4</sub> nanocomposites.” *Appl. Phys. A Mater. Sci. Process.*, 127(9), 731.

Pramoda, K. P., Mohamed, A., Phang, I. Y., and Liu, T. (2005). “Crystal transformation and thermomechanical properties of poly(vinylidene fluoride)/clay nanocomposites.” *Polym. Int.*, 54(1), 226–232.

Prateek, Thakur, V. K., and Gupta, R. K. (2016). “Recent Progress on Ferroelectric Polymer-Based Nanocomposites for High Energy Density Capacitors: Synthesis, Dielectric Properties, and Future Aspects.” *Chem. Rev.*, 116(7), 4260–4317.

Qi, Y., and Mcalpine, M. C. (2010). “Nanotechnology-enabled flexible and biocompatible energy harvesting.” *Energy Environ. Sci.*, 3(9), 1275–1285.

Ramadan, K. . (2014). “A review of piezoelectric polymers as functional materials for electromechanical transducers.” *Smart Mater. Struct.*, 23(3), 033001.

Ramakrishna, S., Fujihara, K., Teo, W.-E., Lim, T.-C., and Ma, Z. (2005). *An Introduction to Electrospinning and Nanofibers*. Singapore: World Scientific Publishing Co. Pte. Ltd.

Rana, A., Roberge, J. P., and Duchaine, V. (2016). “An Improved Soft Dielectric for a Highly Sensitive Capacitive Tactile Sensor.” *IEEE Sens. J.*, 16(22), 7853–7863.

Rasel, S., and Rizvi, G. (2018). "Fabrication and Characterization of Electrospun PVA/Mica Fibrous Nanocomposite Mats." *Polym. - Plast. Technol. Eng.*, 57(4), 320–326.

Roy, K., Ghosh, S. K., Sultana, A., Garain, S., Xie, M., Bowen, C. R., Henkel, K., Schmeißer, D., and Mandal, D. (2019). "A Self-Powered Wearable Pressure Sensor and Pyroelectric Breathing Sensor Based on GO Interfaced PVDF Nanofibers." *ACS Appl. Nano Mater.*, 2(4), 2013–2025.

Sadiq, M. M. J., and Nesaraj, A. S. (2015). "Soft chemical synthesis and characterization of BaWO<sub>4</sub> nanoparticles for photocatalytic removal of Rhodamine B present in water sample." *J. Nanostructure Chem.*, 5(1), 45–54.

Safaei, M., Sodano, H. A., and Anton, S. R. (2019). "A review of energy harvesting using piezoelectric materials: State-of-the-art a decade later (2008-2018)." *Smart Mater. Struct.*, 28(11), 113001.

Sajkiewicz, P., Wasiak, A., and Gocłowski, Z. (1999). "Phase transitions during stretching of poly(vinylidene fluoride)." *Eur. Polym. J.*, 35(3), 423–429.

Sakaguchi, M., Makino, M., Ohura, T., and Iwata, T. (2014). "Contact electrification of polymers due to electron transfer among mechano anions, mechano cations and mechano radicals." *J. Electrostat.*, 72(5), 412–416.

Salimi, A., and Yousefi, A. A. (2004). "Conformational changes and phase transformation mechanisms in PVDF solution-cast films." *J. Polym. Sci. Part B Polym. Phys.*, 42(18), 3487–3495.

Sarkar, S., Garain, S., Mandal, D., and Chattopadhyay, K. K. (2014). "Electro-active phase formation in PVDF–BiVO<sub>4</sub> flexible nanocomposite films for high energy density storage application." *RSC Adv.*, 4(89), 48220–48227.

Satthiyaraju, M., and Ramesh, T. (2019a). "Effect of annealing treatment on PVDF nanofibers for mechanical energy harvesting applications." *Mater. Res. Express*, 6(10), 105366.

- Sathiyaraju, M., and Ramesh, T. (2019b). “Nanomechanical , Mechanical Responses and Characterization of Piezoelectric Nanoparticle-Modified Electrospun PVDF Nanofibrous Films.” *Arab. J. Sci. Eng.*, 44(6), 5697–5709.
- Schneider, C. A., Rasband, W. S., and Eliceiri, K. W. (2012). “NIH Image to ImageJ: 25 years of image analysis.” *Nat. Methods*, 9(7), 671–675.
- Sencadas, V., Gregorio, R., and Lanceros-Méndez, S. (2009). “ $\alpha$  to  $\beta$  phase transformation and microstructural changes of PVDF films induced by uniaxial stretch.” *J. Macromol. Sci. Part B Phys.*, 48(3), 514–525.
- Shamitha, C., Mahendran, A., and Anandhan, S. (2020). “Effect of polarization switching on piezoelectric and dielectric performance of electrospun nanofabrics of poly(vinylidene fluoride)/Ca–Al LDH nanocomposite.” *J. Appl. Polym. Sci.*, 137(20), 48697.
- Sharafkhani, S., and Kokabi, M. (2018). “Tailoring favor crystalline structure via electrospun PVDF/BaTiO<sub>3</sub> nanofibers.” *6TH Int. Bienn. Conf. ULTRAFINE GRAINED NANOSTRUCTURED Mater.*, Kish Island, Iran: AIP Publishing, 020001.
- Sharma, M., Madras, G., and Bose, S. (2015). “Contrasting Effects of Graphene Oxide and Poly(ethylenimine) on the Polymorphism in Poly(vinylidene fluoride).” *Cryst. Growth Des.*, 15(7), 3345–3355.
- Sharma, M., Srinivas, V., Madras, G., and Bose, S. (2016). “Outstanding dielectric constant and piezoelectric coefficient in electrospun nanofiber mats of PVDF containing silver decorated multiwall carbon nanotubes: Assessing through piezoresponse force microscopy.” *RSC Adv.*, 6(8), 6251–6258.
- Shetty, S., Ekbote, G. S., Mahendran, A., and Anandhan, S. (2019). “Polymorphism, dielectric and piezoelectric response of organo-modified Ni–Co layered double hydroxide nanosheets dispersed electrospun PVDF nanofabrics.” *J. Mater. Sci. Mater. Electron.*, 30, 20703–20715.
- Shetty, S., Mahendran, A., and Anandhan, S. (2020). “Development of a new flexible nanogenerator from electrospun nanofabric based on PVDF/talc nanosheets

composites.” *Soft Matter*, 16(24), 5679–5688.

Shetty, S., Shanmugaraj, A. M., and Anandhan, S. (2021). “Physico-chemical and piezoelectric characterization of electroactive nanofabrics based on functionalized graphene/talc nanolayers/PVDF for energy harvesting.” *J. Polym. Res.*, 28(11), 419.

Shi, L., Jin, H., Dong, S., Huang, S., Kuang, H., Xu, H., Chen, J., Xuan, W., Zhang, S., Li, S., Wang, X., and Luo, J. (2021). “High-performance triboelectric nanogenerator based on electrospun PVDF-graphene nanosheet composite nanofibers for energy harvesting.” *Nano Energy*, 80, 105599.

Shin, S. H., Bae, Y. E., Moon, H. K., Kim, J., Choi, S. H., Kim, Y., Yoon, H. J., Lee, M. H., and Nah, J. (2017). “Formation of Triboelectric Series via Atomic-Level Surface Functionalization for Triboelectric Energy Harvesting.” *ACS Nano*, 11(6), 6131–6138.

Sim, D. J., Choi, G. J., Sohn, S. H., and Park, I. K. (2022). “Electronegative polyvinylidene fluoride/C<sub>60</sub> composite nanofibers for performance enhancement of triboelectric nanogenerators.” *J. Alloys Compd.*, 898, 162805.

Singh, H. H., and Khare, N. (2019). “Improved performance of ferroelectric nanocomposite flexible film based triboelectric nanogenerator by controlling surface morphology, polarizability, and hydrophobicity.” *Energy*, 178, 765–771.

Singh, S. K., Kumar, P., Magdum, R., Khandelwal, U., Deswal, S., More, Y., Muduli, S., Boomishankar, R., Pandit, S., and Ogale, S. (2019). “Seed Power: Natural Seed and Electrospun Poly(vinyl difluoride) (PVDF) Nanofiber Based Triboelectric Nanogenerators with High Output Power Density.” *ACS Appl. Bio Mater.*, 2(8), 3164–3170.

Sohma, J. (1989). “Mechanochemistry of polymers.” *Prog. Polym. Sci.*, 14(4), 451–596.

Soin, N., Zhao, P., Prashanthi, K., Chen, J., Ding, P., Zhou, E., Shah, T., Ray, S. C., Tsonos, C., Thundat, T., Siores, E., and Luo, J. (2016). “High performance triboelectric nanogenerators based on phase-inversion piezoelectric membranes of poly(vinylidene fluoride)-zinc stannate (PVDF-ZnSnO<sub>3</sub>) and polyamide-6 (PA6).” *Nano Energy*, 30,

470–480.

Stassi, S., Cauda, V., Canavese, G., and Pirri, C. F. (2014). “Flexible tactile sensing based on piezoresistive composites: A review.” *Sensors*, 14(3), 5296–5332.

Szewczyk, P. K., Gradys, A., Kim, S. K., Persano, L., Marzec, M., Kryshstal, A., Busolo, T., Toncelli, A., Pisignano, D., Bernasik, A., Kar-Narayan, S., Sajkiewicz, P., and Stachewicz, U. (2020). “Enhanced Piezoelectricity of Electrospun Polyvinylidene Fluoride Fibers for Energy Harvesting.” *ACS Appl. Mater. Interfaces*, 12(11), 13575–13583.

Tao, X., Jin, H., Ma, M., Quan, L., Chen, J., Dong, S., Zhang, H., Lv, C., Fu, Y., and Luo, J. (2019). “Significantly Enhanced Performance of Triboelectric Nanogenerator by Incorporating BaTiO<sub>3</sub> Nanoparticles in Poly(vinylidene fluoride) Film.” *Phys. Status Solidi Appl. Mater. Sci.*, 216(7), 1900068.

Taylor, P., and Lowell, J. (1980). “Advances in Physics Contact electrification.” *Adv. Phys.*, 29(6), 947–1023.

Tayyab, M., Wang, J., Wang, J., Maksutoglu, M., Yu, H., Sun, G., Yildiz, F., Eginligil, M., and Huang, W. (2020). “Enhanced output in polyvinylidene fluoride nanofibers based triboelectric nanogenerator by using printer ink as nano-fillers.” *Nano Energy*, 77, 105178.

Tcho, I. W., Kim, W. G., Kim, J. K., Kim, D. W., Yun, S. Y., Son, J. H., and Choi, Y. K. (2022). “A flutter-driven triboelectric nanogenerator for harvesting energy of gentle breezes with a rear-fixed fluttering film.” *Nano Energy*, 98, 107197.

Thakre, A., Kumar, A., Song, H. C., Jeong, D. Y., and Ryu, J. (2019). “Pyroelectric energy conversion and its applications—flexible energy harvesters and sensors.” *Sensors*, 19(9), 2170.

Ting, Y., Suprpto, Bunekar, N., Sivasankar, K., and Aldori, Y. R. (2020). “Using annealing treatment on fabrication ionic liquid-based PVDF films.” *Coatings*, 10(1), 44.

Tiwari, S., Gaur, A., Kumar, C., and Maiti, P. (2019). “Enhanced piezoelectric response in nanoclay induced electrospun PVDF nanofibers for energy harvesting.” *Energy*, 171, 485–492.

Tsonos, C., Zois, H., Kanapitsas, A., Soin, N., Siores, E., Peppas, G. D., Pyrgioti, E. C., Sanida, A., Stavropoulos, S. G., and Psarras, G. C. (2019). “Polyvinylidene fluoride/magnetite nanocomposites: Dielectric and thermal response.” *J. Phys. Chem. Solids*, 129, 378–386.

Wan, S., Bi, H., Zhou, Y., Xie, X., Su, S., Yin, K., and Sun, L. (2017). “Graphene oxide as high-performance dielectric materials for capacitive pressure sensors.” *Carbon N. Y.*, 114, 209–216.

Wan, Y., Qiu, Z., Hong, Y., Wang, Y., Zhang, J., Liu, Q., Wu, Z., and Guo, C. F. (2018). “A Highly Sensitive Flexible Capacitive Tactile Sensor with Sparse and High-Aspect-Ratio Microstructures.” *Adv. Electron. Mater.*, 4(4), 1700586.

Wang, H., Chen, Q., Xia, W., Qiu, X., Cheng, Q., and Zhu, G. (2018). “Electroactive PVDF thin films fabricated via cooperative stretching process.” *J. Appl. Polym. Sci.*, 135(22), 46324.

Wang, J., Jiu, J., Nogi, M., Sugahara, T., Nagao, S., Koga, H., He, P., and Suganuma, K. (2015). “A highly sensitive and flexible pressure sensor with electrodes and elastomeric interlayer containing silver nanowires.” *Nanoscale*, 7(7), 2926–2932.

Wang, S., Zi, Y., Zhou, Y. S., Li, S., Fan, F., Lin, L., and Wang, Z. L. (2016a). “Molecular surface functionalization to enhance the power output of triboelectric nanogenerators.” *J. Mater. Chem. A*, 4(10), 3728–3734.

Wang, Y., Yang, X., Yu, X., Duan, J., Yang, Q., Duan, Y., and Tang, Q. (2020). “Triboelectric charging behaviors and photoinduced enhancement of alkaline earth ions doped inorganic perovskite triboelectric nanogenerators.” *Nano Energy*, 77, 105280.

Wang, Z. L. (2020). “On the first principle theory of nanogenerators from Maxwell’s equations.” *Nano Energy*, 68, 104272.

- Wang, Z. L., Jiang, T., and Xu, L. (2017). "Toward the blue energy dream by triboelectric nanogenerator networks." *Nano Energy*, 39, 9–23.
- Wang, Z. L., Long, W., Chen, L. J., Niu, S., and Zi, Y. (2016b). *Triboelectric Nanogenerators*. Switzerland: Springer International Publishing.
- Wang, Z. L., and Wu, W. (2012). "Nanotechnology-enabled energy harvesting for self-powered micro-/nanosystems." *Angew. Chemie - Int. Ed.*, 51(47), 11700–11721.
- Wen, R., Guo, J., Yu, A., Zhang, K., Kou, J., Zhu, Y., Zhang, Y., Li, B. W., and Zhai, J. (2018). "Remarkably enhanced triboelectric nanogenerator based on flexible and transparent monolayer titania nanocomposite." *Nano Energy*, 50, 140–147.
- Wu, C., Chou, M.-H., and Zeng, W.-Y. (2018). "Piezoelectric Response of Aligned Electrospun Polyvinylidene Fluoride / Carbon Nanotube Nanofibrous Membranes." *Nanomaterials*, 8(6), 420.
- Wu, C. M., and Chou, M. H. (2016). "Sound absorption of electrospun polyvinylidene fluoride/graphene membranes." *Eur. Polym. J.*, 82, 35–45.
- Xin, Y., Guo, C., Qi, X., Tian, H., Li, X., Dai, Q., Wang, S., and Wang, C. (2016a). "Wearable and unconstrained systems based on PVDF sensors in physiological signals monitoring: A brief review." *Ferroelectrics*, 500(1), 291–300.
- Xin, Y., Tian, H., Guo, C., Li, X., Sun, H., Wang, P., Lin, J., Wang, S., and Wang, C. (2016b). "PVDF tactile sensors for detecting contact force and slip: A review." *Ferroelectrics*, 504(1), 31–45.
- Xing, C., Guan, J., Li, Y., and Li, J. (2014). "Effect of a room-temperature ionic liquid on the structure and properties of electrospun poly(vinylidene fluoride) nanofibers." *ACS Appl. Mater. Interfaces*, 6(6), 4447–4457.
- Xu, C., Wang, A. C., Zou, H., Zhang, B., Zhang, C., Zi, Y., Pan, L., Wang, P., Feng, P., Lin, Z., and Wang, Z. L. (2018a). "Raising the Working Temperature of a Triboelectric Nanogenerator by Quenching Down Electron Thermionic Emission in Contact-Electrification." *Adv. Mater.*, 30(38), 1803968.

Xu, C., Zi, Y., Wang, A. C., Zou, H., Dai, Y., He, X., Wang, P., Wang, Y. C., Feng, P., Li, D., and Wang, Z. L. (2018b). “On the Electron-Transfer Mechanism in the Contact-Electrification Effect.” *Adv. Mater.*, 30(15), 1706790.

Xu, F., Li, X., Shi, Y., Li, L., Wang, W., He, L., and Liu, R. (2018c). “Recent developments for flexible pressure sensors: A review.” *Micromachines*, 9(11), 580.

Xu, M., Wang, Y. C., Zhang, S. L., Ding, W., Cheng, J., He, X., Zhang, P., Wang, Z., Pan, X., and Wang, Z. L. (2017). “An aeroelastic flutter based triboelectric nanogenerator as a self-powered active wind speed sensor in harsh environment.” *Extrem. Mech. Lett.*, 15, 122–129.

Xue, W., Lv, C., Jing, Y., Chen, F., and Fu, Q. (2017). “Fabrication of electrospun PVDF nanofibers with higher content of polar  $\beta$  phase and smaller diameter by adding a small amount of dioctadecyl dimethyl ammonium chloride.” *Chinese J. Polym. Sci.*, 35(8), 992–1000.

Yadav, P., Raju, T. D., and Badhulika, S. (2020). “Self-Poled hBN-PVDF Nanofiber Mat-Based Low-Cost, Ultrahigh-Performance Piezoelectric Nanogenerator for Biomechanical Energy Harvesting.” *ACS Appl. Electron. Mater.*, 2(7), 1970–1980.

Yang, L., Ji, H., Qiu, J., Zhu, K., and Shao, B. (2014). “Effect of temperature on the crystalline phase and dielectric and ferroelectric properties of poly(vinylidene fluoride) film.” *J. Intell. Mater. Syst. Struct.*, 25(7), 858–864.

Yang, X., Wang, Y., and Qing, X. (2019). “A flexible capacitive sensor based on the electrospun PVDF nanofiber membrane with carbon nanotubes.” *Sensors Actuators A Phys.*, 299, 111579.

Ye, H. J., Yang, L., Shao, W. Z., Sun, S. B., and Zhen, L. (2013). “Effect of electroactive phase transformation on electron structure and dielectric properties of uniaxial stretching poly(vinylidene fluoride) films.” *RSC Adv.*, 3(45), 23730–23736.

Yu, B., Mao, M., Yu, H., Huang, T., Zuo, W., Wang, H., and Zhu, M. (2017). “Enhanced Piezoelectric Performance of Electrospun Polyvinylidene Fluoride Doped with Inorganic Salts.” *Macromol. Mater. Eng.*, 302(11), 1700214.

- Zaarour, B., Zhu, L., and Jin, X. (2020). "Direct generation of electrospun branched nanofibers for energy harvesting." *Polym. Adv. Technol.*, 31(11), 2659–2666.
- Zha, G., Hu, N., Jiang, M., Zeng, X., and Hou, H. (2019). "Synthesis and properties of BaWO<sub>4</sub> nanocrystals prepared using a reverse microemulsion method." *Appl. Phys. A Mater. Sci. Process.*, 125, 207.
- Zhang, C., Yuan, X., Wu, L., Han, Y., and Sheng, J. (2005). "Study on morphology of electrospun poly(vinyl alcohol) mats." *Eur. Polym. J.*, 41(3), 423–432.
- Zhang, J. H., Zhou, Z., Li, J., Shen, B., Zhu, T., Gao, X., Tao, R., Guo, X., Hu, X., Shi, Y., and Pan, L. (2022). "Coupling Enhanced Performance of Triboelectric-Piezoelectric Hybrid Nanogenerator Based on Nanoporous Film of Poly(vinylidene fluoride)/BaTiO<sub>3</sub> Composite Electrospun Fibers." *ACS Mater. Lett.*, 4(5), 847–852.
- Zhang, R., and Olin, H. (2020). "Material choices for triboelectric nanogenerators: A critical review." *EcoMat*, 2(4), 12062.
- Zhu, G., Zhao, L. Y., Zhu, L. T., Deng, X. Y., and Chen, W. L. (2017). "Effect of Experimental Parameters on Nanofiber Diameter from Electrospinning with Wire Electrodes." *Int. Conf. Mater. Sci. Nanomater.*, Barcelona, Spain: IOP Publishing Ltd, 0120430–12055.
- Zhu, J., Sun, H., Xu, Y., Liu, T., Hou, T., Liu, L., Li, Y., Lin, T., and Xin, Y. (2019). "Preparation of PVDF / TiO<sub>2</sub> nano fi bers with enhanced piezoelectric properties for geophone applications." *Smart Mater. Struct.*, 28, 085006.
- Zhu, Y., Wu, Y., Wang, G., Wang, Z., Tan, Q., Zhao, L., and Wu, D. (2020). "A flexible capacitive pressure sensor based on an electrospun polyimide nanofiber membrane." *Org. Electron.*, 84, 105759.
- Zi, Y., Lin, L., Wang, J., Wang, S., Chen, J., Fan, X., Yang, P. K., Yi, F., and Wang, Z. L. (2015). "Triboelectric-pyroelectric-piezoelectric hybrid cell for high-efficiency energy-harvesting and self-powered sensing." *Adv. Mater.*, 27(14), 2340–2347.
- Zong, X., Kim, K., Fang, D., Ran, S., Hsiao, B. S., and Chu, B. (2002). "Structure and

process relationship of electrospun bioabsorbable nanofiber membranes.” *Polymer*, 43(16), 4403–4412.

## BIO-DATA

---

### GOVIND SHREENIVAS EKBOTE

#### Permanent address:

Block F, Room no. 02, 256 Gala,  
Raviwar Peth, Solapur-413005  
Maharashtra, INDIA.



#### Contact Details:

Email: [govind.ekbote@gmail.com](mailto:govind.ekbote@gmail.com)

Mobile no.: +91-9765576339

#### Academic Qualifications:

- Master of Technology in Nanotechnology (2017) from the National Institute of Technology of Karnataka, Surathkal, Karnataka, India.
- Bachelor of Engineering in Mechanical Engineering (2012) from Punyashlok Ahilyadevi Holkar Solapur University, Solapur, Maharashtra, India.

#### Research publications:

Articles in International Journals: 05

Article submitted to Journal: 02

Articles in Conference Proceedings: 02

Book chapter: 01 (Invited)



## LIST OF PUBLICATIONS

---

### SCI/Scopus indexed International journal:

1. Ekbote, G. S., Khalifa, M., Mahendran, A., and Anandhan, S. (2021). "Cationic surfactant assisted enhancement of dielectric and piezoelectric properties of PVDF nanofibers for energy harvesting application" *Soft Matter*, 17(8), 2215–2222.
2. Ekbote, G. S., Khalifa, M., Venkatesa Perumal, B., and Anandhan, S. (2023). "Development of a flexible piezoelectric and triboelectric energy harvester with piezo capacitive sensing ability from barium tungstate nanorod-dispersed PVDF nanofabrics" *Flex. Print. Electron.*, 8(2), 025011.
3. Ekbote, G. S., Khalifa, M., Venkatesa Perumal, B., and Anandhan, S. (2023) "A new multifunctional energy harvester based on mica nanosheets-dispersed PVDF nanofabrics featuring piezo-capacitive, piezoelectric and triboelectric effects" *RSC Applied Polymers*, 2023, 1, 266 - 280 (**invited paper as part of the themed collection: Celebrating the scientific accomplishments of RSC Fellows**).
4. Ekbote, G.S., Sathies, T., Anandhan, S. "Piezoelectric Electrospun PVDF nanofibers: A review on the effect of electrospinning and filler-polymer interaction on  $\beta$ -phase and piezoelectric response" *Journal of Micro and Nano Engineering*.(In pipeline)

### Conference proceedings:

1. Govind S. Ekbote, Mohammed Khalifa, S. Anandhan "Enhanced Piezoelectric and Triboelectric Performance of Mica Nanosheet Infused Electrospun PVDF Nanofiber-Based Energy Harvesters," National Conference on New Developments in Polymeric Materials (DPM-2023), Thiruvananthapuram, Kerala, India, March 2023.
2. Govind S. Ekbote, S. Anandhan "Design and Development of Barium Tungstate Nanorods-Dispersed Electroactive Polymer Nanofabrics for

Piezoelectric and Triboelectric Energy Harvesting”, 14th International Conference on Advancements in Polymeric Materials (APM-2023), CIPET, Bangalore, India, March 2023 (**Keynote Paper**).